

Liquid-phase epoxidation reactions over molecular sieve supported first-row transition metal catalysts

Hu, Shuangquan

2010

Hu, S. Q. (2010). Liquid-phase epoxidation reactions over molecular sieve supported first-row transition metal catalysts. Doctoral thesis, Nanyang Technological University, Singapore.

<https://hdl.handle.net/10356/47462>

<https://doi.org/10.32657/10356/47462>

Nanyang Technological University

Downloaded on 13 Mar 2024 16:26:04 SGT

**LIQUID-PHASE EPOXIDATION REACTIONS OVER
MOLECULAR SIEVE SUPPORTED FIRST-ROW
TRANSITION METAL CATALYSTS**

SHUANGQUAN HU

School of Chemical and Biomedical Engineering

A thesis submitted to the Nanyang Technological University
in partial fulfillment of the requirement for the degree of
Doctor of Philosophy

2010

Abstract

Catalysis is extremely important to the energy production and utilization, the chemical synthesis, and also to minimize the impact on environment. Epoxidation is an essential process, as epoxides are necessary and widely demanded in organic synthesis and industry. The design of epoxidation catalyst plays a vital role and lays the primary base of catalytic epoxidation process development. In this work, various first-row transition metal supported on molecular sieve catalysts were employed in catalyzing the liquid-phase epoxidation reactions. The main objective was to elucidate the pore structure effect of support on the catalytic performance.

To study the pore curvature effect and gain a better understanding on the pore structure effect on catalytic reactions in liquid phase, vanadium supported mesoporous catalysts with constant vanadium composition and chemical environment on the pore wall surface but various pore structures were prepared using a controlled atomic layer deposition (ALD) method. The V-TUD-1 catalyst with a large pore diameter and a 3-D mesoporous structure showed the best epoxidation activity among all the catalysts using *tert-butyl* hydroperoxide (TBHP) as oxidant.

Most of the currently available mesoporous materials are still not applicable to industrial process because of their high cost in the synthesis and low stability. From an engineering perspective, vanadium-containing NaX zeolite catalyst was synthesized in this study using an ion-exchange method. The *trans*-stilbene and *cis*-cyclooctene epoxidation reactions were carried out to evaluate the catalytic properties. More than 95% conversion and the stilbene oxide selectivity of 85% can

be achieved for *trans*-stilbene epoxidation and 54 % conversion in the cyclooctene epoxidation with selectivity of 96 %.

Optimization of the epoxidation process using a statistical method was also tackled in this study. A well-established catalyst, Co^{2+} -NaX (cobalt ion-exchanged faujasite zeolites) was adopted in optimizing the liquid-phase epoxidation using the response surface methodology (RSM). An iterative RSM framework was proposed, where Gaussian process (GP) regression models were applied for the approximation of the response surface. As a result, GP models generally attained higher accuracy of approximating the response surface, and thus provided greater chance to identify the optimum. In addition, GP was capable of providing both prediction mean and variance, the latter being a measure of the modeling uncertainty.

Acknowledgements

I would like to sincerely thank my supervisor, Professor Yanhui Yang, for his constant guidance and encouragement during the course of my research and writing of this thesis. I cannot have completed the project without absorbing his enthusiasm for chemical engineering. I also greatly appreciate Professor Tao Chen for his kind instruction and advice on the study of response surface methodology.

Thanks to the members of Professor Yang's group: Dr Qinghu Tang and Dr. Dapeng Liu for their precious advice on my experiments. Mr. Zhen Guo and Ms. Yuanting Chen for their helpful discussions and encouragements and Mr. Xianyang Quek, Ms. Lusi Li, Ms. Beitian Chia, Ms. Sufen Xu, and Ms. Ying Bin Lau for their help in the experiments.

I also would like to thank the School of Chemical and Biomedical Engineering, Nanyang Technological University for the scholarship support.

Lastly, I want to thank my family, they have always encouraged me in the pursuits and have provided much love and support.

Table of Contents

Abstract.....	i
Acknowledgements	iii
Table of Contents	iv
List of Figures	viii
List of Tables	xiii
Chapter 1 Background and Philosophy	1
1.1 Driving Force for Heterogeneous Catalysis in Epoxidation	1
1.2 Mesoporous Materials as Support	2
1.3 Motivation of the Study on the Pore Structure Effect	3
Chapter 2 Literature Review	7
2.1 Epoxidation.....	7
2.1.1 Importance of Epoxidation and Industrial Applications.....	7
2.1.2 Epoxidation Catalysts.....	10
2.2 Mesoporous Materials	12
2.2.1 Introduction of Mesoporous Materials	12
2.2.2 Synthesis of Mesoporous Molecular Sieves and Formation Mechanism	16
2.2.3 Characterization of Mesoporous Molecular Sieves.....	20
2.3 Transition Metal Supported on Mesoporous Molecular Sieves	21
Chapter 3 Techniques of Characterization and Synthesis	31
3.1 Techniques.....	31
3.1.1 Nitrogen Physisorption.....	31

3.1.2 X-ray Diffraction (XRD)	32
3.1.3 Diffuse Reflectance UV-visible Spectroscopy.....	32
3.1.4 Raman Spectroscopy	33
3.1.5 Electron Paramagnetic Resonance (EPR).....	34
3.1.6 X-ray Absorption near Edge Structure (XANES).....	34
3.1.7 Hydrogen Temperature-Programmed Reduction (H ₂ -TPR)	35
3.1.8 Temperature-Programmed Desorption (TPD)	36
3.2 Synthesis.....	37
3.2.1 Materials	37
3.2.2 Synthesis of MCM-41 and V-MCM-41	37
3.2.3 Synthesis of SBA-15	38
3.2.4 Synthesis of TUD-1	39
3.2.5 Vanadium Grafting Method.....	39
3.2.6 Synthesis of Vanadium Incorporated NaX Zeolites.....	40
Chapter 4 Epoxidation of <i>trans</i> -Stilbene and <i>cis</i> -Cyclooctene over Vanadium	
Grafted Mesoporous Materials with Different Pore Sizes and Structures	43
4.1 Catalysts Characterization	44
4.2 Catalytic Performance on Epoxidation of <i>trans</i> -Stilbene and <i>cis</i> -Cyclooctene	52
4.2.1 <i>trans</i> -Stilbene Epoxidation.....	52
4.2.2 <i>cis</i> -Cyclooctene Epoxidation	56
4.3 Discussion on the Pore Pore Structure and Pore Size Effect	59
4.4 Conclusion	61
Chapter 5 Preparation, Characterization and Catalytic Properties of Vanadium	
Exchanged X Faujasite Zeolites for the Epoxidation Reaction of <i>trans</i> -Stilbene and	
<i>cis</i> -Cyclooctene	65
5.1 Catalysts Characterization	66

5.1.1 Degree of Exchange and Vanadium Content	66
5.1.2 XRD Patterns	67
5.1.3 Diffuse Reflectance UV-vis and UV-Raman Spectroscopy	69
5.1.4 XANES.....	71
5.2 Catalytic Performances in <i>trans</i> -Stilbene Epoxidation and <i>cis</i> -Cyclooctene Epoxidation.....	73
5.2.1 Catalytic Performances in <i>trans</i> -Stilbene Epoxidation.....	73
5.2.2 Catalytic Performances in <i>cis</i> -Cyclooctene Epoxidation.....	78
5.3 Conclusion	81
Chapter 6 Response Surface Methodology Using Gaussian Processes: Towards Optimizing the <i>trans</i> -Stilbene Epoxidation over Co ²⁺ -NaX Catalysts	
6.1 Experimental.....	90
6.2 Response Surface Methodology using Gaussian Processes.....	91
6.2.1. Experimental Design through Latin Hypercube Sampling.....	93
6.2.2. Gaussian Process Regression Modelling	97
6.2.3. Model-based Region-searching.....	100
6.2.4. Model-based Optimization	103
6.3 Results and Discussions.....	104
6.4 Conclusions.....	114
Chapter 7 Summary.....	118
Appendix.....	121
A.1 A non-Sodium Synthesis of Highly Ordered V-MCM-41 and its Catalytic Application in Isomerization	121
A.1.1 Experimental	123
A.1.2 Catalysts Characterization	124
A.1.3 Heptene isomerization	138

A.1.4 Conclusion 144

A.2 Publications 149

List of Figures

Figure 2.1 the epoxidation process for cyclohexene, cyclooctene and <i>trans</i> -stilbene	7
Figure 2.2 schematic explain of the propene oxide-styrene monomer process for the production of propene oxide.	9
Figure 2.3 Scheme for the allylic alcohols epoxidation by VO(acac) ₂	12
Figure 2.4. Pore models of mesostrucutres with symmetries of (A) <i>P6mm</i> , (B) <i>Ia$\bar{3}d$</i> , (C) <i>Pm$\bar{3}n$</i> , (D) <i>Pm$\bar{3}m$</i> , (E) <i>Fd$\bar{3}m$</i> , (F) <i>Fm$\bar{3}m$</i>	14
Figure 2.5 TEM images of MCM-41, SBA-15 and TUD-1.	15
Figure 2.6 Two synthetic strategies of mesoporous materials: (1) liquid-crystal templating process, (2) cooperative self-assembly.....	18
Figure 4.1 Nitrogen physisorption of various vanadium grafted mesoporous materials.	45
Figure 4.2 XRD patterns of various vanadium grafted mesoporous materials (a) low angle (b) high angle [$\ast = \text{V}_2\text{O}_5$].....	47
Figure 4.3 (a) Diffuse reflectance UV-VIS spectra and (b) Raman spectra of various vanadium grafted mesoporous materials.	49
Figure 4.4 Comparison of vanadium K-dege XANES regions for vanadium grafted mesoporous materials and the reference compounds.	50
Figure 4.5 Conversion and selectivity of <i>trans</i> -stilbene epoxidation over V-MCM- 41, V-SBA-15, and V-TUD-1 with different vanadium loadings. The reaction condition: 338K, 24h, 1 atm.....	53

Figure 4.6 Conversion and selectivity of <i>trans</i> -stilbene epoxidation over 3V-MCM-41, 3V-SBA-15, and 3V-TUD-1 with reaction time. The reaction condition: 338K, 1 atm and 3wt% vanadium.	54
Figure 4.7 Conversion and selectivity of <i>trans</i> -stilbene epoxidation over 3V-MCM-41, 3V-SBA-15, and 3V-TUD-1 as a function of temperature. The reaction condition: 24h, 1 atm, 3 wt.% vanadium.	55
Figure 4.8 Conversion and selectivity of <i>cis</i> -cyclooctene epoxidation over V-MCM-41, V-SBA-15, and V-TUD-1 with vanadium loadings. The reaction condition: 338K, 24h, 1atm.	56
Figure 4.9 Conversion and selectivity of <i>cis</i> -cyclooctene epoxidation over 3V-MCM-41, 3V-SBA-15, and 3V-TUD-1 with reaction time. The reaction condition: 338K, 1 atm, 3 wt. % vanadium.	57
Figure 4.10 Conversion and selectivity of <i>cis</i> -cyclooctene epoxidation over 3V-MCM-41, 3V-SBA-15, and 3V-TUD-1 as a function of temperature. The reaction condition: 338K, 24h, 1 atm.	58
Figure 4.11 Pore structure and pore size effect on the <i>trans</i> -stilbene and <i>cis</i> -cyclooctene epoxidation. All the results were obtained under the condition of 338K, 24h, 1 atm and 3 wt. % vanadium.	60
Figure 5.1 XRD patterns of the V-X and V-X(C) samples, the signal of NaX shown at the bottom was assigned to zeolite X.	68
Figure 5.2 (a) UV-Vis spectra of the V-X and V-X(C) samples; (b) UV-Raman spectra of V-X and V-X(C) samples.	69
Figure 5.3 The normalized XANES spectra at V K-edge for reference compounds, 6V-X, 6V-X(C) as well as the used samples 6V-X-A and 6V-X(C)-A.	71

Figure 5.4 (a) <i>trans</i> -stilbene conversion on V-X and V-X(C) samples with different vanadium loading; (b) selectivity of <i>trans</i> -stilbene oxide, benzaldehyde, and benzoic acid over V-X and V-X(C) samples with different vanadium loading. The reaction condition: 338K, 24h, 1 atm.	74
Figure 5.5 (a) <i>trans</i> -stilbene conversion change with different time over V-X and V-X(C) samples, (b) selectivity of <i>trans</i> -stilbene oxide, benzaldehyde, benzoic acid over V-X and V-X(C) samples with different time. The reaction condition: 338K, 1 atm, 3 wt.% vanadium.	76
Figure 5.6 (a) <i>trans</i> -stilbene conversion change with different temperature, (b) selectivity of <i>trans</i> -stilbene oxide, benzaldehyde, benzoic acid with different temperature. The reaction condition: 24h, 1 atm, 3 wt.% vanadium.	77
Figure 5.7 The influence of vanadium content on (a) <i>cis</i> -cyclooctene conversion and (b) cyclooctene oxide selectivity. The reaction condition: 338K, 24h, 1atm.	78
Figure 5.8 (a) <i>cis</i> -cyclooctene conversion with different temperature, (b) cyclooctene oxide selectivity with different vanadium content. The reaction condition: 24h, 1 atm, 3 wt.% vanadium.	79
Figure 5.9. Activation energy calculated by Arrhenius plot, the activation energies for epoxidation of <i>trans</i> -stilbene are 33.37 kJ/mol and 43.15 kJ/mol on 3V-X and 3V-X(C) respectively; the activation energies for epoxidation of <i>cis</i> -cyclooctene are 85.5 kJ/mol and 51.16 kJ/mol on 3V-X and 3V-X(C) respectively. The test reaction: 1 atm, 24h.....	80
Figure 6.1 Illustration of incremental LHS using one design factor within the range of [0 1]. (a) Initial two design points (denoted by “x”) generated by LHS. (b)	

Two additional design points (denoted by “o”) generated by one more run of LHS; they are close to the initial points and do not provide desired overall coverage of the range. (c) Two additional design points generated by incremental LHS.....	96
Figure 6.2 Prediction results (the first iteration) using leave-one-out cross-validation for GP (RMSE=5.42, $R^2=0.85$, NLPD=6.07) and quadratic regression (RMSE=7.66, $R^2=0.70$, NLPD=8.52) models.....	107
Figure 6.3 Prediction results (the second iteration) using leave-one-out cross-validation for GP (RMSE=3.77, $R^2=0.96$, NLPD=3.06) and quadratic regression (RMSE=5.31, $R^2=0.92$, NLPD=3.60) models.....	112
Figure 6.4 The response surface of conversion as a function of temperature and (a) oxygen pressure (b) stilbene conversion (c) stirring rate and (d) reaction time....	113
Figure A.1 X-ray diffraction patterns of Si-MCM-41 and V-MCM-41: (a) Si-MCM-41 synthesized with different amounts of ammonia; (b) V-MCM-41 with different vanadium content.	125
Figure A.2 Nitrogen physisorption of V-MCM-41 with different vanadium loading (a) isotherm graph of Si-MCM-41, 1V-MCM-41, 2V-MCM-41 and 3V-MCM-41 (b) Pore size distribution of Si-MCM-41, 1V-MCM-41, 2V-MCM-41 and 3V-MCM-41.....	126
Figure A.3 UV-vis spectrum of V-MCM-41, (a) absorbance graph of V-MCM-41 (b) UV absorption edge of V-MCM-41.	130
Figure A.4 Raman spectra V-MCM-41 materials.....	131
Figure A.5 EPR spectra (1 st derivative) of 0.2V-MCM-41, 1V-MCM-41, 2V-MCM-41, and 3V-MCM-41.	133

Figure A.6 H ₂ -TPR profiles of impregnated vanadium on different catalysts. (a),(b),(c),(d) represent impregnated V/MCM-41, 1V-MCM-41, 2V-MCM-41, 3V-MCM-41.....	134
Figure A.7 NH ₃ -TPD results of V-MCM-41 materials.....	136
Figure A.8 (a) XRD patterns of 1V-MCM-41 before and after reaction of heptene isomerization. (b) Isotherm graph of 1V-MCM-41 before and after heptene isomerization reaction (c) Pore size distribution of 1V-MCM-41 before and after heptene isomerization reaction. A represents the sample before reaction and B represents the sample after reaction.....	137
Figure A.9 Catalytic results about the conversion and selectivity of heptene isomers by Si-MCM-41, 1V-MCM-41, 2V-MCM-41 and 3V-MCM-41.	139
Figure A.10 Linear relationship between $\ln k$ vs $1/T$ for V-MCM-41.....	140
Figure A.11 Conversion and selectivity of isomers with different WHSV (0.5h ⁻¹ , 1h ⁻¹ , 2h ⁻¹) on 2V-MCM-41.	142
Figure A.12 Conversion and selectivity of isomers over long time test on 2V-MCM- 41 under 593K.....	143

List of Tables

Table 4.1 Physical properties of various vanadium grafted mesoporous materials.....	46
Table 4.2 Energy positions of various spectral features in the V K-edge XANES spectra	51
Table 5.1. Vanadium Content in samples	67
Table 5.2, Energy positions of various spectral features in the V K-edge XANES spectra	72
Table 6.1: The process factors. The response variable to be maximized is the stilbene conversion (%).	89
Table 6.2: Designed experiments and resultant stilbene conversion y (%): the first iteration.	104
Table 6.3 Designed experiments and resultants tilbene conversion y (%): the second iteration.	108
Table A.1 List of physicochemical properties of Si-MCM-41 and V-MCM-41	127
Table A.2 List of Edge Position of V-MCM-41 samples and the standard samples. ..	128

Chapter 1 Background and Philosophy

1.1 Driving Force for Heterogeneous Catalysis in Epoxidation

As a highly “strained and reactive cyclic” ether, epoxide has been named “the most valuable organic intermediates”, since the discovery of alkene epoxidation in 1909.¹ Epoxides have been playing a crucial role in synthetic chemistry,² chemical intermediates production,³ and the synthesis of a variety of products, e.g., perfume materials, epoxy resins, plasticizers, drugs, anthelmintic preparations.⁴ However, the conventional alkene epoxidation process, e.g., chlorhydrin process for propylene oxide, has the drawbacks in expensive source materials, long production period and toxic to environment. Thus recently built industry processes for epoxidation mostly have chosen hydroperoxide process technologies, which are setup based on the peroxidation of an alkane to alkyl-hydroperoxide and subsequently the alkyl-hydroperoxide with alkene. However, a disadvantage of this method is the production of a large amount of co-product. Therefore, searching for an environmentally friendly and efficient catalytic process to replace the use of stoichiometric oxidant, to minimize the formation of by-products, and to reduce the energy consumption will be enormously practical.

Metal-catalyzed alkene epoxidation has received gradually increasing attention, both in chemical synthesis and industrial processes, since the innovation of the “sharpless” epoxidation.^{5,6} Many metal complexes^{5,7-15} were studied in catalyzing the epoxidation among which mostly were homogenous catalysts. Recently, environmental and economic concerns have put up strong demand to re-design the commercially significant epoxidation processes, the use of toxic materials and the formation of harmful waste should be avoided.⁷ Heterogeneous catalysts which can be easily

recovered will meet these requirements. As such, applying heterogeneous catalysts in the metal-catalyzed epoxidation would be able to play a key role in the future development of environmentally benign process of alkene epoxidation.

1.2 Mesoporous Materials as Support

In 1980s, the discovery of TS-1 titanium silicate molecular sieves was recognized as a significant breakthrough to the alkene epoxidation.⁸ The catalytic technology, employing TS-1 as catalyst and H_2O_2 as oxidant, received progressive attention in the following years. However, the TS-1 molecular sieves are microporous materials, and they are not suitable for handling bulky reactant molecules as the restraint of the pore diameter, which limits the application of TS-1 in the fine chemical synthesis industry.

In 1991, Mobil researchers synthesized a large family of mesoporous silicates and aluminosilicate, currently known as the M41S mesoporous molecular sieves including hexagonal MCM-41, cubic MCM-48 and laminar MCM-50.⁹ Subsequently, the synthesis of various of mesoporous molecular sieves were reported, for example, HMS,¹⁰ SBA-15,¹¹ TUD-1,¹² and MSU.¹³ All these reported mesoporous materials possess high specific surface area and large pore volume. Furthermore, the pore size and pore structure can be easily controlled by changing the synthesis factors. Modification of these mesoporous molecular sieves was achieved by incorporating a wide spectrum of metal cations, such as Al,^{14,15} Ti,^{15,16} Zr,^{24,26} V,¹⁷ Co,¹⁸ Ni,¹⁹ or Fe²⁰ due to their amorphous silica wall structure, thus leading to materials with acidic, basic or redox catalytic properties. The epoxidation reaction was also widely investigated using the metal supported mesoporous molecular sieves due to their relatively larger pore size compared to zeolites. Vanadium, niobium and titanium modified mesoporous molecular

sieves were employed as catalysts for propylene epoxidation.²¹ Zr and Mn bimetallic mesoporous catalysts were investigated in the epoxidation of styrene.⁴

1.3 Motivation of the Study on the Pore Structure Effect

Extensive literatures now exist on the effect of uniform micropore structure on the activity and selectivity.²² How the uniform nanoscale pores affect the catalytic activity and selectivity remains as an ambiguous question. Recently, the radius of curvature of the pore wall effect on the catalytic reaction has been reported in the gas phase reaction over MCM-41.²³⁻²⁵ The change of pore size results in a curvature difference to the active sites located on the mesoporous supports. A small change in local geometry may have a remarkable effect on the atomic properties that would subsequently affect catalytic activity. However, no consistent conclusion on this issue was drawn for the liquid-phase catalytic reaction which is widely used in the large organic molecules transformations. With a carefully chosen model reaction, this curvature effect on liquid phase reaction can also be probed as the different catalytic performance. The elucidation of this curvature effect on liquid phase reaction will be able to provide helpful insight into the rational design of catalyst. In this thesis, liquid phase epoxidation reaction was employed as a probe reaction to investigate the radius of curvature effect. In order to overcome the doubts that other structural parameters may also have an effect on the catalytic activity and selectivity in the study of radius of curvature effect, the mesoporous molecular sieve catalysts were prepared in such a way that the metal content was regulated constant while varying the pore diameters and pore structures.

As numerous types of mesoporous materials were found in the past two decades, the catalytic performance using mesoporous support has already attracted much attention.²⁶⁻

³² Besides those reported striking catalytic results, employing mesoporous catalysts

enables us to reveal the effect of pore diffusion on the catalytic liquid phase reaction. The diffusion of reaction mixture in the confined nano-channels can be one of the limiting steps in a catalytic reaction in liquid phase; different pore structures would act differently in the reactant transport. MCM-41 and SBA-15 are two dimensional (2-D) hexagonal pore structures with difference in the pore size. The newly discovered mesoporous material TUD-1,³³ possesses three-dimensional (3-D) silicate network with disordered open pore structure. The difference in catalytic performance using MCM-41, SBA-15 and TUD-1 as catalyst support, can be the probe for the pore structure effect during the catalytic reactions. To avoid the difference in metal dispersion and chemical state, the atomic layer deposition is used to form similar metal composition and local environment on different support surfaces.

References:

- (1) Nikolaus, P. *Berichte der deutschen chemischen Gesellschaft* **1909**, 42, 4811.
- (2) Selvaraj, M.; Lee, T. G. *The Journal of Physical Chemistry B* **2006**, 110, 21793.
- (3) Calvete, T.; Gerbase, A. E.; Benvenutti, E. V.; Gregorio, J. R.; Robinson, D. *Journal of Sol-Gel Science and Technology* **2009**, 50, 69.
- (4) Selvaraj, M.; Song, S. W.; Kawi, S. *Microporous and Mesoporous Materials* **2008**, 110, 472.
- (5) Sharpless, K. B.; Verhoeven, T. R. *Aldrichimica Acta* **1979**, 12, 63.
- (6) Sharpless, K. B.; Michaelson, R. C. **1973**, 95, 6137.
- (7) Punniyamurthy, T.; Velusamy, S.; Iqbal, J. *Chemical Reviews* **2005**, 105, 2329.
- (8) Taramasso, M. US 4 410 501, 1983.
- (9) Beck, J. S.; Vartuli, J. C.; Roth, W. J.; Leonowicz, M. E.; Kresge, C. T.; Schmitt, K. D.; Chu, C. T. W.; Olson, D. H.; Sheppard, E. W.; McCullen, S. B.; Higgins, J. B.; Schlenker, J. L. *Journal of the American Chemical Society* **1992**, 114, 10834.

- (10) Tanev, P. T.; Chibwe, M.; Pinnavaia, T. J. *Nature* **1994**, 368, 321.
- (11) Zhao, D. Y.; Feng, J. L.; Huo, Q. S.; Melosh, N.; Fredrickson, G. H.; Chmelka, B. F.; Stucky, G. D. *Science* **1998**, 279, 548.
- (12) Shan, Z.; Jansen, J. C.; Zhou, W.; Maschmeyer, T. *Applied Catalysis A: General* **2003**, 254, 339.
- (13) Sayari, A. *Chemistry of Materials* **1996**, 8, 1840.
- (14) Cai, H. Q.; Zhao, D. Y. *Science in China Series B-Chemistry* **2009**, 52, 1090.
- (15) Szczodrowski, K.; Prelot, B.; Lantenois, S.; Douillard, J. M.; Zajac, J. *Microporous and Mesoporous Materials* **2009**, 124, 84.
- (16) Prasad, M. R.; Madhavi, G.; Rao, A. R.; Kulkarni, S. J.; Raghavan, K. V. *Journal of Porous Materials* **2006**, 13, 81.
- (17) Du, G.; Lim, S.; Pinault, M.; Wang, C.; Fang, F.; Pfefferle, L.; Haller, G. L. *Journal of Catalysis* **2008**, 253, 74.
- (18) Quek, X. Y.; Tang, Q. H.; Hu, S. Q.; Yang, Y. H. *Applied Catalysis a-General* **2009**, 361, 130.
- (19) Yang, Y. H.; Lim, S.; Du, G. A.; Wang, C. A.; Ciuparu, D.; Chen, Y.; Haller, G. L. *Journal of Physical Chemistry B* **2006**, 110, 5927.
- (20) Bachari, K.; Touileb, A.; Lamouchi, M. *Transition Metal Chemistry* **2009**, 34, 529.
- (21) Held, A.; Florczak, P. *Catalysis Today* **2009**, 142, 329.
- (22) Gates, B. C. *Catalytic Chemistry*; John Wiley and Sons: New York, 1992.
- (23) Lim, S. Y.; Haller, G. L. *Applied Catalysis a-General* **1999**, 188, 277.
- (24) Wei, D.; Chueh, W. T.; Haller, G. L. *Catalysis Today* **1999**, 51, 501.
- (25) Yang, Y. H., Du, G.A., Lim, S.Y. and Haller G.L. *Journal of Catalysis* **2005**, 234, 318.
- (26) Karakoulia, S. A.; Triantafyllidis, K. S.; Lemonidou, A. A. In *2nd International Workshop of the European-Network-of-Excellence: IN Situ Study and Development of Processes Involving NanoPORous Solids* Thessaloniki, GREECE, 2007, p 157.
- (27) Karakoulia, S. A.; Triantafyllidis, K. S.; Tsilomelekis, G.; Boghosian, S.; Lemonidou, A. A. *Catalysis Today*, 2007, 141, 245-253.

- (28) Tsoncheva, T.; Ivanova, L.; Dimitrova, R.; Rosenholm, J. *Journal of Colloid and Interface Science* **2008**, 321, 342.
- (29) Li, X. K.; Ji, W. H.; Zhao, J.; Zhang, Z.; Au, C. T. *Applied Catalysis a-General* **2006**, 306, 8.
- (30) Hu, Y. F.; Wang, S. X.; Guo, X. W.; Li, S. L.; Hu, S.; Sun, H. B.; Bai, L. *Catalysis Letters* **2005**, 100, 59.
- (31) Tang, Q.; Wang, C.; Hu, S.; Sun, H.; Chen, Y.; Haller, G.; Yang, Y. *Catalysis Letters* **2007**, 117, 25.
- (32) Chouyyok, W.; Panpranot, J.; Thanachayanant, C.; Prichanont, S. *Journal of Molecular Catalysis B: Enzymatic* **2009**, 56, 246.
- (33) Jansen, J. C.; Shan, Z.; Marchese, L.; Zhou, W.; von der Puil, N.; Maschmeyer, T. *Chemical Communications* **2001**, 713.

Chapter 2 Literature Review

2.1 Epoxidation

2.1.1 Importance of Epoxidation and Industrial Applications

Epoxides are among the most useful synthetic intermediates for the manufacturing of various chemical products, such as perfume, surface coating materials; epoxy resins adhesives, plasticizers and pharmaceutical products.¹⁻³ Small alkene epoxides are fundamental organic-industry materials. Notably, propylene oxide is the main source of polyether polyols which are used for the production of (polyurethane) foams. In addition, propylene oxide has also been applied for the production of propylene glycol and propylene glycol ethers.⁴ In the other category, large alkene epoxides, e.g., cyclohexene oxide, cyclooctene oxide and *trans*-stilbene (epoxidation process with catalysts and tert-butyl hydroperoxide (TBHP) is shown in Figure 2.1), are important intermediates in the fine chemical synthesis industry.

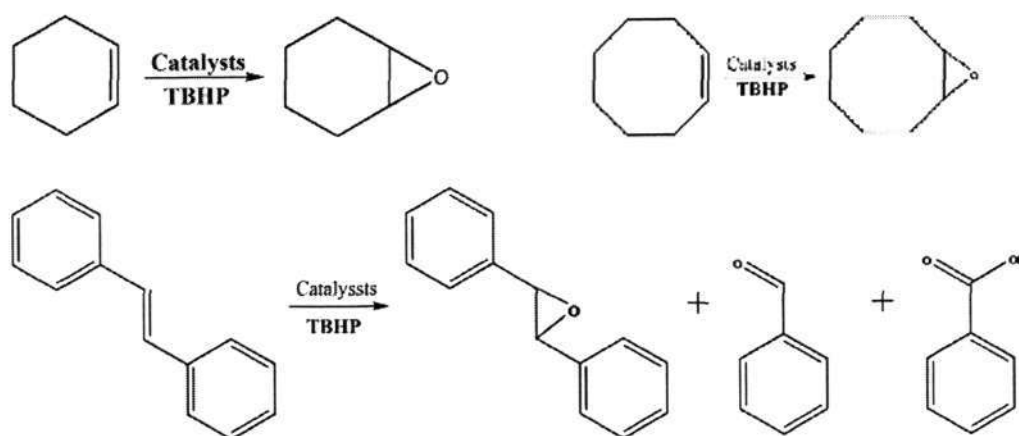


Figure 2.1 the epoxidation process for cyclohexene, cyclooctene and *trans*-stilbene

In the past decades, epoxidation processes have received great attention in the catalysis community. The mainstream epoxidation technologies are chlorohydrin process, hydroperoxide processes, silver catalysts and hydrogen peroxide combination, among others.⁵ In the chlorohydrin process, chlorohydrin is produced by reacting alkene with hypochlorous acid (HOCl). Then the chlorine reacts with acid to generate hypochlorous acid in aqueous phase.⁶ The chlorohydrin is afterward dehydrochlorinated to produce the epoxides using aqueous potassium hydroxide. The chlorohydrin process is processed to adapt the Wilkinson synthesis for ether.⁷ This route has been the chief process for the production of epoxides for years, especially ethylene oxide and propylene oxide. However, the chlorohydrin process causes serious environmental pollution and it has been gradually replaced by more environmentally friendly hydroperoxide processes, which is based on peroxidizing an alkane to an alkyl-hydroperoxide. The alkyl-hydroperoxides subsequently react with the alkene and produce epoxide and a corresponding alcohol. Two variants of the process are currently applied commercially. One is the epoxide styrene monomer process.^{8,9} In this process, ethylbenzene hydroperoxide formed by oxidation of ethylbenzene, reacts with alkene to produce epoxide and α -phenyl ethanol, and the α -phenyl could form styrene after dehydration. The other process is epoxide *tert*-butyl alcohol process.^{10,11} Isobutene is oxidized to TBHP in this process, and TBHP reacts with alkene to produce epoxides and *tert*-butyl alcohol. By dehydration, the *tert*-butyl alcohol is converted to isobutene, which can be further transformed to methyl-*tert*-butyl ether (MTBE) with methanol. Compared with chlorohydrins process, hydroperoxide process is clearly more desirable in terms of higher selectivity and less waste produced. However, the major disadvantage is the production of byproduct that is not associated with epoxides in the markets.

Figure 2.2 depicts a typical scheme of hydroperoxide process exemplified by the propylene oxide-styrene monomer process for the production of propylene oxide.⁵ In

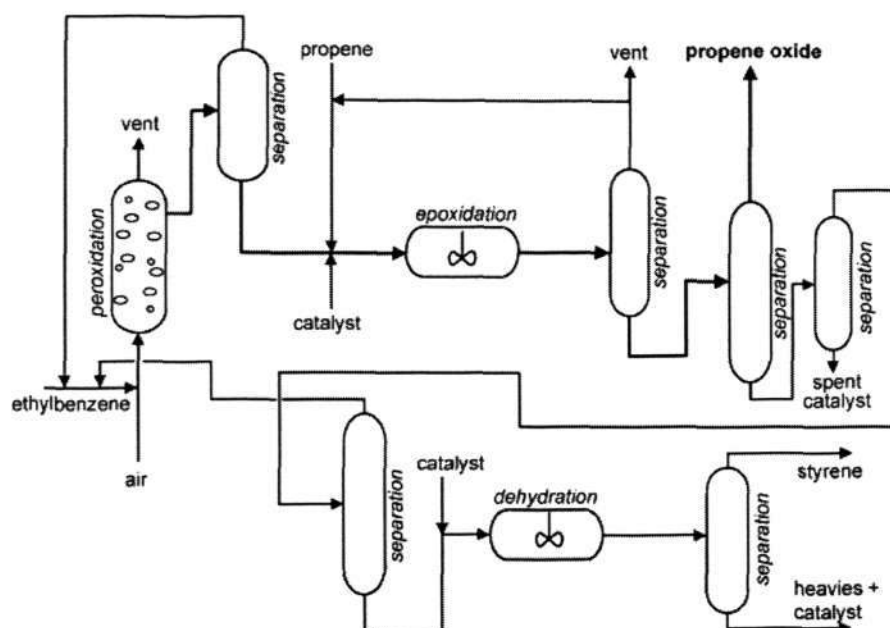


Figure 2.2 schematic explain of the propene oxide-styrene monomer process for the production of propene oxide.⁵

the first step, ethylbenzene or isobutene is converted to its corresponding hydroperoxide through direct liquid-phase oxidation with oxygen or air. In the second reactor, the hydroperoxide reacts with propylene to produce propylene oxide in the presence of catalyst. The silver catalyst is widely adopted in the production of ethylene oxide following a direct oxidation route.¹² Usually, a fixed-bed reactor is setup to epoxidize ethylene at 500 K and 30 bar. The silver catalyst has a high silver loading supported on a low-surface area metal oxide as opposed to microporous materials, which typically give poor yield due to the difficulty of heat transfer inside the particles and further oxidation of ethylene in the pores.¹² In principle, this method is equally applicable to produce epoxides other than ethylene oxide. However, no success has been reported to

prepare a silver catalyst in other epoxidation processes.⁵ Hydrogen peroxide combination process has been developed recently in the production of epoxides.¹³ Due to its high cost, hydrogen peroxide may not be an ideal oxidizing agent for commercial epoxidation; yet the process is promising if the hydrogen peroxide can be produced *in-situ*. Most hydrogen peroxide is currently produced by the anthrhydroquinone autoxidation process.¹⁴ Besides the afore reviewed methods, other processes are available for epoxidation using, e.g. nitrous oxide, molten salts and gold-titanium catalysts, though their effectiveness is not satisfactory so far. However, improvements are being made continuously and may lead to novel epoxidation processes in the future.

2.1.2 Epoxidation Catalysts

Catalysis by metal complexes and metals on support serves an important role in epoxidation. Many transition metal catalysts have been studied over the last few years, whereby titanium has attracted significant interest for catalyzing epoxidation.¹⁵⁻¹⁷ The titanium(IV) catalysts is applicable to the epoxidation of alkenes with varying molecular weights, including those of biological interest.^{15,18-20} Titanium(IV) catalysts are characterized as Lewis acid in their highest oxidation state. The titanium(IV) has low redox potential¹⁵ and is able to coordinate with ligand substitution.¹⁶ The titanium(IV) complexes can enhance the heterolysis of alkyl peroxides and of hydrogen peroxide by forming complexes similar to the inorganic peracid formed with hydrogen peroxide.¹⁷ The titanium (IV) alkoxides catalyzed epoxidation with alkyl hydroperoxide relatively slow and byproducts formed by adding *tert*-butyl peroxide radicals to the substrate are often observed.²⁰ These problems have been solved by developing the heterogeneous four-coordinate titanium centers in the microporous siliceous frameworks.^{21,22} The Ti-containing silicalite zeolites (TS-1) have a small pore size of 5.5Å and are relatively

more reactive toward terminal alkenes than toward *Z*-alkenes. Furthermore, modified TS-1 catalyst allows the epoxidation of *E*-isomers.²³ The Ti-MWW (a zeolite with large 10-membered ring, also termed MCM-22) mediates the epoxidation of linear aliphatic alkenes (carbon number range six to eight), and the process is selective towards *E*-alkenes (as opposed to *Z*-isomers) as the result of larger pore size.¹³ Several studies on epoxidation over zirconium (Zr) and hafnium (Hf) catalysts have been conducted. However, low yield of epoxides was observed when TBHP was employed as oxygen donor.²⁴

Vanadium is probably one of the most important transition metal catalysts used for epoxidation with TBHP.²⁵ The reactivity of vanadium (V) in catalyzing epoxidation is similar to that of titanium (IV). The stereochemistry of epoxidation catalyzed by the oxovanadium-ligand complexes is mostly dependent on the ligand present in the complex.^{26,27} The oxovanadium ions were also incorporated into polymer resins²⁸⁻³³ attached to acetylacetone, ethylenediamine, pyridine, dithiocarbonato, aminodiacetic acid, phosphonomethyl and hydroxymethyl ligands.^{28,31,32} The vanadyl ion can also be immobilized on sulfonated ion-exchange resins.³⁰ For alkene epoxidation with TBHP, immobilized oxovanadium catalysts typically outperform homogeneous oxovanadium complexes.²⁹ The epoxidation of allylic alcohols over $\text{VO}(\text{acac})_2$ with alkyl hydroperoxide provides a useful route to synthesize epoxy alcohols.^{18,34,35} The scheme about $\text{VO}(\text{acac})_2$ diastereoselectivity epoxidizes allylic alcohols to epoxy alcohols with TBHP and *m*-chloroperbenzoic acid is shown in Figure 2.3.^{36,37}

Other transition metals such as Mo, Co, Mn also attracted attention for epoxidation. Molybdenum (VI) complexes are good catalysts for epoxidation with alkyl hydroperoxide as oxidant,³⁸ however, molybdenum catalysts show low turnovers and

selectivity using H_2O_2 as oxidant.^{39,40} Cobalt complexes are effective catalysts for autoxidation and some of the work in alkene epoxidation is related to the autoxidation using molecular oxygen.^{15,41} $\text{Co}(\text{acac})_2$ and $\text{Co}(\text{acac})_3$ can catalyze the epoxidation with TBHP though low yields and long reaction time.⁴² The manganese (Mn) complexes are also efficient catalysts for alkene epoxidation mainly in the systems with biologically relevant manganese porphyrins.^{17,43,44} Other metal catalysts can refer to the review paper published elsewhere.¹⁷

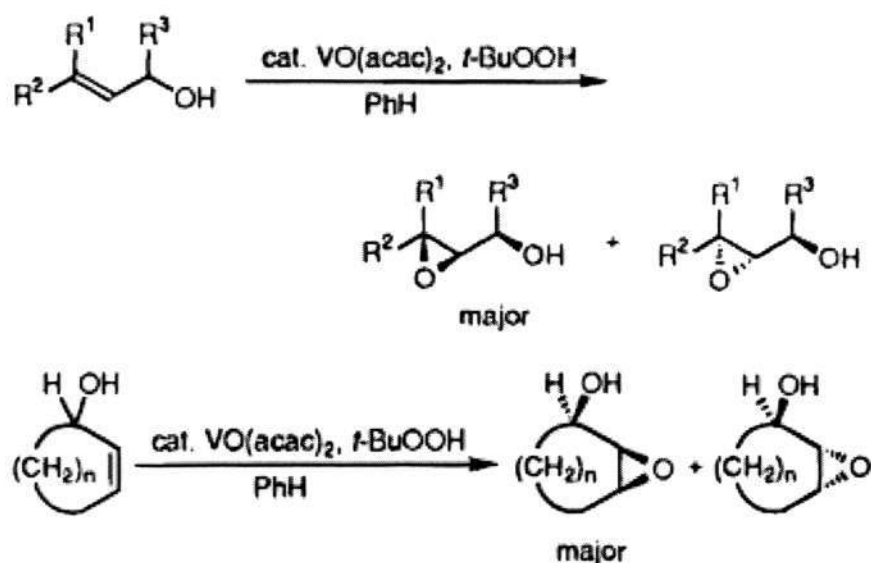


Figure 2.3 Scheme for the allylic alcohols epoxidation by $\text{VO}(\text{acac})_2$.³⁷

2.2 Mesoporous Materials

2.2.1 Introduction of Mesoporous Materials

Porous materials created by nature or by synthetic design have great impact in human activity.⁴⁵ Over the past decades, significant progress has been made to design, synthesize, characterize and evaluate various molecular sieves (most notably zeolites), and successful application on catalysis, adsorption and separation has been

demonstrated⁴⁶⁻⁴⁹ Bicontinuous phase has been employed to “orient the organic species which are then photopolymerized”.⁵⁰ The elimination of the unpolymerized components results in porous monoliths. This process established a new methodology for self-assembling microstructure. Based on this concept, it became possible to insert large organic molecules into layered clays to create novel porous materials with controllable pore size.⁵¹ Furthermore, the nanocomposite can be synthesized by using the cooperative organization of inorganic and organic molecular species.⁵² A new family of mesoporous molecular sieves, M41S, has also been discovered through formulating novel inorganic materials.⁵³ After that, a large variety of mesoporous materials with different mesostructures⁵⁴ (two-dimensional (2-D), space group $p6mm$, three-dimensional (3-D) hexagonal $P6_3/mmc$, 3D cubic $Pm\bar{3}m$, $Pm\bar{3}n$, $Fd\bar{3}m$, $Fm\bar{3}m$, $Im\bar{3}m$, bicontinuous cubic $Ia\bar{3}d$, etc.) and compositions (silica, metal oxides,⁵⁵⁻⁵⁹ metal sulfides,⁶⁰ metals, and even polymers and carbons^{61,62}) have been synthesized and some of them are shown in Figure 2.4. There are also some other mesostructures which cannot be defined by unit cell, symmetries, and space groups, such as HMS,⁶³ MSU,⁶⁴ KIT-1,⁶⁵ TUD-1,⁶⁶ and Al-MMS⁶⁷ mesoporous silicates. They show disordered mesopores and amorphous pore walls and are named foam-like or worm-like mesoporous molecular sieves. These disordered mesostructures can probably be described as randomly packed short interconnected 1-D pores.⁶⁸

At least five aspects are different in the structure and composition between mesoporous silicates and zeolites.⁵⁴ (1) Zeolites are crystalline silicates or aluminosilicates with 3D framework structures, and they are also inorganic crystals on the molecular scale. Mesoporous materials possess a periodic arrangement of a moiety and show well-defined diffraction spots on the mesoscale. (2) Zeolites are formed by aluminosilicate tetrahedron (TO_4) networks, while the pore walls of mesoporous

materials are amorphous. Hexa-coordination octahedron (TO_6) and penta-coordination trigonal bipyramid (TO_5) are allowed in mesoporous materials. (3) The TO_4 units of Si and Al in zeolites are normally four-connected by covalent bonds. But not all SiO_4 units in mesoporous silicates are four-connected. Three-connected and even two-connected SiO_4 units can be detected, and this leads to a hydrophilic surface with more hydroxyl groups (Si-OH). (4) Zeolites are hydrothermally stable, whereas some particular mesoporous silicates materials are unstable in water or steam. (5) Though significant effort has been attempted to synthesize mesostructured materials with zeolite-type walls,^{69,70} there has been little achievement with reproducibility.

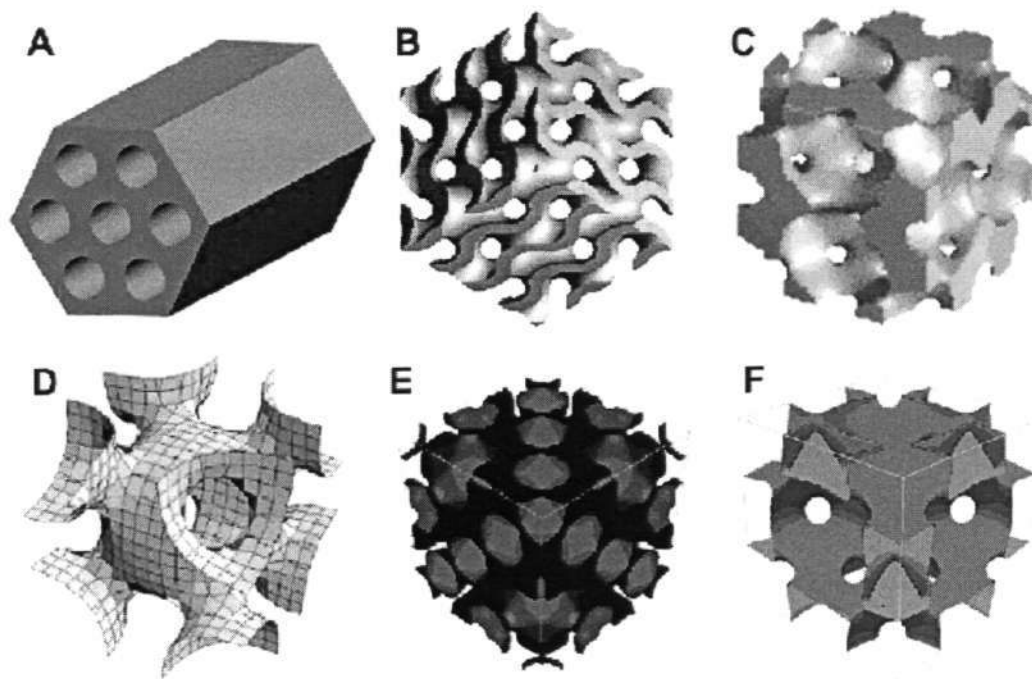


Figure 2.4. Pore models of mesostructures with symmetries of (A) $P6mm$, (B) $Ia\bar{3}d$, (C) $Pm\bar{3}n$, (D) $Pm\bar{3}m$, (E) $Fd\bar{3}m$, (F) $Fm\bar{3}m$.⁵⁴

MCM-41 materials are most widely studied ones among the many mesoporous materials reported to date, since they are flexible to produce by adjusting synthesis conditions, pore size and “framework” composition.⁷¹⁻⁸¹ They have two-dimensional

hexagonal ordered structures with uniform mesopores. The other well-studied mesoporous materials are the family of SBA, which can be synthesized by using a triblock copolymer as a structure-directing agent under acidic conditions.^{82,83} The salient feature of SBA is the hexagonal array of uniform tubular channels. Compared with MCM-41, SBA's pore diameter is much larger (in the range of 5-30nm), a property reducing diffusion resistance. Furthermore, SBA's thicker pore wall provides higher thermal stability and hydrothermal stability than MCM-41. TUD-1, with disordered 3-D sponge-like mesopore structure, is a recent addition member to the mesoporous material family.^{17,69,87} Dissimilar to amorphous silica, 3-D pores in the disordered mesostructures are interpenetrating, uniform, and adjustable. Furthermore, the uniform pores, high surface area, easy modification, and thermal stability offer good opportunities in catalysis, adsorption, separation, and immobilization. The TEM images of MCM-41, SBA-15 and TUD-1 are shown in Figure 2.5.

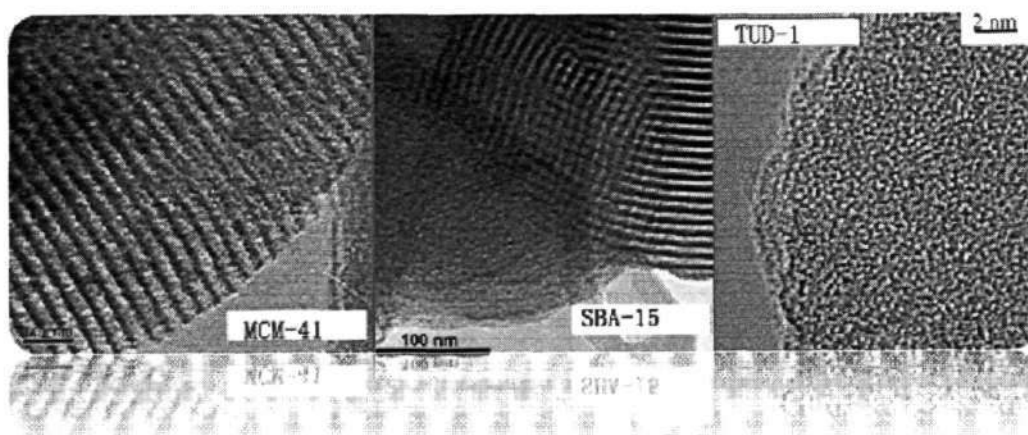


Figure 2.5 TEM images of MCM-41, SBA-15 and TUD-1.^{81,83,87}

2.2.2 Synthesis of Mesoporous Molecular Sieves and Formation Mechanism

2.2.2.1 Synthesis of Mesoporous Molecular Sieves

MCM-41 is one of the most popular mesoporous molecular sieves, and the synthesis is essentially similar to the synthesis of traditional zeolite and molecular sieve. The basic steps include mixing organic surfactants, silica, and/or alumina source to generate a supersaturated solution, and the mixture's temperature should be kept at a certain value for certain duration. In a typical MCM-41 synthesis, an aqueous solution containing silica source (e.g., fumed silica, sodium silicate, tetraethyl orthosilicate or tetramethylammonium silicate) is added to a clear alkaline aqueous solution of a micelle-forming surfactant under constant stirring.^{53,84,85} Surfactants, e.g., $C_nH_{2n+1}(CH_3)_3N^+$ ($n=8-12$) or $C_nH_{2n+1}C_5H_5N^+$ ($n=12$ or 16), which have a hydrophilic head group and a hydrophobic tail group, serve the purpose of agents for structure-directing. The silica source is hydrolyzed and condensed to form multidentate, multicharged anions that can coordinate with the surfactant head groups. The silica species and the surfactants assemble into a silica-surfactant phase, and formed a mixture of gel. The pH is adjusted (in the range of 8-11). After a period of time, the silica condenses to form a siloxane framework. The gel is transferred into a Teflon-lined autoclave or polypropylene bottle and heated under autogenous pressure in an air oven or in a steam box at a certain temperature for selected period of time. After crystallization, the solids are filtered and washed with deionized water, and then the template is removed.^{53,63,86-88}

The synthesis of mesoporous silicas SBA-15 is different from the synthesis of MCM-41. A well-established procedure of SBA-15 synthesis is described as follow.⁸² Triblock copolymer (poly(ethylene glycol)-block-poly(propylene glycol)-block-

poly(ethylene glycol)) is typically used as template. The first step is to dissolve the triblock copolymer in water under vigorous stirring. Upon dissolving, the HCl solution is added into the solution to obtain acid environment. Following that, tetraethyl orthosilicate is added into the mixture and stirred over a controlled time under controlled temperature, usually between 35 to 80°C. After crystallization and filtration, the SBA-15 is prepared.

Disordered mesoporous TUD-1 is synthesized following a surfactant-free procedure.⁶⁶ Tetraethylorthosilicate (TEOS) and triethanolamine (TEA) are mixed to form a homogeneous mixture. With aging and drying in air, the mixture solidified and formed a gel. Hydrothermal treatment is carried out to change the gel to a mesoporous structure. After remove the template via Soxhlet extraction or via calcination, TUD-1 mesoporous silica is obtained.

2.2.2.2 Formation Mechanism

Different from the traditional preparation of zeolites and molecular sieves template by a single organic molecule or metal ion, the formation of MCM-41 uses surfactants with an alkyl chain length having more than six carbon atoms. Therefore, a large number of studies have been carried out to investigate the formation and assembly of mesostructure on the basis of surfactant self-assembly.⁸⁹ Two main mechanisms, the cooperative self-assembly mechanism and liquid crystal templating (LCT) mechanism, seem to be plausible in the synthesis of ordered mesostructures, as shown in Figure 2.6.^{48,54,90-92}

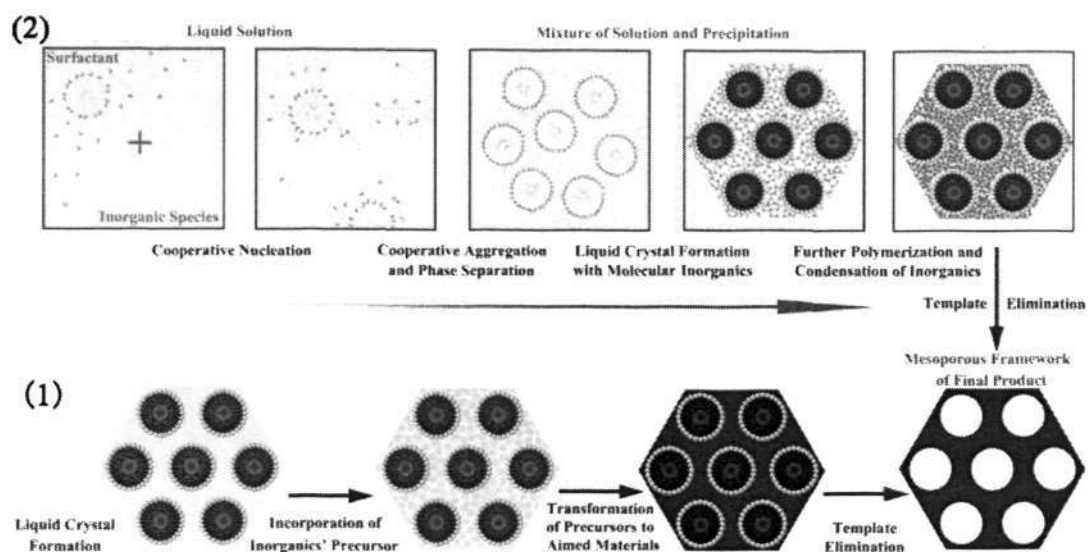


Figure 2.6 Two synthetic strategies of mesoporous materials: (1) liquid-crystal templating process, (2) cooperative self-assembly.⁵⁴

In the LCT mechanism, initially proposed by Beck et al.⁸⁴ the surfactants used for the preparation of mesostructures are amphibian molecules with a hydrophilic head groups face out to the surrounding water to minimize the total surface energy, leading to the formation of spherical micelles or micellar rods, as shown in Figure 2.6 (1). Importantly, within the LCT mechanism, the liquid crystalline mesophases (or micelles) serves the purpose of structure-directing templates, and thus the final product is a silicate skeleton that contains voids with the shape of these mesophases. There are two plausible pathways for the formation of mesostructure. First, the liquid crystals form in the surfactant solution and the added silicate condenses on the hydrophilic heads, leading to the formation of the wall of mesostructure. Second, the micellar rods resulted from the interaction and combination of surfactant molecules with siliceous species encapsulated by the inorganic phase, aggregate to form ordered structure. The influence of alkyl chain length and the increase of the pore diameter by adding mesitylene have been viewed as strong support to the LCT mechanism.⁹³

Kuroda, Inagaki and co-workers proposed a layer-to-hexagonal mechanism according to which the mesostructure is formed from a layered precursor.^{51,94} However, the mechanism is not general because the layered intermediate is unnecessary in the formation of hexagonal mesostructure in MCM-41. A “silicate rod assembly” mechanism was postulated by Davis and co-workers.⁹⁵ According to this mechanism, two or three monolayers of silicate species first deposit on the isolated surfactant micellar rods, the long surfactant-silicate rods then aggregate and pack into a long-range ordered hexagonal arrangement. Zhou and co-workers gave weak evidence for this mechanism for their observation on a single rod on the edge of samples at different synthetic stages using TEM.⁹⁶ However, this mechanism is still unconvincing due to the difficulty of assembling long rods. Stucky and co-workers proposed a cooperative formation mechanism (as shown in Figure 2.6 (2)) and this mechanism has been accepted by most researchers.^{55,97} The cooperative self-assembly process is established on the basis of the interactions between silicate and surfactants to form inorganic-organic mesostructured composites. Silicate polyanions such as silicate oligomers interact with positively charged groups in cationic surfactants. The silicate species at the interface polymerize, cross-link and change the charge density of the inorganic layers. In the reaction, the arrangements of surfactants and the charge density between inorganic and organic species influence each other. Hence the compositions of inorganic-organic hybrids differ to some degree. The matching of charge density at the interfaces of surfactant/inorganic species is crucial to determine the assembly process. The final mesophase is the ordered 3-D arrangement to reach lowest interface energy. This mechanism with different surfactant has been studied using NMR techniques.⁹⁸

The cooperative formation mechanism in a nonionic template system, such as preparation of SBA-15 with triblock copolymer P123 ($\text{EO}_{20}\text{PO}_{70}\text{EO}_{20}$) template, was

also investigated.^{99,100} A continuous transformation from spheroidal micelles into threadlike micelles was discovered and bundles were formed with dimensions. The elongation of micelles is a result of reduction of polarity and water content within the micelles due to the adsorption and polymerization of silicate species. Before the hydrothermal treatment, the majority of copolymer chains insert into silicate frameworks, which generate micropores after the removal of templates. Flodstrom et al studied the dynamics of SBA-15 formation.¹⁰¹ Four stages were observed during the cooperative assembly, which are the adsorption of silicates on globular micelles, the association of globular micelles into flocs, the precipitation of flocs, and the micelle-micelle coalescence. Khodakov et al.¹⁰² proposed a structure with a hydrophobic PO core and a PEO-water-silicate corona for the first stage. The cylindrical micelles then pack into large domains, and solvents are replaced by condensed silicate species at the same time.

TUD-1 is a new discovered disordered mesoporous molecular sieve and the formation mechanism is still not clear, as it is a surfactant-free synthesis route which cannot be identified into the above mechanisms. In current investigations,^{66,103} the templates (e.g. triethanolamine (TEA)) form meso-sized organic aggregates during heating. These organic aggregates are trapped in a silica framework, which was formed by condensing silica species. As a result, bulk phase separation of the silica species and the organic templates is avoided. The pore structure is primarily determined by cooperative organization of inorganic species and organic templates.

2.2.3 Characterization of Mesoporous Molecular Sieves

Reliable experimental techniques are important for characterizing the pore structures. Corma has generally reviewed the fundamental techniques used for

characterizing the mesoporous molecular sieves.⁴⁸ Mesoporous materials, in general, are characterized by a variety of techniques such as X-ray diffraction (XRD), gas physisorption, electron diffraction (ED), small-angle X-ray/neutron scattering (SAXS/SANS), transmission electron microscopy (TEM), scanning electron microscopy (SEM), gas adsorption measurements, nuclear magnetic resonance (NMR) and Fourier transform infrared (FT-IR) spectroscopies. Various techniques such as XRD, SAXS, and TEM combined with ED have been proven useful for the elucidation of structure, pore size and wall thickness. On the other hand, gas physisorption measurements have usually been used to determine surface area, pore size, and pore size distribution.¹⁰⁴ As an example, the combination of these methods has demonstrated that MCM-41 has a multilevel structure comprising mesopores, crystallites, and grains within the parent particles.¹⁰⁵ Typically, the crystallites have sizes of 30-50 nm and the particle diameters are around 0.3-0.8 μm . The fractal interpretation of adsorption data for various compounds has also shown the smooth mesopore surface on a molecular scale. This is indicated by the correlation of monolayer capacity with molecular area, yielding a slope of -1 on the logarithmic coordinates.¹⁰⁶ Several techniques are available for determining the pore sizes of mesoporous molecular sieves, including gas adsorption, small angle X-ray scattering, transmission electron microscope and porosimetry. Each method has a limited length-scale of applicability for probing the structure, but N_2 adsorption at its normal boiling point is the most popular because of its utility for both micropores and mesopores and because of its convenience and low cost.

2.3 Transition Metal Supported on Mesoporous Molecular Sieves

As mesoporous materials usually show uniform pores and high surface area, the mesoporous molecular sieves are good candidates as the support of catalysts.

Immobilization of catalytically active sites on molecular sieves has many potential advantages than other approaches such as the use of organic polymer supports. The chemical stability of the inorganic supports is important; particularly with regard to oxidizing conditions.¹⁰⁷ Their mechanical stability is often excellent, so that the issue of swelling depending on solvent conditions can largely be avoided.

Different methods introduce the catalytic active sites with different location and coordination. As the location and coordination of the metal sites are important to the activity of catalysts, the method introducing metal to mesoporous molecular sieves is an important step in the preparation of catalysts. Transition metals, as important epoxidation catalyst described in section 2.1.2, can be introduced into mesoporous molecular sieves with several methods. Take MCM-41 as a representative mesoporous molecular sieve, it can generally be concluded by five methods. (1) The direct hydrothermal synthesis method was used in the preparation of Al-MCM-41, Ti-MCM-41 and some other materials.^{108,109} In this method, the metal ions were added into the reactant system before the crystallization step. There are also other reports that B¹¹⁰, Zr¹¹¹, V^{112,113}, Cr¹¹⁴ and Nb¹¹⁵ were added into MCM-41 by this method. (2) Iwamoto and co-workers discovered that the template in the un-calcined MCM-41 exchanged with Mn²⁺ ions in water solution and as a result the Mn was introduced into the MCM-41 pores.^{116,117} (3) Grafting method is the method that organic metal or metal ions are grafted onto the surface of mesopore walls by the reaction with Si-OH in water free condition. This method was successfully applied on the preparation of Ti-MCM-41^{118,119} and V-MCM-41¹²⁰. (4) The chemical vapor deposition (CVD) method is also used in introducing metal ions into mesoporous molecular sieves. Iwamoto and co-workers prepared the Ti-MCM-41 using TiCl₄ as precursor,¹²¹ Caps and co-workers used the precursor of Mn₂(CO)₈ and CpMn(CO)₃ to get Mn-MCM-41¹²². (5) The

traditional impregnation method can also be used in the preparation of metal supported mesoporous catalysts.¹²³

The applications of transition metal supported mesoporous molecular sieves attracted many investigations. For example, vanadium, niobium and titanium modified mesoporous molecular sieves were used as catalysts for propylene epoxidation.¹²⁴ Vanadium oxide impregnated in MCM-41 was applied in the isomerization of heptene.¹²⁵ Zr and Mn bimetallic mesoporous catalysts were investigated in the epoxidation of styrene.² Transition metal complexes were also immobilized on the mesoporous molecular sieves to apply in the heterogeneous catalysis. Salen VO complex was immobilized in MCM-41 for oxidation of cyclohexane¹²⁶ and Mn(bpy)₂ⁿ⁺ (bpy=2,2'-bipyridine) complexes immobilized in mesoporous materials performed well in the olefin oxidation with H₂O₂.¹²⁷ The cationic [meso-Tetrakis(4-trimethylammoniophenyl)porphyrinato]oxovanadium(IV) (VOTAPP) tetrachloride was also encapsulated into MCM-41 and applied in the oxidation of alkenes.¹²⁸

References:

- (1) Selvaraj, M.; Lee, T. G. *The Journal of Physical Chemistry B* **2006**, *110*, 21793.
- (2) Selvaraj, M.; Song, S. W.; Kawi, S. *Microporous and Mesoporous Materials* **2008**, *110*, 472.
- (3) Calvete, T.; Gerbase, A. E.; Benvenutti, E. V.; Gregorio, J. R.; Robinson, D. *Journal of Sol-Gel Science and Technology* **2009**, *50*, 69.
- (4) Kalich, D.; Wiechern, U.; Linder, J. In *Ullman's Encyclopedia of industrial chemistry*; 5th ed.; Verlag Chemie: Weinheim, Germany, 1993; Vol. A22, p 239.
- (5) Nijhuis, T. A.; Makkee, M.; Moulijn, J. A.; Weckhuysen, B. M. *Industrial & Engineering Chemistry Research* **2006**, *45*, 3447.
- (6) Richey, W. F. *Chlorohydrins*; 4 ed.; Wiley: New York, 1994; Vol. 6.

- (7) Bartolome, E.; Koehler, W.; Stoeckelman, G.; May, A. US. Patent No. 3,886,187, 1975.
- (8) Pell, M.; Korchak, E. I. U.S. Patent 3,439,001, 1969.
- (9) Dubner, W. S.; Cochran, R. N. U.S. Patent No. 6,504,038, 1993.
- (10) Kollar, J. U.S. Patent No. 3,351,635, 1967.
- (11) Marquis, E. T.; Keating, K. P.; Knifton, J. F.; Smith, W. A.; Sanderson, J. R.; Lustri, J. U.S. Patent No. 4,891,437, 1990.
- (12) Dever, J. P.; George, K. F.; Hoffman, W. C.; Soo, H. *Ethylene Oxide*; Wiley: New York, 1995; Vol. 9.
- (13) Lane, B. S.; Burgess, K. *Chemical Reviews* **2003**, *103*, 2457.
- (14) Hess, W. T. *Hydrogen Peroxide*; 4 ed. New York, 1995; Vol. 13.
- (15) Sheldon, R. A.; Kochi, J. A. *Metal-Catalyzed Oxidations of Organic Compounds*; Academic Press: New York, 1981.
- (16) Bradley, D. C.; Mehrotra, R. C.; Gaur, D. P. *Metal alkoxides*; Academic Press: New York, 1978.
- (17) Joergensen, K. A. *Chemical Reviews* **1989**, *89*, 431.
- (18) Sharpless, K. B.; Verhoeven, T. R. *Aldrichimica Acta* **1979**, *12*, 63.
- (19) Sheldon, R. A. *Journal of molecular Catalysis* **1980**, *7*, 107.
- (20) Sheldon, R. A.; van-Doorn, J. A. *Journal of Catalysis* **1973**, *31*, 438.
- (21) Munakata, H.; Oumi, Y.; Miyamoto, A. *Journal of physical chemistry B* **2001**, *105*, 3493.
- (22) Tantanak, D.; Vincent, M. A.; Hillier, I. H. *Chemical Communications* **1998**, 1031.
- (23) Wu, P.; Tatsumi, T. *Chemical Communications* **2001**, 897.
- (24) Ikegami, S.; Katsuki, T.; Yamaguchi, M. *Chemistry Letters* **1987**, 83.
- (25) Hawkins, E. G. E. *Journal of the American Chemical Society* **1950**, 2169.
- (26) Mimoun, H.; Chaumette, P.; Mignard, M.; Saussine, L.; Fischer, J.; Weiss, R. *Nouv. J. Chim.* **1983**, *7*, 467.

- (27) Mimoun, H.; Mignard, M.; Brechot, P.; Saussine, L. *Journal of the American Chemical Society* **1986**, *108*, 3711.
- (28) Sheng, M. N.; Zajacek, J. G. *Journal of Organic Chemistry* **1970**, *35*, 1839.
- (29) Linden, G. L.; Faron, M. F. *Journal of Catalysis* **1977**, *48*, 284.
- (30) Linden, G. L.; Faron, M. F. *Inorganic Chemistry* **1977**, *16*, 3170.
- (31) Bhaduri, S.; Ghosh, A.; Khwaja, H. *J. Chem. Soc., Dalton Trans* **1981**, 447.
- (32) Yokoyama, T.; Nishizawa, M.; Kimure, T.; Suzuki, T. M. *Bulletin of the chemical society of Japan* **1985**, *58*, 3271.
- (33) Zhang, K.; Kumar, G. S.; Neckers, D. C. *J. Polym. Sci.* **1985**, *23*, 1213.
- (34) Gould, E. S.; Hiatt, R. R.; Irwin, K. C. *Journal of the American Chemical Society* **1968**, *90*, 4573.
- (35) Sharpless, K. B.; Michaelson, R. C. *Journal of the American Chemical Society* **1973**, *95*, 6136-6137.
- (36) Thomson, S. A. *Journal of Organic Chemistry* **1988**, *53*, 1055.
- (37) Hirao, T. *Chemical Reviews* **1997**, *97*, 2707.
- (38) Celestin Bakala, P.; Briot, E.; Salles, L.; Bregeault, J.-M. *Applied Catalysis A: General* **2006**, *300*, 91.
- (39) Gresley, N. M.; Griffith, W. P.; Laemmel, A. C.; Nogueira, H. I. S.; Parkin, B. C. *Journal of Molecular Catalysis A: Chemical* **1997**, *117*, 185.
- (40) Kamiyama, T.; Inoue, M.; Enomoto, S. *Chemistry Letters* **1989**, 1129.
- (41) Quek, X. Y.; Tang, Q. H.; Hu, S. Q.; Yang, Y. H. *Applied Catalysis a-General* **2009**, *361*, 130.
- (42) Indicator, N.; Brill, W. F. *Journal of Organic Chemistry* **1965**, *30*, 2074.
- (43) Ramanathan, A.; Archipov, T.; Maheswari, R.; Hanefeld, U.; Roduner, E.; Glaser, R. *Journal of Physical Chemistry C* **2008**, *112*, 7468.
- (44) Zhang, Q. H.; Wang, Y.; Itsuki, S.; Shishido, T.; Takehira, K. *Journal of Molecular Catalysis a-Chemical* **2002**, *188*, 189.
- (45) Broekhoff, J. C. P.; Linsen, B. G. *Physical and chemical aspects of adsorbents and catalysts*; Academic Press: London, 1970.

- (46) Armor. *Applied Catalysis* **1992**, *B1*.
- (47) Chen, N. Y.; Garwood, W. E.; Dwyer, F. G. *Shape selective catalysis in industrial application*; 2 ed.; CRC: New York, 1996.
- (48) Corma, A. *Chemical Reviews* **1997**, *97*, 2373.
- (49) Davis, M. E.; Lobo, R. F. *Chemistry of Materials* **1992**, *4*.
- (50) Davis, M. E. *Nature* **1993**, *364*, 391.
- (51) Yanagisawa, T.; Shimizu, T.; Kuroda, K.; Kato, C. *Bulletin of the chemical society of Japan* **1990**, *63*.
- (52) Mann, S. *Nature* **1993**, 365.
- (53) Kresge, C. T.; Leonowicz, M. E.; Roth, W. J.; Vartuli, J. C.; Beck, J. S. *Nature* **1992**, *359*, 710.
- (54) Wan, Y.; Zhao *Chemical Reviews* **2007**, *107*, 2821.
- (55) Huo, Q. S.; Margolese, D. I.; Ciesla, U.; Feng, P. Y.; Gier, T. E.; Sieger, P.; Leon, R.; Petroff, P. M.; Schuth, F.; Stucky, G. D. *Nature* **1994**, *368*, 317.
- (56) Sun, T.; Ying, J. Y. *Nature* **1997**, *389*, 704.
- (57) Tian, Z. R.; Tong, W.; Wang, J. Y.; Duan, N. G.; Krishnan, V. V.; Suib, S. L. *Science* **1997**, *276*, 926.
- (58) Yang, P. D.; Zhao, D. Y.; Margolese, D. I.; Chmelka, B. F.; Stucky, G. D. *Nature* **1998**, *396*, 152.
- (59) Zou, X. D.; Conradsson, T.; Klingstedt, M.; Dadachov, M. S.; O'Keeffe, M. *nature* **2005**, *437*, 716.
- (60) Trikalitis, P. N.; Rangan, K. K.; Bakas, T.; Kanatzidis, M. G. *Nature* **2001**, *410*, 671.
- (61) Attard, G. S.; Kanatzidis, M. G. *Nature* **2006**, *441*, 1122 .
- (62) Sun, D.; Riley, A. E.; Cadby, A. J.; Richman, E. K.; Tolbert, S. H. *Nature* **2006**, *441*, 1126.
- (63) Tanev, P. T.; Pinnavaia, T. J. *Science* **1995**, *267*, 865.
- (64) Bagshaw, S. A.; Prouzet, E.; Pinnavia, T. J. *Science* **1995**, *269*, 865.
- (65) Ryoo, R.; Kim, H. S.; Ko, C. H.; Shin, C. H. *Journal of Physical chemistry B* **1996**, *100*, 17718.

- (66) Jansen, J. C.; Shan, Z.; Marchese, L.; Zhou, W.; von der Puil, N.; Maschmeyer, T. *Chemical Communications* **2001**, 713.
- (67) Mokaya, R.; Jones, W.; Moreno, S.; Poncelet, G. *Catalysis Letters* **1997**, 49, 87.
- (68) Lee, J.; Kim, J.; Kyeon, T. *Chemical Communications* **2003**, 1138.
- (69) Zhang, Z. T.; Han, Y.; Zhu, L.; Wang, R. W.; Yu, Y.; Qiu, S. L.; Zhao, D. Y.; Xiao, F. S. *Angewandte Chemie International Edition in English* **2001**, 40, 1258.
- (70) Liu, Y.; Pinnavaia, T. J. *Chemistry of Materials* **2002**, 14, 3.
- (71) Selvam, P.; Bhatia, S. K.; Sonwane, C. G. *Industrial & Engineering Chemistry Research* **2001**, 40, 3237.
- (72) Casci, J. L. *Advanced Zeolite Science and Applications* **1994**, 85, 329.
- (73) Ciesla, U.; Schuth, F. *Microporous and Mesoporous Materials* **1999**, 27, 131.
- (74) Fenelonov, V. B.; Romannikov, V. N.; Derevyankin, A. L. *Microporous and Mesoporous Materials* **1999**, 27, 131.
- (75) Lin, H. P.; Mou, C. Y. *Accounts of Chemical Research* **2002**, 35, 927.
- (76) Menon, V. C.; Komarneni, S. *Journal of Porous Materials* **1998**, 5, 43.
- (77) Oye, G.; Sjoblom, J.; Stocker, M. *Advances in Colloid and Interface Science* **2001**, 89, 439.
- (78) Pang, J. B.; Qiu, K. Y.; Wei, Y. *Journal of Inorganic Materials* **2002**, 17, 665.
- (79) Raman, N. K.; Anderson, M. T.; Brinker, C. J. *Chemistry of Materials* **1996**, 8, 1682.
- (80) Taguchi, A.; Schuth, F. *Microporous and Mesoporous Materials* **2005**, 77, 1.
- (81) Sayari, A. *Chemistry of Materials* **1996**, 8, 1840.
- (82) Zhao, D. Y.; Feng, J. L.; Huo, Q. S.; Melosh, N.; Fredrickson, G. H.; Chmelka, B. F.; Stucky, G. D. *Science* **1998**, 279, 548.
- (83) Zhao, D.; Huo, Q.; Feng, J.; Chmelka, B. F.; Stucky, G. D. *Journal of the American Chemical Society* **1998**, 120, 6024.

- (84) Beck, J. S.; Vartuli, J. C.; Roth, W. J.; Leonowicz, M. E.; Kresge, C. T.; Schmitt, K. D.; Chu, C. T. W.; Olson, D. H.; Sheppard, E. W.; McCullen, S. B.; Higgins, J. B.; Schlenker, J. L. *Journal of the American Chemical Society* **1992**, *114*, 10834.
- (85) Namba, S.; Mochizuki, A.; Kito, M. *Mesoporous Molecular Sieves* **1998**, *117*, 257.
- (86) Schuth, F. *Berichte Der Bunsen-Gesellschaft-Physical Chemistry Chemical Physics* **1995**, *99*, 1306.
- (87) Kim, M. J.; Ryoo, R. *Chemistry of Materials* **1999**, *11*, 487.
- (88) Hitz, S.; Prins, R. *Journal of Catalysis* **1997**, *168*, 194.
- (89) Zhao, X. S.; Lu, G. Q.; Millar, G. J. *Industrial & Engineering Chemistry Research* **1996**, *35*, 2075.
- (90) Yiing, J. Y.; Mehnert, C. P.; Wong, M. S. *Angewandte Chemie International Edition in English* **1999**, *38*, 56.
- (91) Schuth, F.; Schmidt, W. *Advanced Materials* **2002**, *14*, 629.
- (92) Schuth, F. *Chemistry of Materials* **2001**, *13*, 3184.
- (93) Myers, D. *Surfactant Science and Technology*; VCH: New York, 1992.
- (94) Inagaki, S.; Fukushima, Y.; Kuroda, K. *Journal of the Chemical Society, Chemical Communications* **1993**.
- (95) Chen, C. Y.; Xiao, S. Q.; Davis, M. E. *Microporous Materials* **1995**, *4*, 1.
- (96) Yuan, Z. Y.; Zhou, W. Z. *Chemical Physics Letters* **2001**, *333*, 427.
- (97) Huo, Q. S.; Margolese, D. I.; Ciesla, U.; Demuth, D. G.; Feng, P. Y.; Gier, T. E.; Sieger, P.; Firouzi, A.; Chmelka, B. F.; Schuth, F.; Stucky, G. D. *Chemistry of Materials* **1994**, *6*, 1176.
- (98) Epping, J. D.; Chmelka, B. F. *Current Opinion in Colloid & Interface Science* **2006**, *11*, 81.
- (99) Ruthenstein, S.; Frydman, V.; Abayasinghe, S.; Landau, M.; Goldfarb, D. *Journal of Physical Chemistry B* **2003**, *107*, 1739.
- (100) Ruthenstein, S.; Schmidt, J.; Kesselman, E.; Talmon, Y.; Goldfarb, D. *Journal of the American Chemical Society* **2006**, *128*, 3366.
- (101) Flodstrom, K.; Wennerstrom, H.; Alfredsson, V. *Langmuir* **2004**, *20*.

- (102) Khodakov, A. Y.; Zholobenko, V. L.; Imperor-Clerc, M.; Durand, D. *Journal of Physical Chemistry B* **2005**, *109*, 22780.
- (103) Shan, Z.; Jansen, J. C.; Zhou, W.; Maschmeyer, T. *Applied Catalysis A: General* **2003**, *254*, 339.
- (104) Gregg, S. J.; Sing, K. S. W. *Adsorption Surface Area and Porosity*; Academic Press: New York, 1982.
- (105) Sonwane, C. G.; Bhatia, S. K. *Langmuir* **1999**, *15*, 2809.
- (106) Sonwane, C. G.; Bhatia, S. K.; Calos, N. J. *Langmuir* **1999**, *15*, 4603.
- (107) De Vos, D. E.; Dams, M.; Sels, B. F.; Jacobs, P. A. *Chemical Reviews* **2002**, *102*, 3615.
- (108) De Vos, D.E.; Sels, B. F.; Jacobs, P. A. *Adv. Catal.* **2001**, *46*, 1.
- (109) Tanev, P. T.; Chibwe, M.; Pinnavaia, T. J. *Nature* **1994**, *368*, 321.
- (110) Sayari, A.; Danumah, C.; Moudrakovshi, I. L. *Chemistry of Materials* **1995**, *7*, 813.
- (111) Jones, D. J.; Jimenez-Jimenez, J.; Jimenez-lopez, A.; Maireles-torres, P.; Oliverra-Pastor, P.; Rodriguez-Castellon, E.; Roziere, J. *Journal of the Chemical Society, Chemical Communications* **1997**, *1994*, 1059.
- (112) Reddy, K. M.; Moudrakovski, I.; Sayari, A. *Journal of the Chemical Society, Chemical Communications* **1994**, 1059.
- (113) Luan, Z.; Xiu, J.; He, H.; Klinoswki, J.; Kevan, L. *Journal of physical chemistry B* **1996**, *100*, 19595.
- (114) Ulagapan, N. R.; Rao, C. N. R. *Chemical Communications* **1996**, 1047.
- (115) Zhang, L.; Ying, J. Y. *AIChE J.* **1997**, *43*, 2793.
- (116) Yonemitsu, M.; Tanaka, Y.; Iwamoto, M. *Chemistry of Materials* **1997**, *9*, 2679.
- (117) Iwamoto, M.; Tanaka, Y. *Catal. Surveys Jpn* **2001**, *5*, 25.
- (118) Maschmeyer, T.; Rey, F.; Sankar, G.; Thomas, J. M. *Nature* **1995**, *378*, 2787.
- (119) Oldroyd, R. D.; Thomas, J. M.; Maschmeyer, T.; Macfaul, P. A.; Snelgrove, D. W.; Ingold, K. U.; Wayner, D. D. M. *Angewandte Chemie International Edition in English* **1996**, *35*, 2787.

- (120) Marchese, L.; Gianotti, E.; Dellarocca, V.; Maschmeyer, T.; Rey, F.; Coluccia, S.; Thomas, J. M. *Physical Chemistry Chemical Physics* **1999**, 585, 1.
- (121) Wu, P.; Iwamoto, M. *J. Chem. Soc., Faraday Trans* **1998**, 94, 2871.
- (122) Caps, V.; Tsang, S. C. *Catalysis Today* **2000**, 64, 19.
- (123) Berndt, H.; Martin, A.; Bruchner, A.; Schreier, E.; Muller, D.; Kosslick, H.; Wolf, G. U.; Lucke, B. *Journal of Catalysis* **2000**, 191, 384.
- (124) Held, A.; Florczak, P. *Catalysis Today* **2009**, 142, 329.
- (125) Hu, S.; Liu, D.; Li, L.; Borgna, A.; Yang, Y. *Catalysis Letters* **2009**, 129, 478-485.
- (126) Zhao, J. Q.; Wang, W. Y.; Zhang, Y. C. *Journal of Inorganic and Organometallic Polymers and Materials* **2008**, 18, 441.
- (127) Eswaramoorthy, M.; Rao, C. N. R. *Chemical Communications* **1998**, 615.
- (128) Kalilur Rahiman, A.; Shanmuga Bharathi, K.; Sreedaran, S.; Rajesh, K.; Narayanan, V. *Inorganica Chimica Acta* **2009**, 362, 1810.

Chapter 3 Techniques of Characterization and Synthesis

Catalyst characterization is very important in catalysis research because the catalytic properties of a catalyst are largely determined by its composition and local structure on the atomic scale. Most of the publications related with catalysis contain at least some results of catalyst(s) obtained by characterization techniques. This chapter briefly describes the concepts of the techniques that are frequently employed for catalyst characterization and the synthesis processes of the supports and catalysts in this thesis.

3.1 Techniques

3.1.1 Nitrogen Physisorption

The properties of the texture and pore structure of solid materials is crucial for the development of a catalyst. Physisorption is a primary method for characterizing porous materials and the mesoporous materials with uniform pores have been extensively characterized by physisorption.^{1,2} Typical sorption measurements of mesoporous materials follow the type IV isotherm (such as MCM-41, MCM-48 and SBA series), from which the pore structure information including pore volume, surface area, pore size, and pore size distribution are extracted. One highlight is that capillary condensation takes place in the mesopore range will give a sharp increase in adsorption volume.³ The surface area can be calculated by the Brunauer-Emmett-Teller (BET) method.⁴ Pore volume, and pore size can be obtained by the Barrett-Joyner-Halenda (BJH) method.⁵ In this thesis, nitrogen adsorption-desorption isotherms were measured at 77K with a static volumetric instrument Autosorb-6b (Quanta Chrome). Prior to measurement, the samples were outgassed at 473K to a residual pressure below 10^{-4}

Torr. A Baratron pressure transducer (0.001-10 Torr) was used for low-pressure measurements. The pore size and pore size distributions were calculated from the desorption isotherms using the BJH method.

3.1.2 X-ray Diffraction (XRD)

X-Rays with wavelengths in the angstrom range, are sufficiently energetic to penetrate solids and are well suitable to discover their internal structure. X-Ray diffraction is one of the most essential techniques for characterizing the structure of crystalline or other ordered materials.⁶⁻⁸ It has been widely used in the study of MCM-41 and SBA-15 materials to complement nitrogen physisorption isotherms because of its capability of assessing the two-dimensional hexagonal structure of samples.⁹⁻¹² In the mesoporous samples, the XRD peaks do not result from local order on the atomic range, but from the ordered channel walls. The two dimensional hexagonal structure of MCM-41 or SBA-15 can be characterized by XRD showing a sharp (100) plane diffraction peak and also higher Miller index planes (110), (200) and (210).^{9,11,12} In this thesis, X-ray diffraction measurements were conducted using a Bruker AXS D8 X-ray diffractometer (Cu K α , λ = 1.542 Å, 40 KV, 30 mA).

3.1.3 Diffuse Reflectance UV-visible Spectroscopy

Ultraviolet (UV) and visible (vis) light can cause electronic transitions. When a molecule absorbs UV-vis radiation, the absorbed energy excites the electrons into an empty, higher energy orbital. The absorbance of energy can be plotted against the wavelength to yield a UV-vis spectrum. UV-vis spectroscopy has many applications including detection of eluting components in high performance liquid chromatography (HPLC),¹³ determination of the oxidation state of a metal center,¹⁴ or determination of

the maximum absorbance of a compound prior to a photochemical reaction.¹⁵ The reflection mode of UV-vis spectroscopy has been proved to be the simplest but a powerful method for characterizing metal supported zeolites^{16,17} and mesoporous molecular sieves catalysts^{18,19}.

In this thesis, diffuse reflectance UV-vis was used to investigate the local environment of different transition metal cations incorporated into the silica framework of mesoporous materials. Diffuse reflectance UV-vis spectra were recorded on a Vavian Cary-5000 spectrophotometer equipped with a diffuse-reflectance accessory. The spectra were recorded in the 200-800 nm range at room temperature with BaSO₄ as reference.

3.1.4 Raman Spectroscopy

Supported metal oxide catalysts consist of a two-dimensional, active surface metal oxide phase that is fully dispersed and chemisorbed onto the surfaces of high surface area oxide supports (e.g. alumina, titania, silica, etc.). Vibrational spectroscopy such as Raman has often been used to probe the molecular structures of supported metal oxides; a large amount of information has been obtained for the supported metal oxide catalysts. UV Raman spectroscopy has been proved to be a powerful technique for the study of catalysts and their solids,^{20,21} especially for the identification of isolated transition metal atoms substituted in the framework of molecular sieves.²² In this research, mesoporous materials were studied by Raman spectroscopy in order to identify the structure of the metal incorporated into the silica framework. Raman spectra were collected on a Renishaw inVia Raman system with a 325 nm laser as the excitation source. A laser output of 30 mW was employed and the maximum incident power at the sample was approximately 6 mW.

3.1.5 Electron Paramagnetic Resonance (EPR).

Electron paramagnetic resonance (EPR) spectroscopy is one of the most powerful methods for characterizing paramagnetic catalytic materials, surface species and reaction intermediates, such as those with one or more unpaired electrons. Alone, or in conjunction with other techniques, it has been successfully used in studying various properties of such systems, relating to their bulk, surface structure and catalytic reactivity.²³ The extreme sensitivity of EPR is certainly the most noticeable advantage compared with those of other spectroscopes, and is often used to study low-abundance active sites at catalytic surfaces and interfaces. It is fortunate that many catalytic systems contain transition metal ions as active centers and they can also act as convenient probes to follow the changes about their inner coordination sphere during the catalyst preparation and catalytic reactions. Paramagnetic species such as active sites or reaction intermediates can be located on the surface or within the bulk of the catalyst when porous materials are involved. The EPR in this thesis was carried out with Bruker EMX spectrometer at X-band (~9 GHz). All samples were tested under ambient conditions.

3.1.6 X-ray Absorption near Edge Structure (XANES)

XANES covers the range between 10 eV pre-edge and up to about 50 eV above the main edge. XANES spectra are determined by electronic transitions allowed by the dipole selection rule.²⁴ These transitions provide a probe to characterize electronic structures of transition metals in local environments which include the symmetry and overlap of wave functions and the covalent mixing parameters in occupied and unoccupied orbitals.²⁵ Physical and chemical properties of transition metals along with catalytic activities are governed by these electronic transitions.²⁶ The white line

intensity defines the transition to an electronic level just above the Fermi level of metals when photoelectrons have very small kinetic energy and consequently a large scattering across section. In this thesis, X-ray absorption measurements at vanadium k-edge were performed at the X-ray Demonstration and Development beam line of the Singapore Synchrotron Light Source (SSLS) where a Si (111) channel-cut monochrometer is equipped.²⁷ The samples were ground, pressed into self-supporting wafers, placed in a stainless steel cell, and measured in transmission mode at room temperature. The electron energy in the storage ring was about 700 MeV with a current of about 200 mA. Incident and transmitted X-ray intensities were measured by two ionization chambers filled with pure nitrogen. Energy was calibrated using V foil (5465.0 eV). The spectra collected were analyzed using WinXAS 2.3, an XAS data analysis program.

3.1.7 Hydrogen Temperature-Programmed Reduction (H_2 -TPR)

Hydrogen temperature programmed reduction (H_2 -TPR) is a useful technique for the characterization of metal oxide catalysts.²⁸⁻³² During a H_2 -TPR experiment, the catalyst under investigation is located in a fixed-bed reactor and exposed to a reducing hydrogen mixture that continuously flow through the catalyst bed, while the temperature is increased linearly controlled by a temperature program. The difference of the gas mixture concentration between the inlet and outlet is measured as a function of time by a thermal conductivity detector. The resulting H_2 -TPR profile contains qualitative information on the oxidation state of the reducible species. This technique is quantitative and signal obtained is of a kinetic nature directly correlated with catalytic behavior.

The characterization of H_2 -TPR in this thesis was performed using the Quantachrome Instrument Autosorb-1 static volumetric instrument. The reducibility and

the stability of metal catalysts were investigated by a temperature programmed reduction technique using a thermal conductivity detector (TCD). Approximately 300 mg of each sample was used for all tests. Prior to each TPR run, the sample cell was purged by ultra zero grade air at room temperature. Following on, the temperature was increased to 773K at 5K/min and soaked for 1 hour at the same temperature. Upon heating, the sample was cooled to room temperature. This procedure produces a clean surface before performing the H₂-TPR run. The gas flow was switched to 10 vol. % hydrogen balanced by argon. After baseline stabilization, the sample cell was heated at 5K/min to 1073K and signal was collected by the TPR software.

3.1.8 Temperature-Programmed Desorption (TPD)

The temperature programmed desorption of basic molecule such as ammonia (NH₃-TPD) is one of the most commonly used methods for measuring the surface acidity of porous materials. The sample was activated at 773 K for 1 h under flowing helium and then cooled to 400 K before introducing anhydrous ammonia (5% in helium) for 30 min. Subsequently the physisorbed ammonia was removed by flushing with helium during 2 h at 400 K. The thermal desorption was conducted in flowing helium from 400 to 873 K using a heating rate of 8 K min⁻¹. Ammonia desorption was monitored continuously with a thermal conductivity detector. The outlet gas was passed through a 0.01 M H₂SO₄ solution to absorb the released NH₃. After adsorption, the solution was back-titrated to obtain total amount of desorbed ammonia.

3.2 Synthesis

3.2.1 Materials

Sources of silica were tetramethylammonium silicate (TMASi, 20 wt.%, Aldrich) and tetraethylorthosilicate (TEOS, 98%, Acros Organics). The vanadium source was $\text{VOSO}_4 \cdot 3\text{H}_2\text{O}$ (Sigma-Aldrich Chemical Co.) and vanadium (V) oxytriethoxide (95%, Aldrich). The cobalt source was cobalt (II) sulphate heptahydrate ($\text{CoSO}_4 \cdot 7\text{H}_2\text{O}$, >99%, Sigma) and cobalt (II) nitrate hexahydrate ($\text{Co}(\text{NO}_3)_2 \cdot 6\text{H}_2\text{O}$, 98%, Aldrich). The templates used were $\text{C}_n\text{H}_{2n+1}(\text{CH}_3)_3\text{NBr}$ with $n=12, 14, 16$ (Sigma-Aldrich Co.) and with $n=10$ (American Tokyo Kasei), triblock copolymer poly(ethylene glycol)-block-poly(propylene glycol)-block-poly(ethylene glycol) (Aldrich, $\text{EO}_{20}\text{-PO}_{70}\text{-EO}_{20}$, P123), triethanolamine (TEA, >98.5%, Fluka) and tetraethyl ammonium hydroxide (TEAOH, 35%, Aldrich). Amberjet-4400(OH) ion-exchange resin (Sigma Co.) was used for ion-exchange process. Hydrochloride (HCl, 37%, Sigma-Aldrich), sodium hydroxide (NaOH, >98%, Fluka), acetic acid (Fisher Scientific), and ammonia solution ($\text{NH}_3 \cdot \text{H}_2\text{O}$, 25%, VWR International) was used for pH adjustment of the synthesis solution. Anhydrous toluene (HPLC grade, Fisher Scientific) was used as a solvent. The anti-foaming agent was Antifoam A (Sigma Co.) which is a silane polymer alkyl terminated by methoxy groups. NaX faujasite zeolite (Acros) was used as the support of zeolite.

3.2.2 Synthesis of MCM-41 and V-MCM-41

In a typical synthesis of Si-MCM-41, 0.97g of hexadecyltrimethyl-ammonium bromide (CTABr, >99%, Sigma) was dissolved in a certain amount of ammonia solution ($\text{NH}_3 \cdot \text{H}_2\text{O}$, 25%, VWR International) and distilled water. The total volume of ammonia solution and distilled water was maintained at 35ml. The mixture was stirred

till a clear solution was obtained. 4.5g of tetraethyl orthosilicate (TEOS, 98%, Acros Organics) was added dropwise followed by adding a certain amount of 2% VOSO_4 ($\text{VOSO}_4 \cdot 3\text{H}_2\text{O}$, 99.99%, Aldrich) solution. After additional mixing for about 120 min, the synthesis gel was transferred into a PTFE lined autoclave placed in an oven at 120°C for 48 hours. After cooling to room temperature, the resulting solid was recovered by filtration, washed with deionized water and dried under ambient conditions. The pre-dried solid was heated at a constant rate from room temperature to 813.2K over 20 hours under He and held for 1 hour under the same condition, followed by calcination at 813.2K for 5 hours with air to remove the residual surfactant. As the preparation process may cause some loss of vanadium and silica in the by-products, the final V content was determined by ICP analysis. The molar ratio composition of the gel mixture was $1\text{TEOS} : 0.12\text{CTAB} : x\text{NH}_3 \cdot \text{H}_2\text{O} : y\text{V} : 84.4\text{H}_2\text{O}$ where x varies from 9.2 to 18.5 (pH value from 12.5 to 14) and y varies from 0.012-0.035. The corresponding ammonia volume is 15-25 ml and the vanadium content is 1-3 wt. %.

3.2.3 Synthesis of SBA-15

The siliceous SBA-15 was synthesized according to a well-established procedure using tetraethylorthosilicate and triblock copolymer poly(ethylene glycol)-block-poly(propylene glycol)-block-poly(ethylene glycol) as template agent under acidic conditions. Firstly, 2 g of the triblock copolymer was dissolved in 12.5 ml of distilled water under stirring at 300 rpm. Upon dissolving, 0.29M HCl was added into the colorless solution by a ratio of 1ml 37% HCl: 34ml H_2O . The mixture was then allowed to stir for one hour. Upon stirring, 4.5g of tetraethyl orthosilicate was added into the mixture and stirred at 40°C for 24 hours. The colorless solution immediately turned into a white, cloudy suspension upon the addition of TEOS. After 24 hours, the white

suspension was transferred into polypropylene bottles and heated at 100°C in an oven for 24 hours. After cooling to room temperature, the resulting solid was recovered by filtration and washing with distilled water for several times. The solid was dried overnight under ambient condition and finally calcined in a flow of air at 540°C for 6 hours at a heating rate of 1°C /min, to remove any residual organic template materials, yielding the mesoporous SBA-15 support.

3.2.4 Synthesis of TUD-1

TUD-1 were synthesized following the method reported by Hamdy et al.³³ In a typical preparation, 1.0 g of distilled water was added drop wise to 10 g of tetraethyl orthosilicate under vigorous stirring. Subsequently, 7.2 g of triethanolamine and 1.8 g of distilled water were added to the above-mentioned solution dropwise. After stirring for 30 min, 10.1 g of tetraethyl ammonium hydroxide was added. The mixture was aged at room temperature for 24 h, dried at 373K for 24 h, and hydrothermally treated in a teflon-lined stainless steel autoclave at 453K for 8 h. The resultant TUD-1 powder was calcined at 873K for 10 h in air to remove the template.

3.2.5 Vanadium Grafting Method

The vanadium grafted mesoporous catalysts were synthesized following a controlled grafting process through atomic layer deposition.³⁴ First, vanadium (V) oxytriethoxide solution was prepared as the vanadium precursor in anhydrous toluene (HPLC grade, Fisher Scientific). The as-calcined siliceous mesoporous material was suspended in anhydrous toluene by refluxing under an inert N₂ atmosphere for 5 hours to ensure the removal of any adsorbed water. Certain amount of the vanadium precursor solution was added drop wise into the flask and kept stirring under reflux and N₂ atmosphere for 12

hours. The resulting mixture was cooled, filtered, and washed with anhydrous toluene several times to remove any unreacted vanadium precursor and by-products from the grafting reaction. The solid was dried at room temperature overnight and calcined at 813K for 6 hours to yield the final vanadium grafted catalysts.

3.2.6 Synthesis of Vanadium Incorporated NaX Zeolites

Firstly, 2 g of NaX faujasite zeolite was weighed and put into a flask and 50ml water was added in to the flask which was around pH=11. After that, a measured amount of 8 wt. % vanadyl sulfate solution was dropped into the flask. Keep stirring overnight, the mixture was filtered and dried in 403K. Then, the vanadium ion exchanged NaX zeolite were synthesized and named as xV-X where x is the weight percentage of vanadium proposed in the catalysts. Calcination was proceeded to study the station of the vanadium. The xV-X samples were calcined at 813K for 6 hours with a heating rate of 1K/min in the flow of air and the corresponding calcined catalyst was named xV-X(C) as C was denoted as the calcination.

References:

- (1) Lukens, W. W.; Schmidt-Winkel, P.; Zhao, D. Y.; Feng, J. L.; Stucky, G. D. *Langmuir* **1999**, *15*, 5403.
- (2) Ravikovitch, P.; Odomhnaill, S. C.; Neimark, A. V.; Schuth, F.; Unger, K. K. *Langmuir* **1995**, *11*, 4765.
- (3) Selvam, P.; Bhatia, S. K.; Sonwane, C. G. *Industrial & Engineering Chemistry Research* **2001**, *40*, 3237.
- (4) Brunauer, S.; Emmett, P. H.; Teller, E. *Journal of the American Chemical Society* **1938**, *60*, 309.
- (5) Barrett, E. P. J., L. G.; Halenda, P. P. *Journal of American Chemical Society* **1951**, *73*, 373.

- (6) Davey, W. P. *A study of Crystal Structure and its Applications*; McGraw-Hill: New York, 1934.
- (7) Wells, A. F. *Structural Inorganic Chemistry*; Clarendon Press: Oxford, 1984.
- (8) Niemantsverdriest, J. W. *Spectroscopy in Catalysis: an Introduction*; Weinheim: New York, 1993.
- (9) Zhao, D. Y.; Feng, J. L.; Huo, Q. S.; Melosh, N.; Fredrickson, G. H.; Chmelka, B. F.; Stucky, G. D. *Science* **1998**, *279*, 548.
- (10) Ciesla, U.; Schuth, F. *Microporous and Mesoporous Materials* **1999**, *27*, 131.
- (11) Beck, J. S.; Vartuli, J. C.; Roth, W. J.; Leonowicz, M. E.; Kresge, C. T.; Schmitt, K. D.; Chu, C. T. W.; Olson, D. H.; Sheppard, E. W.; McCullen, S. B.; Higgins, J. B.; Schlenker, J. L. *Journal of the American Chemical Society* **1992**, *114*, 10834.
- (12) Kresge, C. T.; Leonowicz, M. E.; Roth, W. J.; Vartuli, J. C.; Beck, J. S. *Nature* **1992**, *359*, 710.
- (13) Bevers, H.; Wijntje, R.; de Haan, A. B. *Lc Gc Europe* **2005**, *18*, 103.
- (14) Lyczko, K.; Bilewicz, A.; Persson, I. *Inorganic Chemistry* **2004**, *43*, 7094.
- (15) Il'ichev, Y. V.; Schworer, M. A.; Wirz, J. *Journal of the American Chemical Society* **2004**, *126*, 4581.
- (16) Montanari, T.; Bevilacqua, M.; Resini, C.; Busca, G. *Journal of Physical Chemistry B* **2004**, *108*, 2120.
- (17) Warnken, M.; Lazar, K.; Wark, M. *Physical Chemistry Chemical Physics* **2001**, *3*, 1870.
- (18) Gianotti, E.; Dellarocca, V.; Marchese, L.; Martra, G.; Coluccia, S.; Maschmeyer, T. *Physical Chemistry Chemical Physics* **2002**, *4*, 6109.
- (19) Hagen, A.; Schueller, K.; Roessner, F. *Microporous and Mesoporous Materials* **2002**, *51*, 23.
- (20) Xiong, G.; Li, C.; Feng, Z. C.; Ying, P. L.; Xin, Q.; Liu, J. K. *Journal of Catalysis* **1999**, *186*, 234.
- (21) Stair, P. C.; Li, C. *Journal of Vacuum Science & Technology a-Vacuum Surfaces and Films* **1997**, *38*, 2220.

(22) Li, C.; Xiong, G.; Xin, Q.; Liu, J. K.; Ying, P. L.; Feng, Z. C.; Li, J.; Yang, W. B.; Wang, Y. Z.; Wang, G. R.; Liu, X. Y.; Lin, M.; Wang, X. Q.; Min, E. Z. *Angewandte Chemie International Edition in English* **1999**, 38, 2220.

(23) Ertl, G.; Knozinger, H.; Schuth, F.; Weitkamp, J. *Handbook of heterogeneous*; 2 ed.; WILEY-VCH Verlag GmbH & Co. KGaA: New York, 2008.

(24) Parratt, L. G. *Physical Review* **1939**, 56, 295.

(25) Durham, P. J. *Chemical Analysis (New York, NY, United States)* **1988**, 92, 53.

(26) Bart, J. C. J. *Advances in Catalysis* **1986**, 34, 203.

(27) Moser, H. O.; Casse, B. D. F.; Chew, E. P.; Cholewa, M.; Diao, C. Z.; Ding, S. X. D.; Kong, J. R.; Li, Z. W.; Hua, M.; Ng, M. L.; Saw, B. T.; bin Mahmood, S.; Vidyaraj, S. V.; Wilhelmi, O.; Wong, J.; Yang, P.; Yu, X. J.; Gao, X. Y.; Wee, A. T. S.; Sim, W. S.; Lu, D.; Faltermeier, R. B. In *4th International Conference on Synchrotron Radiation in Materials Science (SRMS-4)* Grenoble, FRANCE, 2004, p 83.

(28) Suvanto, S.; Pakkanen, T. A. *Journal of Molecular Catalysis a-Chemical* **2000**, 164, 273.

(29) Berndt, H.; Martin, A.; Bruckner, A.; Schreier, E.; Muller, D.; Kosslick, H.; Wolf, G. U.; Lucke, B. *Journal of Catalysis* **2000**, 191, 384.

(30) Ramirez, J.; Contreras, R.; Castillo, P.; Klimova, T.; Zarate, R.; Luna, R.; *Applied Catalysis a-General* **2000**, 197, 69.

Hamdy, M. S.; Ramanathan, A.; Maschmeyer, T.; Hanefeld, U.; Jansen, J. C. *Chemistry-a European Journal* **2006**, 12, 1782.

(31) Hartmann, M.; Racouchot, S.; Bischof, C. *Microporous and Mesoporous Materials* **1999**, 27, 309

Hamdy, M. S.; Ramanathan, A.; Maschmeyer, T.; Hanefeld, U.; Jansen, J. C. *Chemistry-a European Journal* **2006**, 12, 1782.

(32) Koh, C. A.; Nooney, R.; Tahir, S.; *Catalysis Letters* **1997**, 47, 199.

Hamdy, M. S.; Ramanathan, A.; Maschmeyer, T.; Hanefeld, U.; Jansen, J. C. *Chemistry-a European Journal* **2006**, 12, 1782.

(33) Hamdy, M. S.; Ramanathan, A.; Maschmeyer, T.; Hanefeld, U.; Jansen, J. C. *Chemistry-a European Journal* **2006**, 12, 1782.

(34) Du, G.; Lim, S.; Pinault, M.; Wang, C.; Fang, F.; Pfefferle, L.; Haller, G. L. *Journal of Catalysis* **2008**, 253, 74.

Chapter 4 Epoxidation of *trans*-Stilbene and *cis*-Cyclooctene over Vanadium Grafted Mesoporous Materials with Different Pore Sizes and Structures

The effect of pore structure and pore size of mesoporous materials on catalytic performances has attracted increasing attention.¹⁻⁷ Hu et al. reported that the selectivity to isomerization was highly sensitive to the channel structure of molecular sieves in the hydroisomerization reaction.⁵ Karakoulia et al. indicated that the catalyst support with different pore structures and pore sizes strongly affected the catalytic activity.^{1,2} MCM-41 is one of the most widely studied mesoporous materials reported up to now due to its multilevel flexibility in terms of synthesis conditions, pore size tuning, and “framework” composition.⁸⁻¹⁸ The discovery of SBA-15 type mesostructured materials synthesized using tri-block copolymers as structure-directing agent under acidic conditions has opened a new opportunity in the field of heterogeneous catalysis.^{19,20} Both MCM-41 and SBA-15 mesoporous silica have a 2-D hexagonal array of uniform tubular channels. SBA-15 possesses larger pore diameter compared to MCM-41, enforcing lower diffusion resistance on the reactant molecules. Moreover, the thicker pore wall of SBA-15 relative to MCM-41 provides high thermal stability and hydrothermal stability. TUD-1, with a disordered 3-D sponge-like mesoporous structure, is a recent addition member to the mesoporous material family.²¹⁻²³ Dissimilar to amorphous silica, 3-D pores in the disordered TUD-1 mesostructures are interpenetrating, uniform, and adjustable. The high surface area and high thermal stability of TUD-1 offer good opportunities in catalysis, adsorption, separation, and immobilization.

Epoxides as the industrially important chemicals,²⁴ are largely used for the production of perfume materials, epoxy resins, plasticizers, and drugs.²⁵ Vanadium is a

well studied catalyst in the catalytic epoxidation.^{6,26,27} As reported, the catalytic activity of vanadium catalysts largely depends on the nature of vanadium active sites.²⁸⁻³⁰ For catalytic epoxidation reactions, the activity of vanadium is mainly contributed by the isolated tetrahedral vanadium oxide species which consist of the V=O bond.³¹ Numerous studies have addressed the synthesis and characterization of supported vanadium oxide species, but the precise control of isolated dispersion of vanadium active site was not successfully achieved by the impregnation method.^{2,28,32} Although highly dispersed vanadium on mesoporous materials have been prepared via direct hydrothermal method,³³ our previous work showed that direct hydrothermal synthesis would lead to vanadium buried inside the pore wall and cannot form active center.³⁴ Recently, the controlled post synthesis grafting method through atomic layer deposition (ALD) has been successfully used to prepare vanadium-isolated site dispersion on SBA-15.³⁵

Herein, we employed this novel post synthesis grafting method to prepare V-SBA-15, V-MCM-41 and V-TUD-1 catalysts with well-defined pore structure and highly dispersed vanadium active sites. Epoxidation of two representative bulky olefin compounds, *trans*-stilbene and *cis*-cyclooctene, over these mesoporous vanadium catalysts was selected as model reactions in order to get insight of the pore structure and size effect on liquid phase catalytic reaction.

4.1 Catalysts Characterization

The nitrogen physisorption isotherms and the corresponding pore size distributions are shown in Figure 4.1. All the vanadium grafted samples (V-MCM-41, V-SBA-15, and V-TUD-1) exhibit type IV isotherms according to the IUPAC classification, corresponding to typical mesoporous materials. For V-MCM-41 samples, the capillary

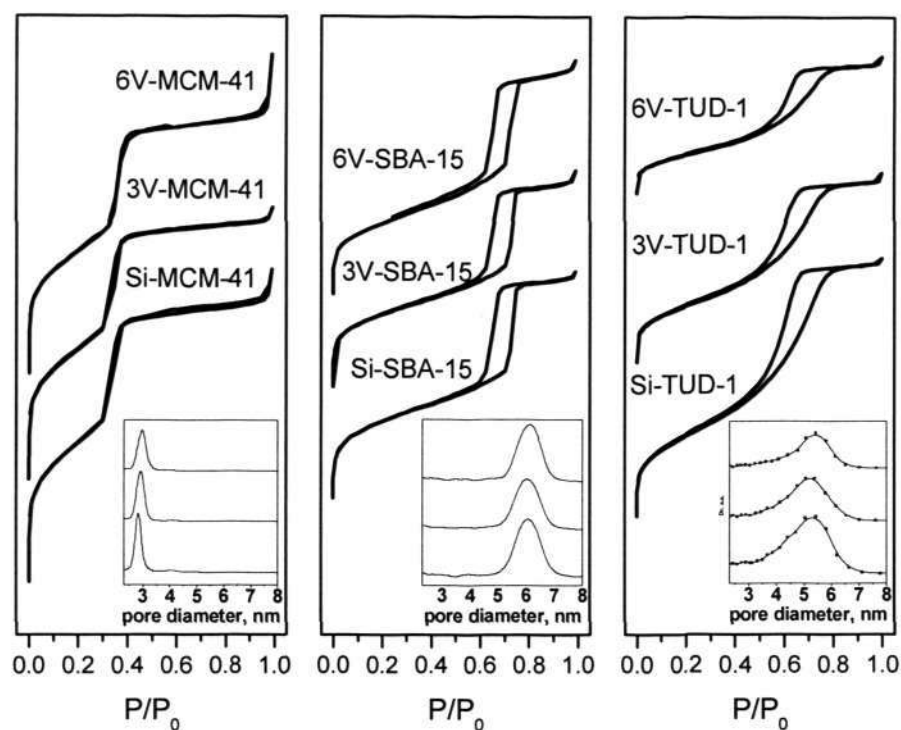


Figure 4.1 Nitrogen physisorption of various vanadium grafted mesoporous materials.

condensation shows a sharp step increase in nitrogen uptake at the relative pressure (P/P_0) range of 0.3-0.4 without adsorption-desorption hysteresis loop, suggesting highly ordered mesoporous structure with uniform channel sizes. The isotherm of V-SBA-15 displays a step increase of nitrogen uptake in the relative pressure (P/P_0) range of 0.6-0.8 with a characteristic H1-type broad hysteresis loop, corresponding to a large-pore mesoporous material with 1-D cylindrical channels.^{35,36} The hysteresis loop suggests long mesopores limit the emptying and filling of accessible volume.³⁷ V-TUD-1 samples also show a well-defined step at high partial pressure ($0.45 < P/P_0 < 0.8$) with a similar H1-type hysteresis loops.³⁸ V-TUD-1 possesses a relatively wider pore

size distribution compared to that of V-MCM-41 and V-SBA-15, which may be due to the disordered sponge-like mesostructure of V-TUD-1.^{22,23} The physical properties of all the vanadium-grafted samples are summarized in Table 4.1. V-MCM-41, V-SBA-15,

Table 4.1 Physical properties of various vanadium grafted mesoporous materials

Sample	Surface Area (m ² /g)	Pore Volume (cc/g)	Pore Diameter (nm)
Si-MCM-41	970	1.10	2.83
3V-MCM-41	925	1.09	2.82
6V-MCM-41	847	1.07	2.82
Si-SBA-15	1021	1.25	6.04
3V-SBA-15	834.8	1.20	6.04
6V-SBA-15	801.1	1.10	6.04
Si-TUD-1	1009	1.28	5.44
3V-TUD-1	706.6	1.15	5.40
6V-TUD-1	475.1	0.80	5.43

and V-TUD-1 show different pore diameters which are 2.9, 6.0, and 5.4nm, respectively. The decreased BET surface area and pore volume were observed on the vanadium-grafted samples compared to the corresponding parent mesoporous materials, however, the pore size did not change much. This should be due to the impregnated vanadium on the surface of the mesoporous pores which may destroy part of the surface structure. The surface areas of V-MCM-41 and V-SBA-15 samples remain greater than 800m²/g, while the surface area of V-TUD-1 decreases remarkably from 1009 to 475m²/g when

the vanadium loading is increased to 6wt. %. The pore volumes also decrease to certain extent when vanadium is grafted as showed in Table 4.1.

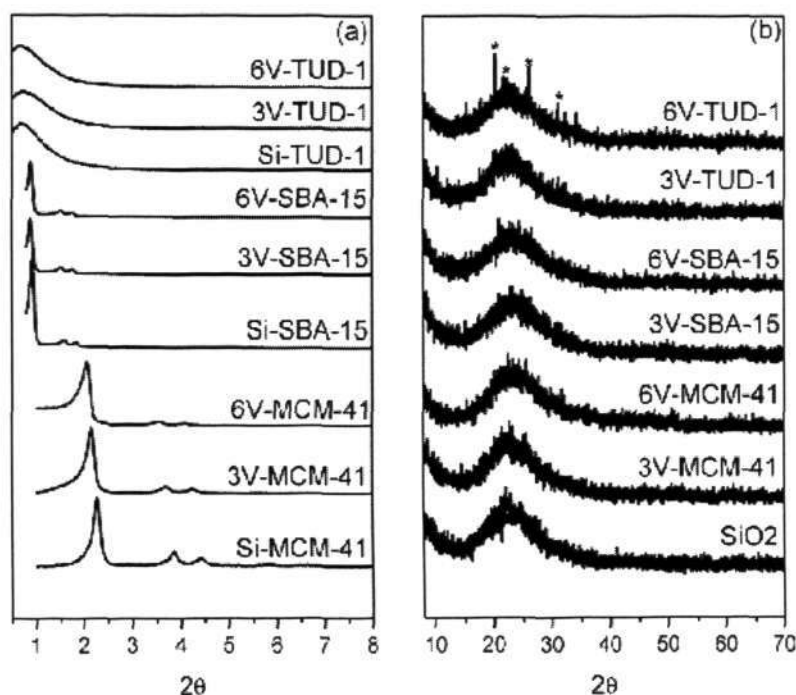


Figure 4.2 XRD patterns of various vanadium grafted mesoporous materials (a) low angle (b) high angle [$*$ = V_2O_5].

The XRD patterns of various vanadium-grafted samples are shown in Figure 4.2. The results during the low angle in Figure 4.2(a) suggest that the long-range order mesostructure is well retained after the grafting and calcination procedures. For V-MCM-41 and V-SBA-15 samples, the characteristic Bragg diffraction peaks indexed to (100), (110) and (200) planes can be discerned at around 2.15° , 3.70° , 4.32° and 0.93° , 1.58° , 1.82° for MCM-41 and SBA-15, respectively.^{36,39} The peaks slightly shift to lower angle after vanadium is grafted, which may be due to the increased pore wall

thickness and hence increased d value because the pore diameter remains substantially constant after grafting (see Table 4.1). In the high angle range shown in Figure 4.2(b), only one broad peak at around 23° for V-MCM-41 and V-SBA-15 samples is observable at high angle, which is ascribed to the amorphous nature of silicate. No crystalline phase of V species appears, indicating that vanadium species are highly dispersed on the pore wall surface. Only one relatively broad diffraction peak at around 0.7° can be discerned for V-TUD-1 samples, implying the irregular mesostructure of TUD-1.³⁸ The small shift of diffraction peak to lower angle may also be due to the increased pore wall thickness. No diffraction peaks at high angle are detected except the amorphous silicate in the samples of V-TUD-1 with vanadium loading of 3wt.% or less. Additional peaks ascribed to crystalline V_2O_5 appear in 6V-TUD-1 sample. Compared with V-MCM-41 and V-SBA-15, crystalline V_2O_5 is easier to form over V-TUD-1, although the reason remains unclear, thus causing the sharp decrease of specific surface area as shown in Table 4.1.

Diffuse reflectance UV-vis spectroscopy is a useful technique for gaining the insight about coordination environment and oxidation states of vanadium species in various molecular sieves/oxide surfaces.⁴⁰ The UV-vis spectra of V-MCM-41, V-SBA-15, and V-TUD-1 are shown in Figure 4.3(a). Siliceous mesoporous sample does not depict any noticeable absorbance. There is no absorbance peak in the range of 600-800nm for all the vanadium grafted samples due to the lack of the characteristic d-d transitions of $(VO)^{2+}$,⁴⁰ suggesting the complete oxidation of vanadium cations to V^{5+} oxidation state. All vanadium grafted samples show two bands at 253 and 393nm, which are attributed to the isolated vanadium species incorporated into the framework and on the framework surface, respectively.^{41,42} For the V-MCM-41 and V-SBA-15 samples, the absence of 320 and 450nm bands indicates there is no polymeric V-O-V bond and V_2O_5 crystallites

in these samples.⁴² An additional weak band at 488nm can be discerned in V-TUD-1 samples, implying a small amount of V_2O_5 crystallites.^{42,43}

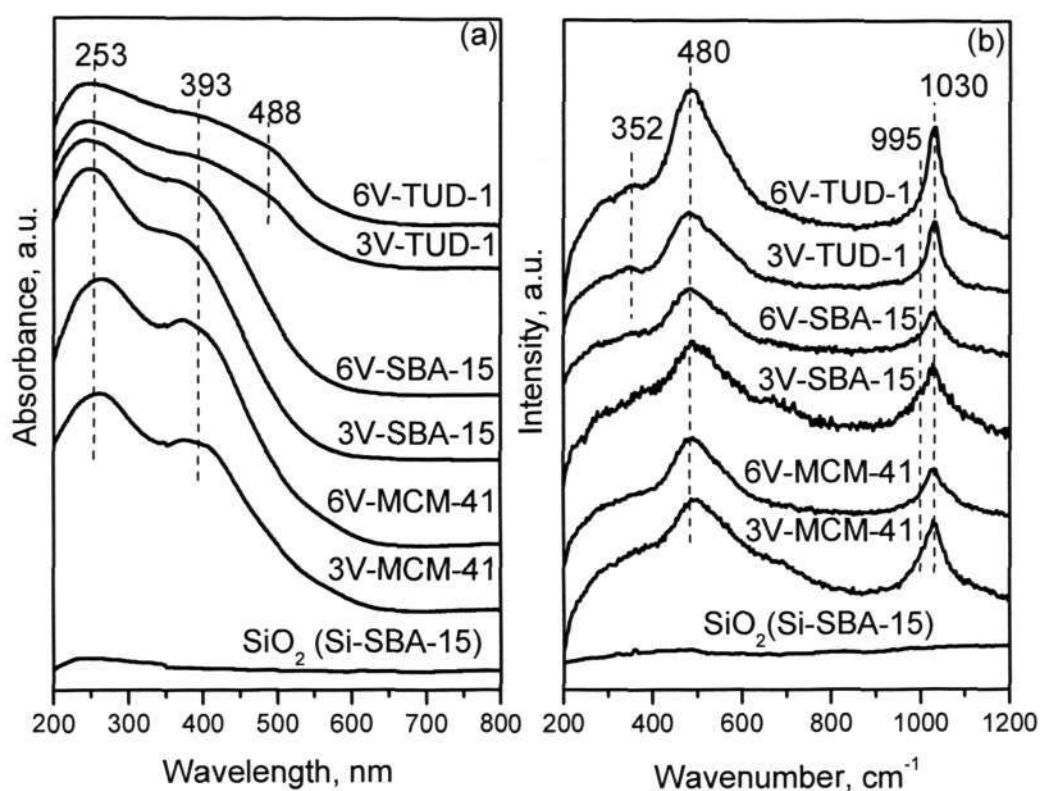


Figure 4.3 (a) Diffuse reflectance UV-VIS spectra and (b) Raman spectra of various vanadium grafted mesoporous materials.

Raman measurement is used to elucidate the molecular nature of vanadium domains. The Raman spectra of vanadium grafted samples are shown in Figure 4.3(b). A strong band at 1030cm^{-1} has been assigned to the symmetric $V=O$ stretching vibration of isolated VO_4 species,^{35,44-46} evidencing that most of vanadium species in the grafted samples are isolated VO_4 species. The peak at 480cm^{-1} is due to the three- and four-fold siloxane rings on the mesoporous silica support.⁴⁵ We also note a weak peak at 355cm^{-1}

for V-TUD-1 samples, which is due to a small amount of crystalline V_2O_5 . These results are accordance with the UV-vis characterization. The absence of V_2O_5 band at 995cm^{-1} in all the samples may suggestt here is no large crystalline V_2O_5 domain presented in all these mesoporous samples.

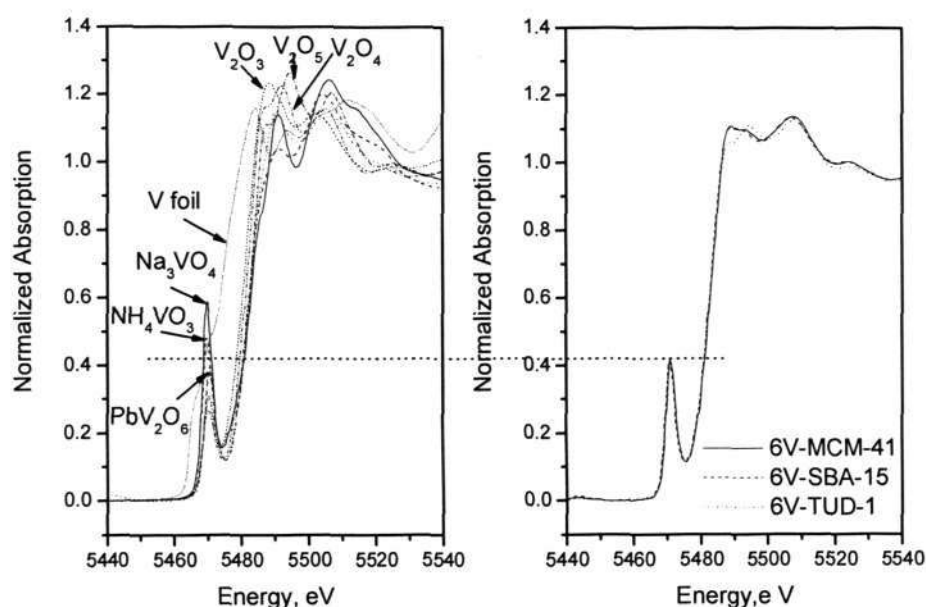


Figure 4.4 Comparison of vanadium K-edge XANES regions for vanadium grafted mesoporous materials and the reference compounds.

The normalized XANES spectra at vanadium k-edge for the vanadium grafted samples (6V-MCM-41, 6V-SBA-15, and 6V-TUD-1) as well as the reference compounds are illustrated in Figure 4.4. All spectra exhibit a strong pre-edge absorption feature corresponding to the forbidden transition of $1s \rightarrow 3d$, which is mainly caused by mixing the $4p$ orbital of vanadium and $2p$ orbital of oxygen with the $3d \pi$ orbital of vanadium atoms.^{35,47} The pre-edge peak height decreases monotonically as the vanadium coordination structure changes from tetrahedral (Na_3VO_4) to the square pyramidal (V_2O_5) or octahedral coordination (PbV_2O_6). The pre-edge peak height of

vanadium grafted samples rest between the reference compound NH_4VO_3 (distorted tetrahedral) and PbV_2O_6 (octahedral), suggesting a distorted tetrahedral local coordination. These vanadium centers are easily hydrated under ambient condition and part of vanadium stays in octahedral coordination.³⁵ The XANES results for vanadium-

Table 4.2 Energy positions of various spectral features in the V K-edge XANES spectra

Sample	Pre-edge peak position ^a (eV)	Main-edge position ^{a,b} (eV)	$E_{\text{pre-edge-}}$ E_0 (eV)	$E_{\text{edge-}}$ $E_{\text{pre-edge}}$ (eV)	Pre-edge peak height (a.u.)	Pre-edge peak intensity ^c (a.u.)
Na_3VO_4	5469.9	5482.4	4.9	12.5	0.59	2.13
NH_4VO_3	5469.9	5481.7	4.9	11.8	0.48	1.86
PbV_2O_6	5470.4	5482.0	5.4	11.6	0.39	1.56
V_2O_5	5470.4	5480.6	5.4	10.2	0.38	1.54
V_2O_4	5470.4	5478.8	5.4	8.4	0.27	--
V_2O_3	5470.4	5476.2	5.4	5.8	0.31	--
6V-MCM-41	5470.8	5482.1	5.8	11.3	0.42	1.59
6V-SBA-15	5470.8	5482.1	5.8	11.3	0.41	1.66
6V-TUD-1	5470.8	5481.7	5.8	10.9	0.42	1.64

^a The uncertainty in peak position is estimated to be ± 0.2 eV.

^b Main edge position is chosen as the mid point of absorption jump.

^c Peak intensity is calculated by peak height \times width at half maximum.

grafted samples and reference compounds are summarized in Table 4.2. The energy difference between pre-edge peak and the main edge is a measurement of the oxidation

state of vanadium.⁴⁷ The $E_{\text{edge}}-E_{\text{pre-edge}}$ value is 10.2 eV as in V_2O_5 , this value decreases to 8.4 eV for V_2O_4 . The $E_{\text{edge}}-E_{\text{pre-edge}}$ of the grafted samples varies from 10.9 to 11.3 eV, suggesting the vanadium in all the samples are V^{5+} oxidation state. The pre-edge peak intensities of vanadium grafted samples are between the value of NH_4VO_3 and PbV_2O_6 , implying that the vanadium domains of vanadium-grafted samples are of molecular cage size between distorted tetrahedral and octahedral coordination.⁴⁷

4.2 Catalytic Performance on Epoxidation of *trans*-Stilbene and *cis*-Cyclooctene

The epoxidation of *trans*-stilbene and *cis*-cyclooctene was performed by *tert*-butyl hydroperoxide in the presence of vanadium grafted mesoporous catalysts. Firstly, 0.2 g of the catalyst was added to 1 mmol of *trans*-stilbene or *cis*-cyclooctene in a round-bottom flask. 10 ml of MeCN and DMF mixture with 9:1 ratio (v/v) was added as the solvent of the reaction followed by adding 10 mmol of TBHP. The reaction was started by immersing the flask into a water bath with desired temperature. The compositions were analyzed by a gas chromatograph (GC, HP-6890N, Agilent) equipped with a HP-5 capillary column (30m*0.32mm*0.25 μm) and a FID detector.

4.2.1 *trans*-Stilbene Epoxidation

Figure 4.5 shows the vanadium loading effect on the epoxidation of *trans*-stilbene over V-MCM-41, V-SBA-15, and V-TUD-1. The conversion of *trans*-stilbene increases with the vanadium content before it reaches the maximum value of 100%. When the vanadium loading is less than 8 wt.%, the *trans*-stilbene conversion decreases in the sequence of V-TUD-1 > V-SBA-15 > V-MCM-41. The V-TUD-1 catalysts show the highest conversion though its lowest surface area. The selectivity of *trans*-stilbene oxide lies between 70 to 90%. It is noted that the selectivity shows an increase with the vanadium loading less than 6 wt.%, and slightly decreases after passing the maximum of

90%. The vanadium loading apparently affects the selectivity of epoxide, which can be attributed the decreased dispersion of active centers at high vanadium content, implying the catalytic reaction is remarkably more sensitive than characterization to probe the physicochemical properties of catalysts.

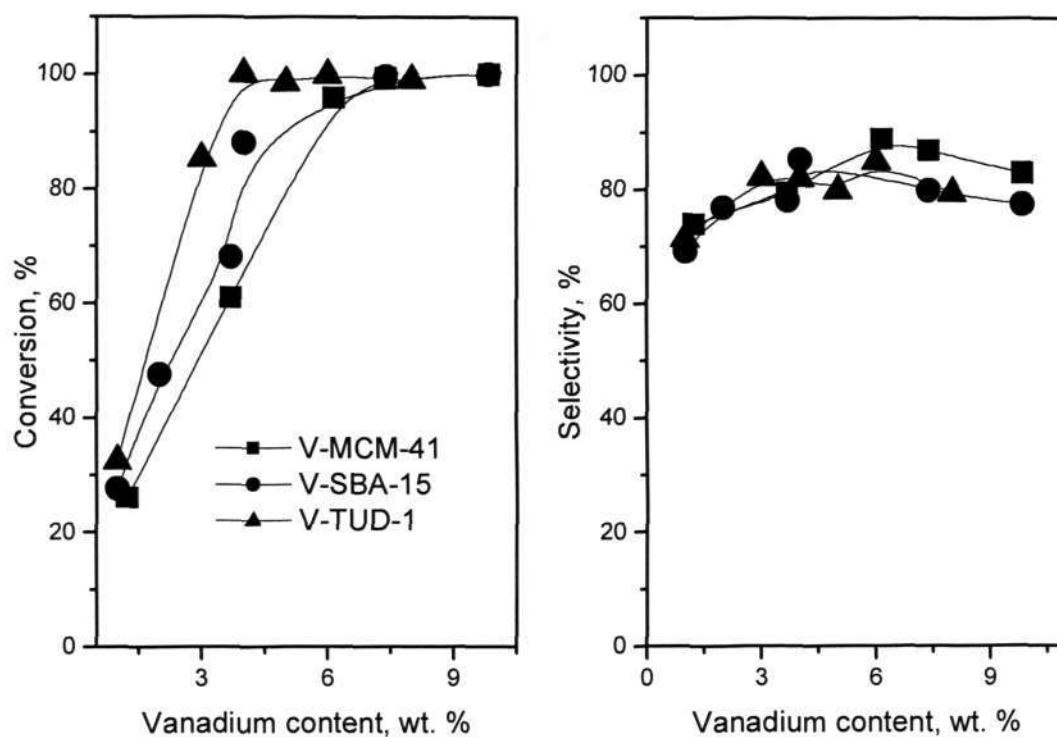


Figure 4.5 Conversion and selectivity of *trans*-stilbene epoxidation over V-MCM-41, V-SBA-15, and V-TUD-1 with different vanadium loadings. The reaction condition: 338K, 24h, 1 atm.

The influence of reaction time on the conversion and selectivity of *trans*-stilbene epoxidation is shown in Figure 4.6. In order to avoid the complication raised from the vanadium dispersion, 3wt.% vanadium content was chosen as the mode catalysts. The initial conversion is almost identical for V-MCM-41, V-SBA-15 and V-TUD-1 catalysts.

The *trans*-stilbene conversion shows a linear increase with reaction time, indicating that the *t*-butyl hydroperoxide enters the channels of vanadium-grafted catalysts, reacting with the vanadium to form vanadium peroxo radicals.⁴⁸ The long-term conversion follows the sequence: V-TUD-1>V-SBA-15>MCM-41, further supporting the effect of pore size and pore structure on the catalytic activity. The selectivity to epoxide increases with time as well for all the catalysts. V-TUD-1 exhibits the highest selectivity towards epoxide, implying that V-TUD-1 catalyst does not only enhance the conversion but also improve the *trans*-stilbene oxide selectivity due to its unique pore structure.

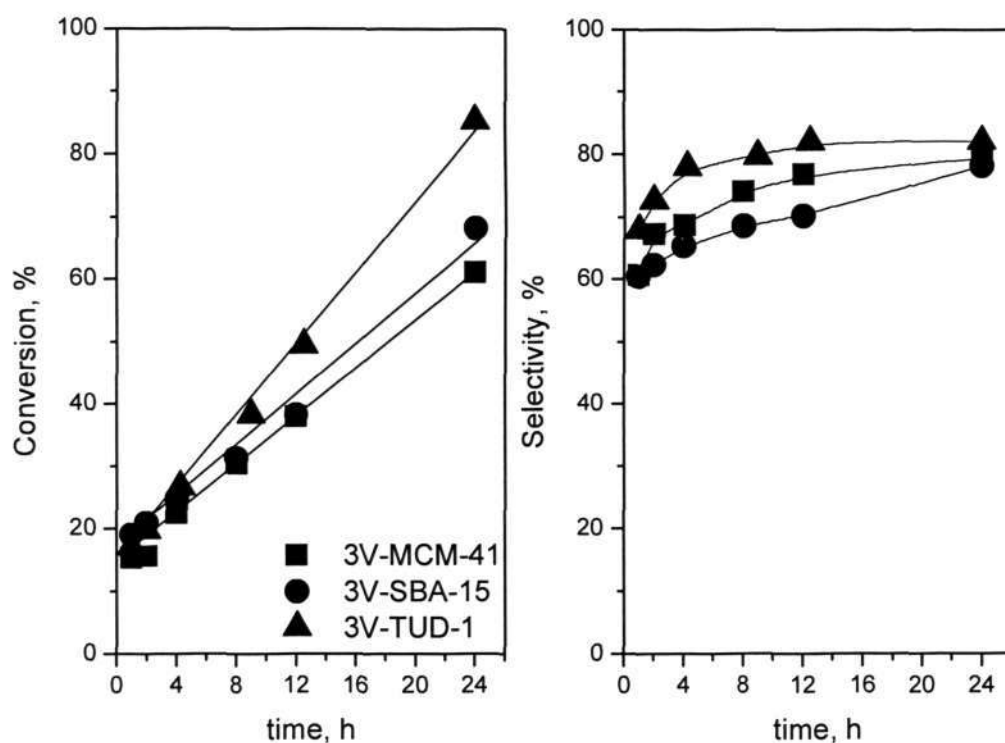


Figure 4.6 Conversion and selectivity of *trans*-stilbene epoxidation over 3V-MCM-41, 3V-SBA-15, and 3V-TUD-1 with reaction time. The reaction condition: 338K, 1 atm and 3wt% vanadium.

Reaction temperature is an important factor controlling the catalytic reaction. Figure 4.7 shows the conversion along with the epoxide selectivity increases with the temperature. The *trans*-stilbene epoxidation is an endothermic reaction and high temperature is favorable to the reaction and thus results in an increase of the *trans*-

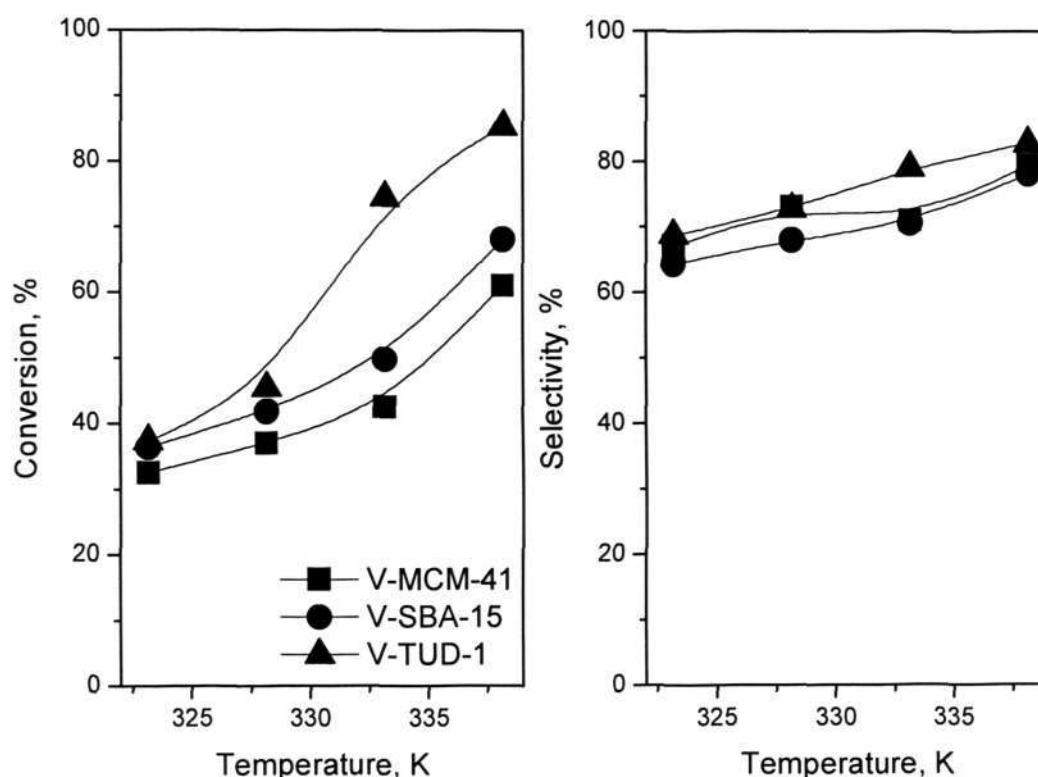


Figure 4.7 Conversion and selectivity of *trans*-stilbene epoxidation over 3V-MCM-41, 3V-SBA-15, and 3V-TUD-1 as a function of temperature. The reaction condition: 24h, 1 atm, 3 wt.% vanadium.

trans-stilbene conversion. V-TUD-1 shows the highest conversion among three catalysts. The best conversion of 87% is achieved over 3V-TUD-1 at 338K with the *trans*-stilbene oxide selectivity of 83%. The conversion follows the order V-TUD-1 > V-SBA-

15>MCM-41, further supporting the diffusion effect of the pore size and pore structure of the catalysts. The selectivity to epoxide increases with time for all the catalysts. The selectivity shows the sequence: V-TUD-1>V-MCM-41>V-SBA-15, implying that V-TUD-1c catalyst does not only enhance the conversion but also improve the *trans*-stilbene oxide selectivity.

4.2.2 *cis*-Cyclooctene Epoxidation

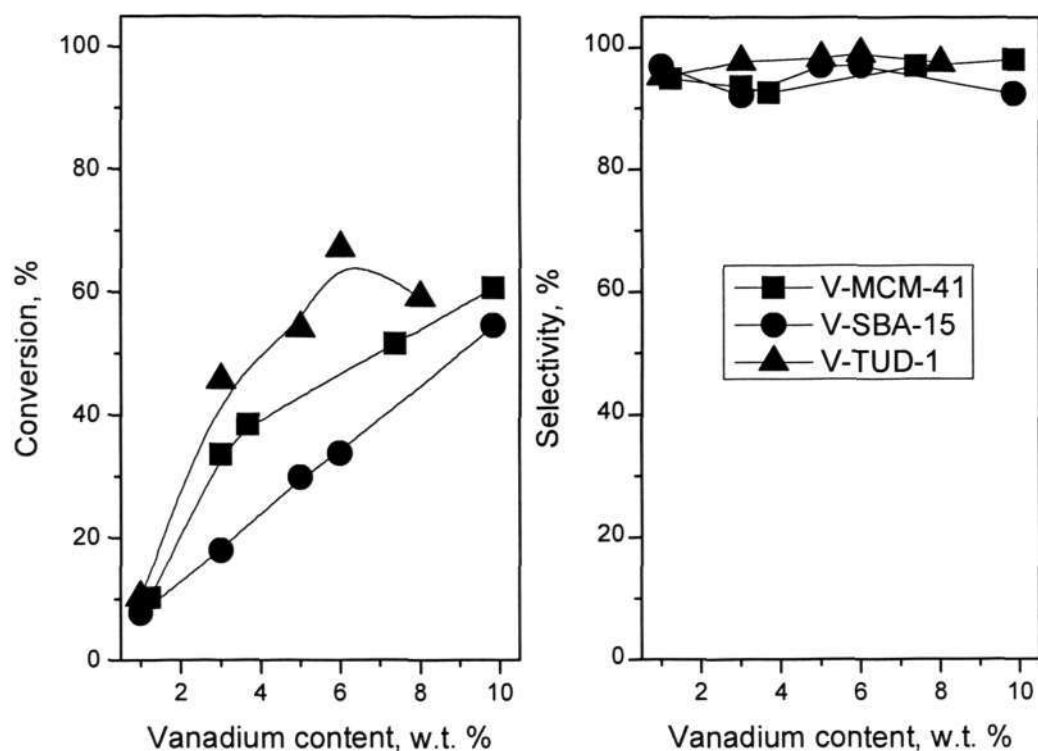


Figure 4.8 Conversion and selectivity of *cis*-cyclooctene epoxidation over V-MCM-41, V-SBA-15, and V-TUD-1 with vanadium loadings. The reaction condition: 338K, 24h, 1atm.

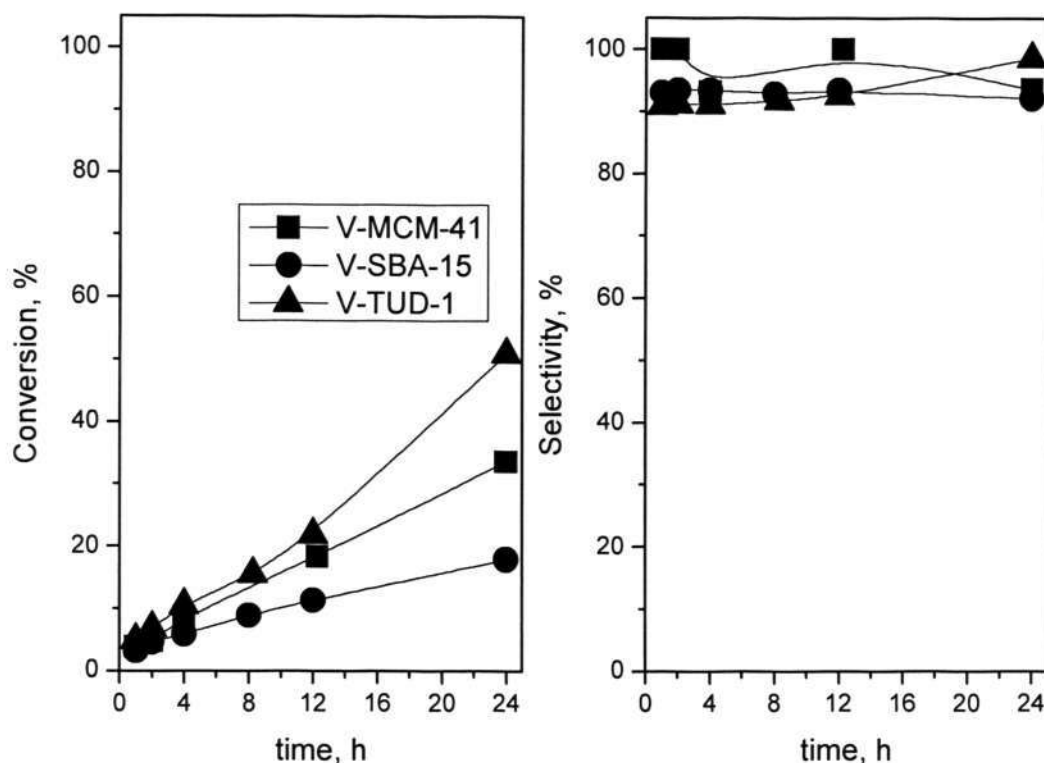


Figure 4.9 Conversion and selectivity of *cis*-cyclooctene epoxidation over 3V-MCM-41, 3V-SBA-15, and 3V-TUD-1 with reaction time. The reaction condition: 338K, 1 atm, 3 wt. % vanadium.

In this study, *cis*-cyclooctene epoxidation was selected as the other model reaction to complement *trans*-stilbene epoxidation, probing the structure effect on the catalytic reaction of bulky molecules in liquid phase. Figure 4.8 shows the effect of vanadium loading on catalytic performance of *cis*-cyclooctene epoxidation over vanadium grafted catalysts. The conversion of *cis*-cyclooctene increases with vanadium loadings. With the same vanadium content, V-TUD-1 catalysts always display the highest conversion. However, the *cis*-cyclooctene conversion over V-MCM-41 is higher than that of V-

SBA-15, which is different from that in *trans*-stilbene and other reports.⁴⁹ The conversion shows a decrease at high vanadium content of 8wt.% on V-TUD-1 catalyst. This may be due to that V_2O_5 crystallite forms and the dispersion of vanadium remarkably decreases. All the catalysts show high selectivity of *cis*-cyclooctene oxide above 90%. The selectivity over V-TUD-1 is slightly higher than over V-MCM-41 and V-SBA-15.

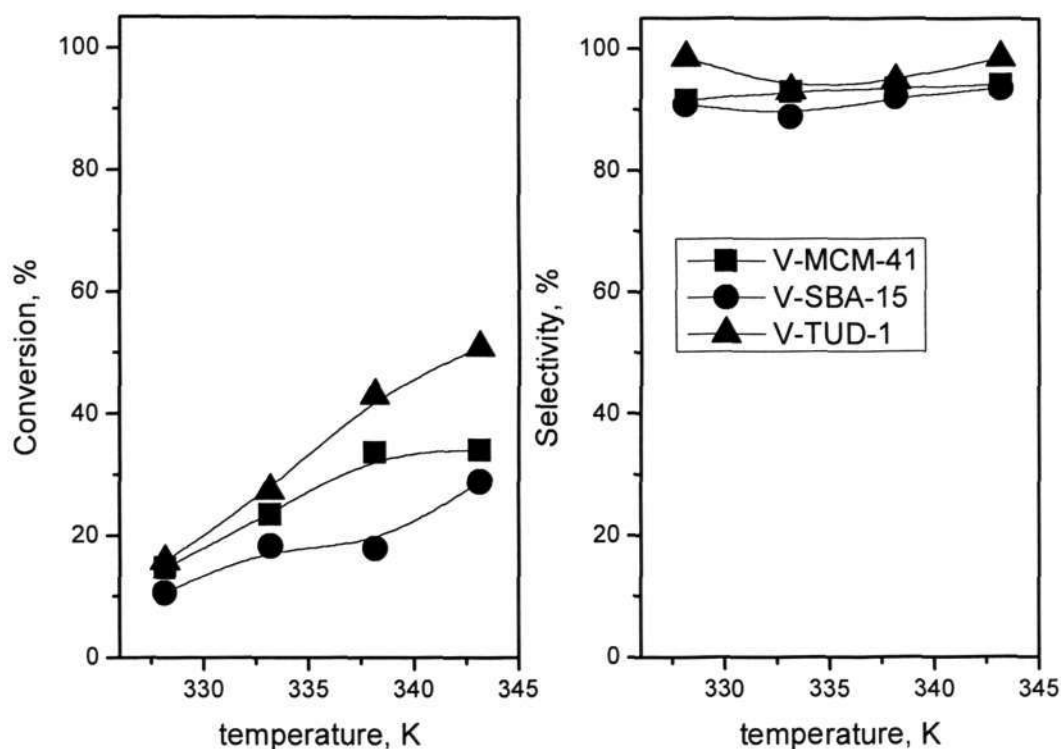


Figure 4.10 Conversion and selectivity of *cis*-cyclooctene epoxidation over 3V-MCM-41, 3V-SBA-15, and 3V-TUD-1 as a function of temperature. The reaction condition: 338K, 24h, 1 atm.

The influence of reaction temperature on the conversion and selectivity of *cis*-cyclooctene epoxidation over 3wt.% catalysts is revealed in Figure 4.9. For all the

grafted catalysts, the *cis*-cyclooctene conversion shows the linear increase with reaction time. Similar to the *trans*-stilbene epoxidation, the V-TUD-1 catalyst with a 3-D structure shows the highest catalytic activities. The *cis*-cyclooctene oxide selectivity on all the catalysts remains above 90%. Figure 4.10 shows the reaction temperature effect on the conversion and selectivity of *cis*-cyclooctene epoxidation. As a result of the endothermic reaction, the conversion of *cis*-cyclooctene increases with reaction temperature for all three types of catalysts. The best conversion of 50.9% is achieved over 3V-TUD-1 with the epoxide selectivity of 98.6%.

4.3 Discussion on the Pore Structure and Pore Size Effect

The V/NaX with 3wt.% vanadium prepared by an impregnation method is used as an additional catalyst to study the effect of pore structure and pore size. In this study, all these model catalysts possess different pore sizes and structures: zeolite V/NaX is microporous materials, V-MCM-41 and V-SBA-15 are mesoporous materials with 2-D structures, V-SBA-15 has larger pore diameter than that of V-MCM-41, and V-TUD-1 is a mesoporous material with fully opened 3-D structure. The catalytic performance of various catalysts with constant vanadium content (3wt.%) is shown in Figure 4.11. The 3-D mesoporous catalyst V-TUD-1 shows the best conversion and epoxide selectivity. The 2-D mesoporous catalysts show better conversion and epoxide selectivity than those of zeolite catalyst. This supports our hypothesis that the widely opened three-dimensional pore structures of V-TUD-1 catalyst decrease the pore diffusion resistance on the reactants, allowing greater accessibility of the reactants to the active sites embedded on the pore wall surface.^{6,50} The microporous catalysts show poorer conversion than mesoporous catalysts which may be due to its small pore size, restricting the diffusion of the reactant. The conversion and epoxide selectivity of *cis*-cyclooctene

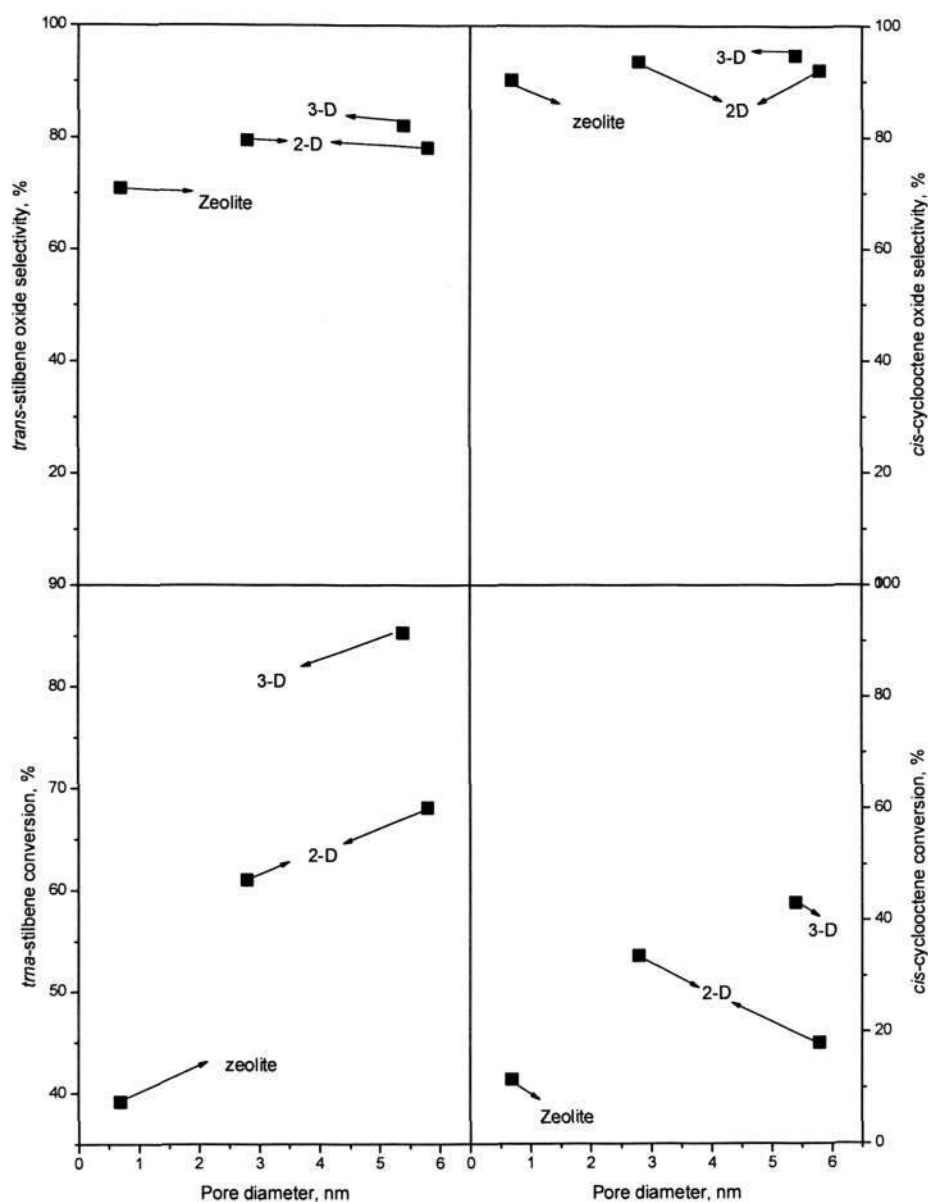


Figure 4.11 Pore structure and pore size effect on the *trans*-stilbene and *cis*-cyclooctene epoxidation. All the results were obtained under the condition of 338K, 24h, 1 atm and 3 wt. % vanadium.

epoxidation also follow the sequence 3-D>2-D>zeolite, which gives additional evidence on the conclusion of the pore structure effect on the catalytic reactions. Comparing between V-MCM-41 and V-SBA-15, V-SBA-15 shows better catalytic performance in *trans*-stilbene epoxidation, whereas V-MCM-41 shows better catalytic performance in *cis*-cyclooctene epoxidation. Although the reason remains unclear up to now, one possible explanation is that due to the steric effect, the molecular size of reactant has to be matched with the pore size of catalyst in order to gain the maximized catalytic activity.

4.4 Conclusion

Vanadium containing mesoporous materials (V-MCM-41, V-SBA-15, and V-TUD-1) were successfully synthesized by a controlled atomic layer deposition method. Their physicochemical properties were investigated by various characterization techniques including N₂-physisorption, X-ray diffraction, UV-vis spectroscopy, Raman spectroscopy, and X-ray absorption near-edge structure (XANES). The results revealed that the vanadium domains on these grafted mesoporous catalysts are mostly isolated VO₄ units with distorted tetrahedral coordination. Catalytic epoxidation of *trans*-stilbene and *cis*-cyclooctene were carried out as probe reactions to test the pore structure effect. Both reactions showed the best catalytic performance could be achieved over the V-TUD-1 catalyst with the unique 3-D pore structure.

References:

- (1) Karakoulia, S. A.; Triantafyllidis, K. S.; Lemonidou, A. A. In *2nd International Workshop of the European-Network-of-Excellence: In Situ Study and Development of Processes Involving NanoPORous Solids* Thessaloniki, GREECE, 2007, p 157.

- (2) Karakoulia, S. A.; Triantafyllidis, K. S.; Tsilomelekis, G.; Boghosian, S.; Lemonidou, A. A. *Catalysis Today, In Press, Corrected Proof*.
- (3) Tsoncheva, T.; Ivanova, L.; Dimitrova, R.; Rosenholm, J. *Journal of Colloid and Interface Science* **2008**, 321, 342.
- (4) Li, X. K.; Ji, W. H.; Zhao, J.; Zhang, Z.; Au, C. T. *Applied Catalysis a-General* **2006**, 306, 8.
- (5) Hu, Y. F.; Wang, S. X.; Guo, X. W.; Li, S. L.; Hu, S.; Sun, H. B.; Bai, L. *Catalysis Letters* **2005**, 100, 59.
- (6) Tang, Q.; Wang, C.; Hu, S.; Sun, H.; Chen, Y.; Haller, G.; Yang, Y. *Catalysis Letters* **2007**, 117, 25.
- (7) Chouyyok, W.; Panpranot, J.; Thanachayanant, C.; Prichanont, S. *Journal of Molecular Catalysis B: Enzymatic* **2009**, 56, 246.
- (8) Selvam, P.; Bhatia, S. K.; Sonwane, C. G. *Industrial & Engineering Chemistry Research* **2001**, 40, 3237.
- (9) Casci, J. L. *Advanced Zeolite Science and Applications* **1994**, 85, 329.
- (10) Ciesla, U.; Schuth, F. *Microporous and Mesoporous Materials* **1999**, 27, 131.
- (11) Fenelonov, V. B.; Romannikov, V. N.; Derevyankin, A. L. *Microporous and Mesoporous Materials* **1999**, 27, 131.
- (12) Lin, H. P.; Mou, C. Y. *Accounts of Chemical Research* **2002**, 35, 927.
- (13) Menon, V. C.; Komarneni, S. *Journal of Porous Materials* **1998**, 5, 43.
- (14) Oye, G.; Sjoblom, J.; Stocker, M. *Advances in Colloid and Interface Science* **2001**, 89, 439.
- (15) Pang, J. B.; Qiu, K. Y.; Wei, Y. *Journal of Inorganic Materials* **2002**, 17, 665.
- (16) Raman, N. K.; Anderson, M. T.; Brinker, C. J. *Chemistry of Materials* **1996**, 8, 1682.
- (17) Taguchi, A.; Schuth, F. *Microporous and Mesoporous Materials* **2005**, 77, 1.
- (18) Sayari, A. *Chemistry of Materials* **1996**, 8, 1840.
- (19) Zhao, D. Y.; Feng, J. L.; Huo, Q. S.; Melosh, N.; Fredrickson, G. H.; Chmelka, B. F.; Stucky, G. D. *Science* **1998**, 279, 548.

- (20) Zhao, D.; Huo, Q.; Feng, J.; Chmelka, B. F.; Stucky, G. D. *Journal of the American Chemical Society* **1998**, *120*, 6024.
- (21) Anand, R.; Hamdy, M. S.; Gkourgkoulas, P.; Maschmeyer, T.; Jansen, J. C.; Hanefeld, U. *Catalysis Today* **2006**, *117*, 279.
- (22) Shan, Z.; Jansen, J. C.; Zhou, W.; Maschmeyer, T. *Applied Catalysis A: General* **2003**, *254*, 339.
- (23) Jansen, J. C.; Shan, Z.; Marchese, L.; Zhou, W.; von der Puil, N.; Maschmeyer, T. *Chemical Communications* **2001**, 713.
- (24) Selvaraj, M.; Lee, T. G. *The Journal of Physical Chemistry B* **2006**, *110*, 21793.
- (25) Selvaraj, M.; Song, S. W.; Kawi, S. *Microporous and Mesoporous Materials* **2008**, *110*, 472.
- (26) Li, Z.; Zhang, W.; Yamamoto, H. *Angewandte Chemie-International Edition* **2008**, *47*, 7520.
- (27) Zhang, Q. H.; Wang, Y.; Itsuki, S.; Shishido, T.; Takehira, K. *Journal of Molecular Catalysis a-Chemical* **2002**, *188*, 189.
- (28) Gao, X.; Bare, S. R.; Weckhuysen, B. M.; Wachs, I. E. *The Journal of Physical Chemistry B* **1998**, *102*, 10842.
- (29) Inumaru, K.; Misono, M.; Okuhara, T. *Applied Catalysis A: General* **1997**, *149*, 133.
- (30) Busca, G.; Centi, G.; Marchetti, L.; Trifiro, F. *Langmuir* **1986**, *2*, 568.
- (31) Das, N.; Eckert, H.; Hu, H.; Wachs, I. E.; Walzer, J. F.; Feher, F. J. *The Journal of Physical Chemistry* **1993**, *97*, 8240.
- (32) Koranne, M. M.; Goodwin, J. G.; Marcelin, G. *Journal of Catalysis* **1994**, *148*, 369.
- (33) Du, G. A.; Lim, S. Y.; Yang, Y. H.; Wang, C.; Pfefferle, L.; Haller, G. L. *Applied Catalysis a-General* **2006**, *302*, 48.
- (34) Hu, S.; Liu, D.; Li, L.; Borgna, A.; Yang, Y. *Catalysis Letters* **2009**, *129*, 478.
- (35) Du, G.; Lim, S.; Pinault, M.; Wang, C.; Fang, F.; Pfefferle, L.; Haller, G. L. *Journal of Catalysis* **2008**, *253*, 74.
- (36) Corma, A. *Chem. Rev.* **1997**, *97*, 2373.

- (37) Vinu, A.; Sawant, D. P.; Ariga, K.; Hossain, K. Z.; Halligudi, S. B.; Hartmann, M.; Nomura, M. *Chemistry of Materials* **2005**, *17*, 5339.
- (38) Hamdy, M. S.; Ramanathan, A.; Maschmeyer, T.; Hanefeld, U.; Jansen, J. C. *Chemistry-a European Journal* **2006**, *12*, 1782.
- (39) Schmidt, R.; Hansen, E. W.; Stoecker, M.; Akporiaye, D.; Ellestad, O. H. *Journal of the American Chemical Society* **1995**, *117*, 4049.
- (40) Yang, Y. H.; Du, G. A.; Lim, S. Y.; Haller, G. L. *Journal of Catalysis* **2005**, *234*, 318.
- (41) Shylesh, S.; Singh, A. R. *Journal of Catalysis* **2006**, *244*, 52.
- (42) Solsona, B.; Blasco, T.; Nieto, J. M. L.; Pena, M. L.; Rey, F.; Vidal-Moya, A. *Journal of Catalysis* **2001**, *203*, 443.
- (43) Wei, D.; Wang, H.; Feng, X.; Chueh, W.-T.; Ravikovitch, P.; Lyubovsky, M.; Li, C.; Takeguchi, T.; Haller, G. L. *The Journal of Physical Chemistry B* **1999**, *103*, 2113.
- (44) Das, N.; Eckert, H.; Hu, H. C.; Wachs, I. E.; Walzer, J. F.; Feher, F. J. *Journal of Physical Chemistry* **1993**, *97*, 8240.
- (45) Davidson, A.; Che, M. *J. Phys. Chem.* **1992**, *96*, 9909.
- (46) Went, G. T.; Oyama, S. T.; Bell, A. T. *J. Phys. Chem.* **1990**, *94*, 4240.
- (47) Wong, J.; Lytle, F. W.; Messmer, R. P.; Maylotte, D. H. *Physical Review B* **1984**, *30*, 5596.
- (48) Selvaraj, M.; Seshadri, K. S.; Pandurangan, A.; Lee, T. G. *Microporous and Mesoporous Materials* **2005**, *79*, 261.
- (49) Celestin Bakala, P.; Briot, E.; Salles, L.; Bregeault, J.-M. *Applied Catalysis A: General* **2006**, *300*, 91.
- (50) Quek, X.-Y.; Tang, Q.; Hu, S.; Yang, Y. *Applied Catalysis A: General* **2009**, *361*, 130.

Chapter 5 Preparation, Characterization and Catalytic Properties of Vanadium Exchanged X Faujasite Zeolites for the Epoxidation Reaction of *trans*-Stilbene and *cis*-Cyclooctene

Several reports on epoxidation employed mesoporous materials as supports due to their high surface area and large pore diameter.^{1,2} However, the preparation of mesoporous materials is time-consuming and not economical in view of industrial application. As the crystalline microporous zeolites containing transition metal ions are well established catalysts with remarkable catalytic properties in oxidation reactions.^{3,4} study on using commercially available X faujasite zeolite as support of vanadium catalyst for epoxidation will be more feasible towards the applied catalysis in industrial applications.

The incorporation of vanadium cations into the zeolite lattice has been considered as a challenge for a long time. Only a minor fraction of the vanadium ions can be incorporated into the zeolite framework during the direct hydrothermal synthesis.⁵ A large amount of crystalline V_2O_5 would be formed using the solid-state ion-exchange method.⁶ Dzwigaj et al. employed $VOSO_4$ as vanadium precursor for ion-exchange under an acid condition, and the highest content of 2.0 wt. % vanadium within BEA zeolite can be achieved.^{3,7} However, the content of vanadium cannot be further increased due to the participation of additional H^+ exchange. Tang et al. successfully applied the liquid ion-exchange to introduce metal oxides CoO_x into faujasite zeolite and the highest cobalt loading was reported as 8.8 wt.%⁸.

The activity and selectivity of vanadium oxide catalysts are mainly attributed to the oxidation state, local coordination, dispersion, and the accessibility of the active centers. It was reported that both V^{5+} and/or V^{4+} are incorporated in either tetrahedral or square pyramidal coordination by framework substitution.^{7,9} The calcination also plays a vital

role in locating the cations in zeolites.⁹ Most of the current studies focused on the distribution of vanadium species in zeolite after calcination, the location of the vanadium in the zeolite before calcination remains unclear.^{3,7,9,10} Furthermore, to the best of our knowledge, no investigation was reported on the insight into the vanadium catalytic active sites, prepared by ion-exchange method, in faujasite (FAU) zeolite framework which consists of sodalite cages (truncated cuboctahedra) linked by double six-rings (D6Rs).¹¹

In this capture, an ion-exchange method under basic environment is reported to prepare the vanadium-containing FAU zeolite catalysts. Both as-synthesized and calcined vanadium catalysts are applied in epoxidation reaction to examine the catalytic properties. The effect of calcination on the catalytic performance will be discussed in detail with the objective to elucidate the migration of vanadium cations upon the calcination.

5.1 Catalysts Characterization

5.1.1 Degree of Exchange and Vanadium Content

The amount of vanadium ions in aqueous solution available for ion-exchange and the numbers of exchangeable sites (Na^+) in zeolites as well as the exchange efficiency would affect the degree of exchange and the vanadium content. As expected, with a fixed amount of zeolite and a fixed volume of solution employed for ion-exchange, the degree of exchange and thus the vanadium content can be regulated by changing the concentration of the vanadium solution which is similar with the reported Co-X zeolite.⁸ Table 5.1 shows the degree of exchange and the content of vanadium incorporated in each sample synthesized in this study. At a very low concentration of the VOSO_4 precursor solution, almost all the vanadium ions can be incorporated into the zeolite

support. Increased concentration of VOSO_4 raises the degree of exchange and the vanadium content in the final sample. However, the proportion of vanadium ions incorporated into zeolite declines. The highest vanadium content can be achieved in this study is 4.85 wt.%, which is higher than those reported previously.³ This may be due to the alkali environment of the solution decreases the H^+ competition in the ion exchange.

Table 5.1. Vanadium Content in samples^a

sample ^b	Concentration of VOSO_4 in ion exchange (M)	Expected V content in samples ^c (wt.%)	Proportion of V incorpated	Actual content in samples
1V-X and 1V-X(C)	0.008	1	95	0.95
3V-X and 3V-X(C)	0.024	3	88.7	2.66
6V-X and 6V-X(C)	0.047	6	80.8	4.85

^a Typical condition for ion exchange: Na-X, 2.0 g; volume of VOSO_4 solution, 50ml.

^b The number before V denotes the expected vanadium content in weight percentage.

^c the vanadium content when the vanadium was fully exchanged into the zeolite.

5.1.2 XRD Patterns

The powder XRD patterns ofV -X and V-X(C) catalysts are shown in Figure 5.1. Both V-X and V-X(C) exhibit excellent crystallinity with almost identical diffraction pattern to that of NaX($\text{Na}_2\text{Al}_2\text{Si}_{2.5}\text{O}_9 \bullet 6.2\text{H}_2\text{O}$ X RDP DF card #00-038-0237),

indicating that X zeolite structure is well preserved upon vanadium incorporation. No additional noticeable diffraction peaks are discerned, implying the absence of crystalline

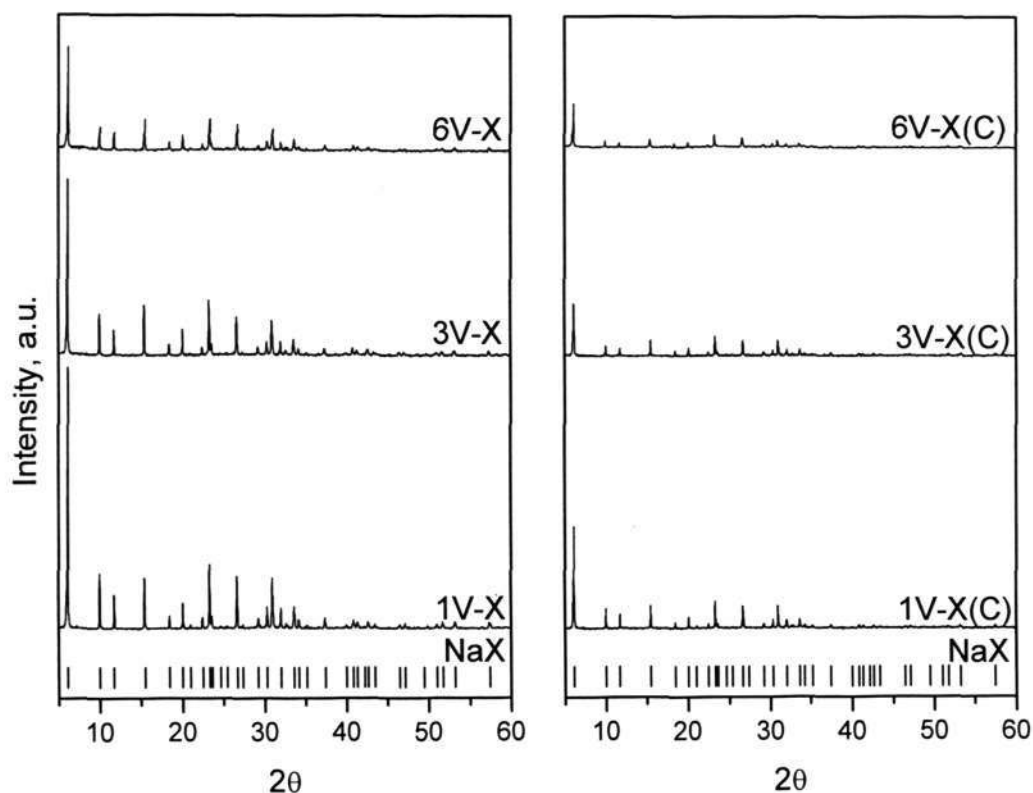


Figure 5.1 XRD patterns of the V-X and V-X(C) samples, the signal of NaX shown at the bottom was assigned to zeolite X ($\text{Na}_2\text{Al}_2\text{Si}_{12}\text{O}_{54} \cdot 6.2\text{H}_2\text{O}$, PDF card #00-038-0237).

vanadium oxide even at high vanadium loading. The XRD signal strength decreases with the increase of vanadium content, which may suggest that the vanadium cations incorporate into the framework and decrease the long-range order structure of the X zeolite. V-X(C) samples show lower intensity diffraction peaks compared to V-X samples with the same vanadium content. The possible sites for vanadium in FAU zeolite are in the supercage, SOD cage and D6Rs units. In VOSO_4 precursor solution,

VO^{2+} ion is usually in hydrated form $[\text{VO}(\text{H}_2\text{O})_2]^{2+}$ with a larger diameter than the six-membered rings in zeolite, the chance for vanadium cations to access the SOD cages and D6Rs units will be reduced to a great extent. Thus the proposed vanadium sites are in the supercage of the FAU zeolite in the V-X samples. The calcination may cause the vanadium to migrate to enter the smaller cages, such as SOD cages, as the hydration water can be removed under high-temperature pretreatment, resulting in the distortion of the zeolite framework.

5.1.3 Diffuse Reflectance UV-vis and UV-Raman Spectroscopy

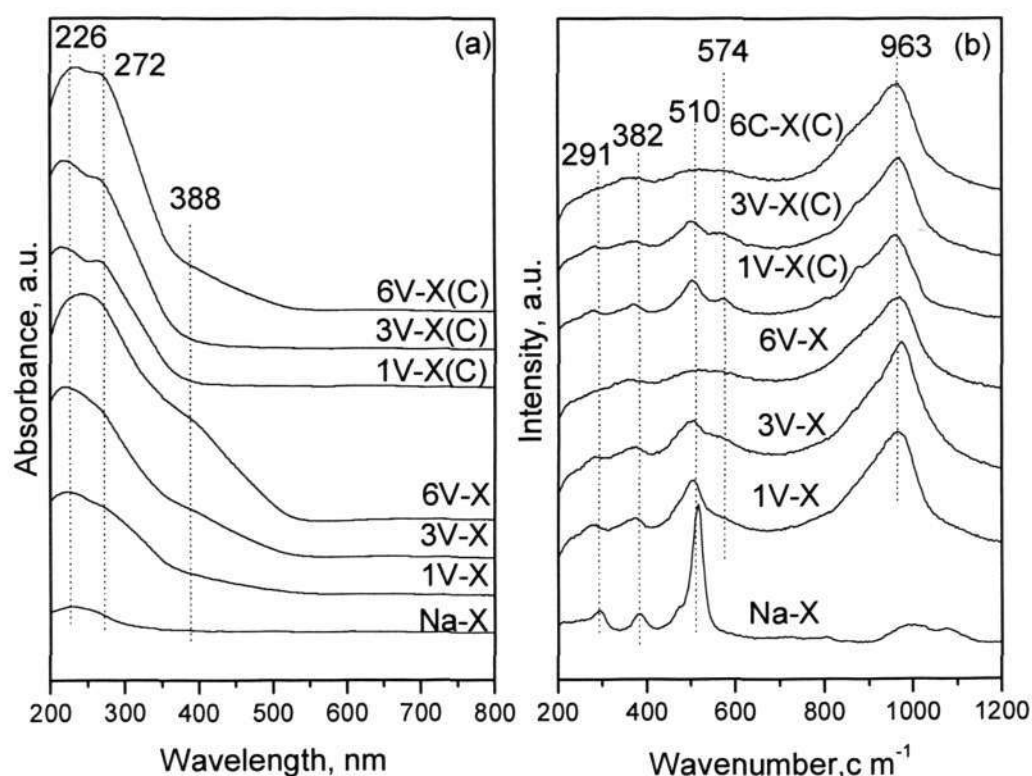


Figure 5.2 (a) UV-Vis spectra of the V-X and V-X(C) samples; (b) UV-Raman spectra of V-X and V-X(C) samples.

UV-vis spectroscopy is widely used to reveal the local environment of metal cations in an oxide domain. In this study, diffuse reflectance UV-vis spectra of V-X and V-X(C) samples are shown in Figure 5.2(a). Except for the peak around 226 nm, there is no significant absorbance for the parent FAU zeolite, showing the signals between 250 and 800 nm can be attributed to the vanadium species. The band at 273 nm attributed to V^{5+} in tetrahedral coordination is detected in all the V-X and V-X(C) samples.¹²⁻¹⁵ The formation of V^{5+} in the V-X samples is due to that the VO^{2+} cations in $VOSO_4$ precursors can be easily oxidized to V^{5+} in alkali environment when exposed to air.¹⁶ The band at 388 nm, ascribed to the tetrahedral V^{5+} coordinated with additional water, is detected as the vanadium content increases in V-X samples.^{12,14,17,18} Additionally, the vanadium supported on zeolite does not show any absorbance in the range of 600-800 nm, implying the lack of the characteristic d-d transitions of $(VO)^{2+}$ on the surface of the catalysts.¹⁷ The V-X and V-X(C) samples with high vanadium loading turn yellow when exposed to air. No signal is observed between 320 and 450 nm, indicating there is no polymeric V-O-V bond and V_2O_5 crystallites in the V-X and V-X(C) samples.¹⁴

UV-Raman spectroscopy is a powerful tool for elucidating the molecular nature of materials, particularly useful for zeolite materials.¹⁹ The Raman spectra of V-X and V-X(C) samples are shown in Figure 5.2(b). All the vanadium supported on zeolite samples show a strong broad Raman band around 963 cm^{-1} assignable to the symmetric V-O stretching in pseudo-tetrahedral $O=V-(O-S)_3$ ($S=Si$ or Al).^{20,21} As the samples are hydrated under ambient condition, the $V=O\cdots H$ resonance under UV excitation causes the disappearance of terminal $V=O$ stretching bands in the range of $990-1050\text{ cm}^{-1}$.²¹ The absence of the typical band at 995 cm^{-1} of V_2O_5 fingerprint in all the samples indicates no crystalline V_2O_5 existent,¹⁵ which is coincident with the results of UV-vis spectra. There is a weak peak detectable at 574 cm^{-1} which attributes to the symmetric

V-O-V stretching,²¹ implying the vanadium is partly polymeric VO_x species on the X zeolite after calcination. The remaining Raman bands at 291, 382 and 510 cm^{-1} are resulted from parent NaX zeolite.

5.1.4 XANES

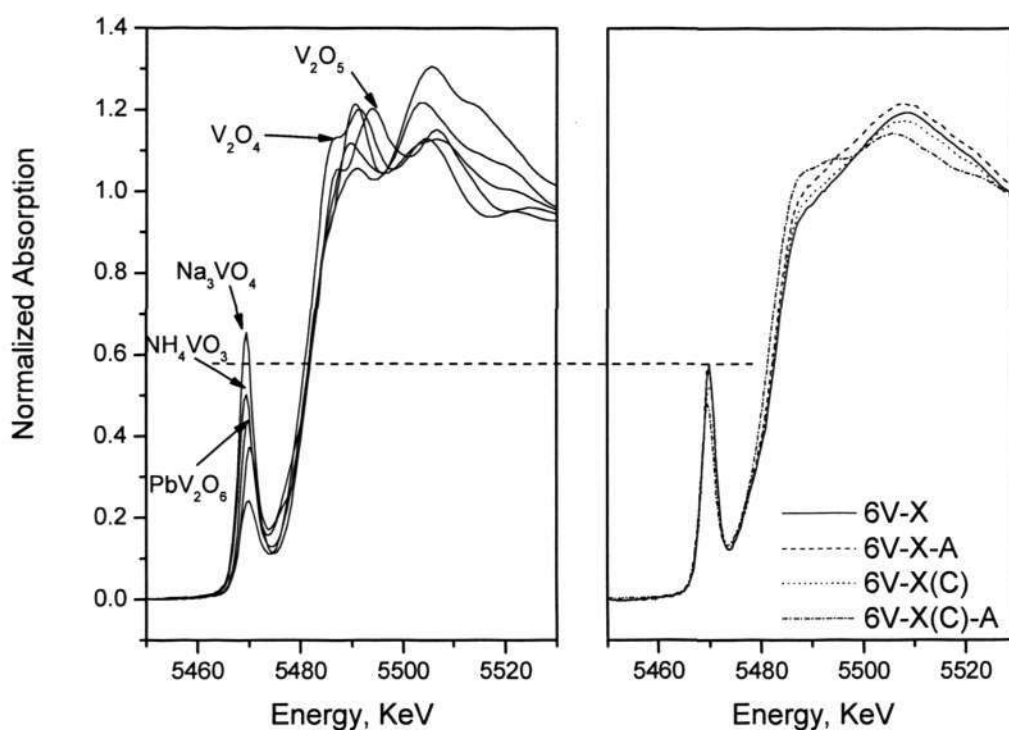


Figure 5.3 The normalized XANES spectra at V K-edge for reference compounds, 6V-X, 6V-X(C) as well as the used samples 6V-X-A and 6V-X(C)-A.

The normalized XANES spectra at vanadium k-edge for the V-X and V-X(C) samples as well as the reference compounds are illustrated in Figure 5.3. The XANES regions for all the vanadium ion-exchanged zeolite samples are indistinguishable, implying the similar electronic structures and site symmetries for the vanadium sites in various samples.^{22,23} It is known that the pre-edge peak height and intensity are closely related to the local symmetry type, and they can be employed to gain insight into the

coordination structure when comparing with the model compounds of specific coordination environment. The pre-edge peak height monotonically decreases as the vanadium structure changes from tetrahedral too ctahedral coordinatona nd square pyramidal. Ass hown in Figure 5.3, the pre-edge peak height of vanadium domain in various samples lay between those of reference compound Na_3VO_4 (tetrahedral) and NH_4VO_3 (distorted tetrahedral), evidencing a distorted tetrahedral coordination for the

Table 5.2, Energy positions of various spectral features in the V K-edge XANES spectra

Sample	Pre-edge peak position ^a (eV)	Main-edge position ^{a,b} (eV)	$E_{\text{pre-edge}} - E_0$ (eV)	$E_{\text{edge}} - E_{\text{pre-edge}}$ (eV)	Pre-edge peak height (a.u.)	Pre-edge peak intensity ^c (a.u.)
Na_3VO_4	5469.5	5482.0	4.5	12.5	0.65	2.37
NH_4VO_3	5469.5	5481.3	4.5	11.8	0.50	2.03
PbV_3O_9	5469.5	5481.1	4.5	11.6	0.44	1.79
V_2O_5	5469.9	5480.1	4.9	10.2	0.37	1.58
V_2O_4	5469.9	5478.3	4.9	8.4	0.24	1.31
6V-X	5469.9	5482.2	4.9	12.3	0.52	1.73
6V-X-A ^d	5469.5	5482.2	4.5	12.3	0.48	1.66
6V-X(C)	5469.9	5481.7	4.9	11.8	0.58	1.83
6V-X(C)-A ^d	5469.9	5482.0	4.9	12.1	0.57	1.88

^a The uncertainty in peak position is estimated to be $\pm 0.4\text{eV}$.

^b Main edge position is chosen as the mid point of absorption jump

^c Peak intensity is calculated by peak height * width at half maximum

^d the samples after epoxidation reaction

vanadium ion exchanged samples.²³ The quantitative XANES results of vanadium-containing samples and reference compounds are summarized in Table 5.2. The distance between the pre-edge energy and the main edge energy is a measurement of the oxidation state of vanadium.²² The $E_{\text{edge}}-E_{\text{pre-edge}}$ value for V^{5+} is greater than 10.7 eV as in V_2O_5 , and this value decreases with lower oxidation states vanadium such as V_2O_4 ($E_{\text{edge}}-E_{\text{pre-edge}} = 9.5$ eV). The $E_{\text{edge}}-E_{\text{pre-edge}}$ values of 6V-X and 6V-X(C) samples are 12.3 and 11.8 eV, respectively, suggesting the vanadium cations are in V^{5+} state which is consistent with the result of UV-vis and UV-Raman spectra. The pre-edge peak intensity has been found to be correlated to the size of “molecular cage”.²² The results summarized in Table 5.2 exhibit that the pre-edge intensities are between the values of NH_4VO_3 and V_2O_5 , suggesting that the vanadium domains are of cage size between those of NH_4VO_3 and V_2O_5 , which confirms the V^{5+} valence in these samples.

5.2 Catalytic Performances in *trans*-Stilbene Epoxidation and *cis*-Cyclooctene Epoxidation

The catalytic epoxidation process is the same with the part of section 4.2.

5.2.1 Catalytic Performances in *trans*-Stilbene Epoxidation

The results of *trans*-stilbene epoxidation for 24 h over V-X and V-X(C) catalysts with different vanadium contents are presented in Figure 5.4. Parent zeolite support presents about 17% conversion and 70 % selectivity towards stilbene oxide. The conversion of *trans*-stilbene shows a linear increase over V-X catalyst respect to the vanadium loading and remains at a constant conversion of 95 % with the vanadium content greater than 3 wt.%, directly suggesting that the vanadium active centers are highly dispersed supported on zeolite. The stilbene oxide selectivity slightly increases with the vanadium content no more than 3 wt.%, while the benzaldehyde selectivity

decreases. The selectivity remains stable at 85 %, 12 %, and 2.9 % towards stilbene oxide, benzaldehyde, and benzoic acid, respectively under high vanadium loadings. The vanadium sites are more favorable to stilbene oxide, which suggests the V^{5+} centers act

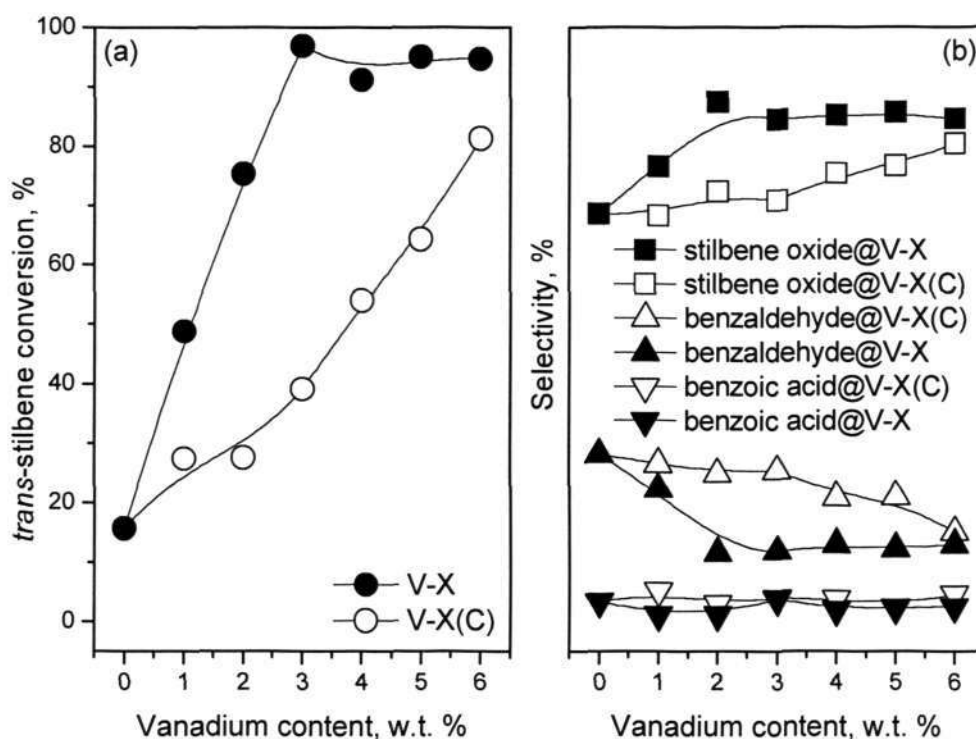


Figure 5.4 (a) *trans*-stilbene conversion on V-X and V-X(C) samples with different vanadium loading; (b) selectivity of *trans*-stilbene oxide, benzaldehyde, and benzoic acid over V-X and V-X(C) samples with different vanadium loading. The reaction condition: 338K, 24h, 1 atm.

as a base in the zeolite to decline the selectivity towards benzaldehyde. The selectivity of benzoic acid remains at a low level, indicating the mild acid strength. For the calcined vanadium catalysts V-X(C), a similar trend appears in the conversion and

selectivity except that both the conversion and stilbene oxide selectivity are remarkably lower compared to the V-X catalyst. As we discussed in the characterization results, both as-synthesized and calcined catalysts show the similar characteristics of vanadium active centers, e.g., oxidation state, local coordination, the difference in the catalytic activity over these two catalysts can be explained that the calcination may cause the migration of vanadium sites from supercage to SOD cage, the lower conversion in V-X(C) sample may be due to that the vanadium sites in the smaller SOD cage are less accessible to the reactant of *trans*-stilbene and TBHP molecules.

To further probe the confinement effect of zeolite channels, Figure 5.5 shows the initial reaction rates of *trans*-stilbene epoxidation using TBHP over 3V-X and 3V-X(C) catalysts. 3V-X exhibits a slightly higher initial conversion compared to that of 3V-X(C). Reactions over both catalysts show a linear increase with time-on-stream, while the conversion over 3V-X increases more rapidly than over 3V-X(C). The dimension of zeolite pores should play a crucial role in controlling the reaction, TBHP enters the zeolite channels, reacting with vanadium to form vanadium peroxo radicals to initiate the epoxidation²⁴. As it is suggested, the vanadium species in V-X samples are mostly located in the supercage, it is easy for TBHP to enter and form the vanadium peroxo radicals, and whereas the vanadium in SOD cages in V-X(C) catalyst is hardly accessible to TBHP due to the small dimension of SOD cages. Both as-synthesized and calcined catalysts show the similar trend in the selectivities of stilbene oxide, benzaldehyde and benzoic acid. The selectivity towards stilbene oxide increases with reaction time, implying the gradually increased amount of peroxo radicals. The selectivity of benzaldehyde declines slowly while the decrease of benzoic acid selectivity is remarkable during the first 10 h. This can be due to the oxidation of *trans*-stilbene over abundant acid sites in the zeolite and the formation of peroxo radicals is

insufficient to complete the overall oxidation in the initial several hours. The 3V-X catalyst also shows constantly higher stilbene epoxide selectivity than that of 3V-X(C), indicating the V-X is a better epoxidation catalyst than V-X(C).

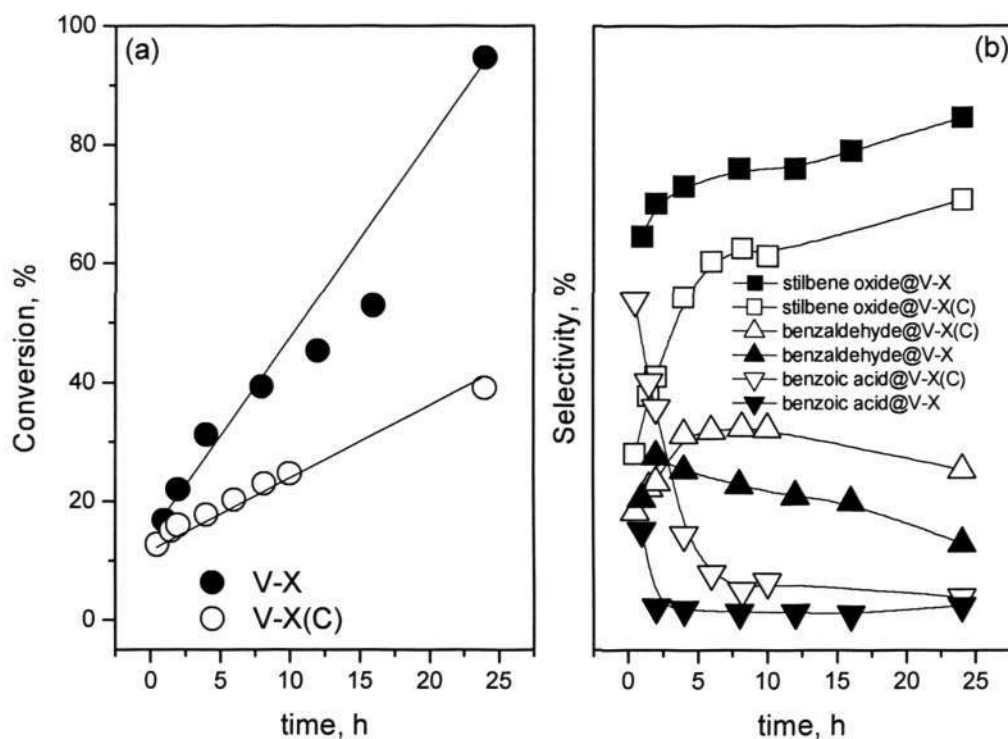


Figure 5.5 (a) *trans*-stilbene conversion change with different time over V-X and V-X(C) samples, (b) selectivity of *trans*-stilbene oxide, benzaldehyde, benzoic acid over V-X and V-X(C) samples with different time. The reaction condition: 338K, 1 atm, 3 wt.% vanadium.

Figure 5.6 shows the variation in *trans*-stilbene conversion and product selectivity with increasing the reaction temperature over 3 wt.% V-X and V-X(C) catalysts. The conversions increase with the temperature over both catalysts. The selectivities of stilbene epoxide also increase while the selectivities of benzaldehyde decrease. The

selectivities of benzoic acid slightly increase over the reaction temperature range. The *trans*-stilbene epoxidation is an endothermic reaction and high temperature would favor the reaction thus leading to the increase of conversion and selectivity. The V-X sample shows higher conversion and stilbene epoxide selectivity over all the temperatures with lower benzaldehyde selectivity and similar benzoic acid selectivity compared with the V-X(C) sample. Activation energies are also calculated as shown in Figure 5.10. The activation energies for *trans*-stilbene epoxidation over 3V-X and 3V-X(C) catalysts are 33.37 and 43.15 kJ/mol, respectively. The 3V-X catalyst shows lower activation energy than 3V-X(C), evidencing the reaction can be easily activated over the former catalyst.

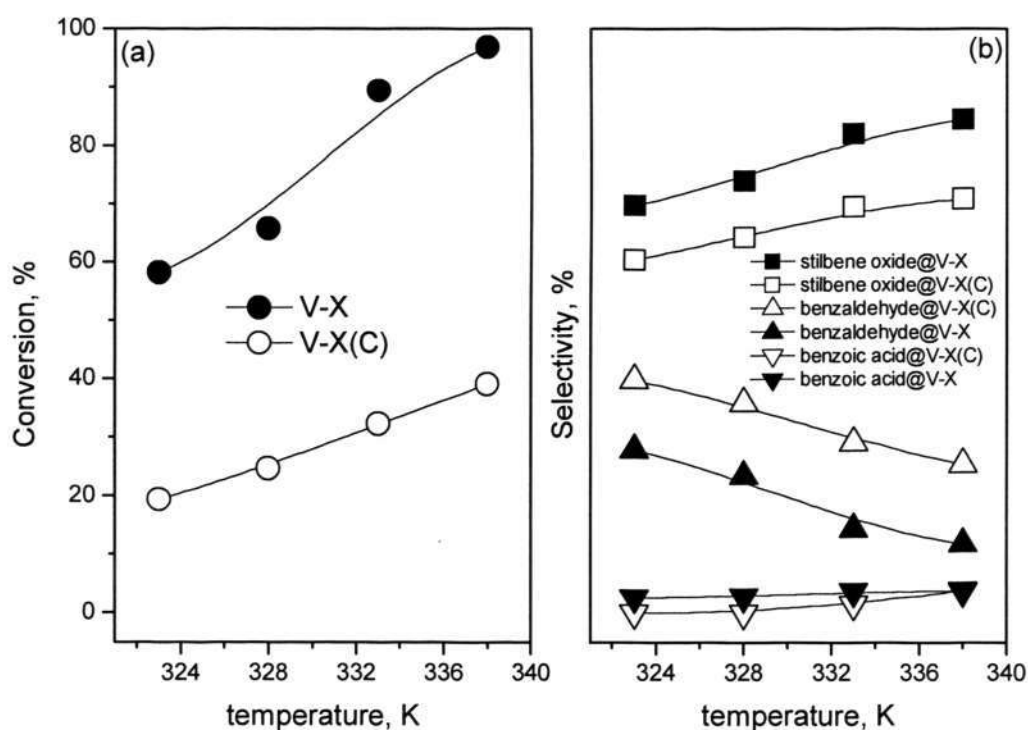


Figure 5.6 (a) *trans*-stilbene conversion change with different temperature, (b) selectivity of *trans*-stilbene oxide, benzaldehyde, benzoic acid with different temperature. The reaction condition: 24h, 1 atm, 3 wt.% vanadium.

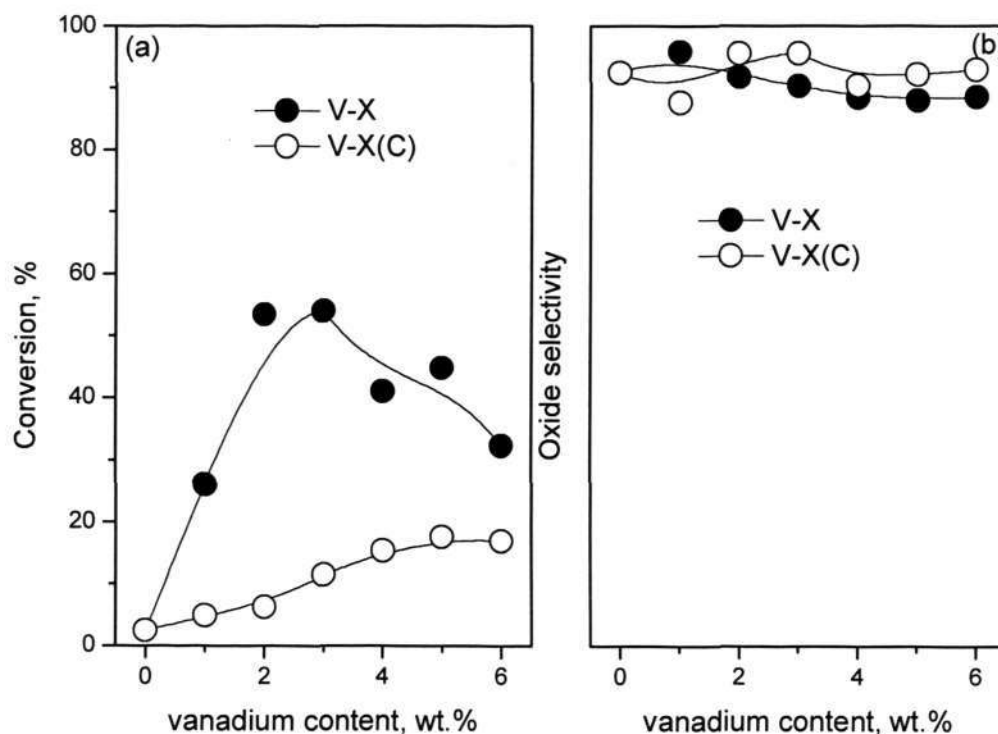
5.2.2 Catalytic Performances in *cis*-Cyclooctene Epoxidation

Figure 5.7 The influence of vanadium content on (a) *cis*-cyclooctene conversion and (b) cyclooctene oxide selectivity. The reaction condition: 338K, 24h, 1atm.

The results of *cis*-cyclooctene epoxidation over vanadium-containing zeolite with different vanadium contents are presented in Figure 5.7. Comparing with *trans*-stilbene epoxidation, the conversion of *cis*-cyclooctene is lower which is caused by the *cis*-structure and less nucleophilic substitution effect of the reactant molecules²⁵. As shown in Figure 5.7(a), the conversion increases rapidly to 54 % with vanadium content less than 3 wt.%; a higher vanadium loading results in the decrease of conversion, suggesting that only a optimized vanadium content would lead to high conversion for the *cis*-cyclooctene epoxidation reaction over the vanadium X zeolites. The 3V-X(C)

catalysts show the similar trend in conversion. The V-X catalysts exhibit higher conversion than the V-X(C) catalysts which is consistent with the results of characterization and *trans*-stilbene epoxidation. The selectivities of cyclooctene oxide over both catalysts remain constant at around 95 %.

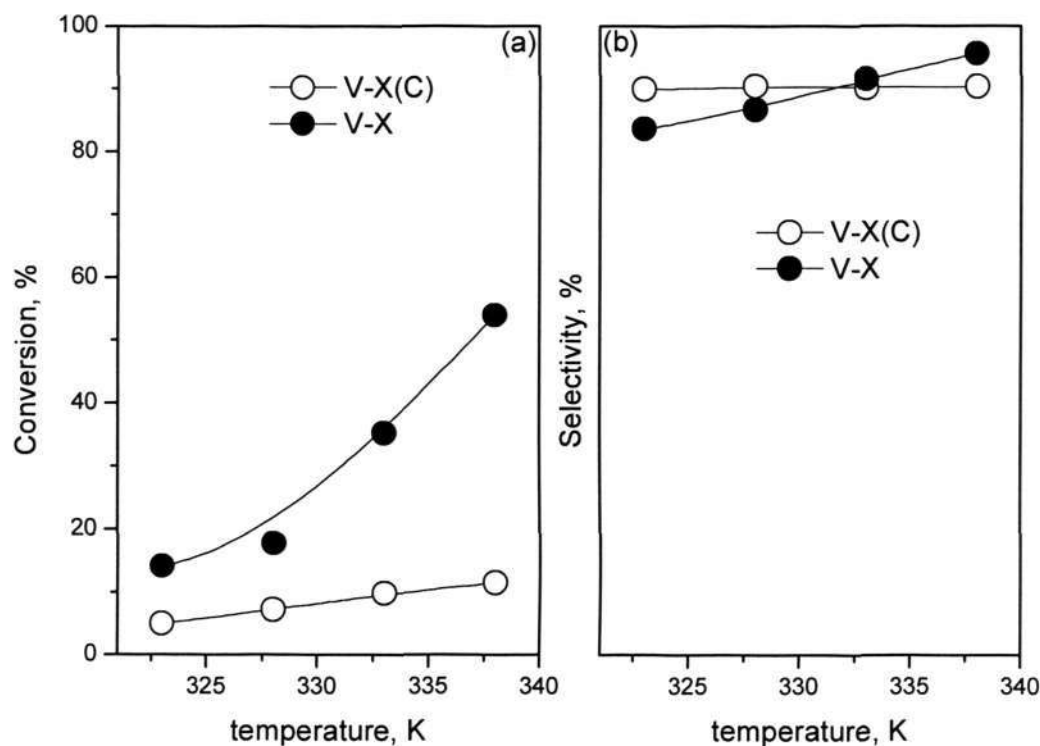


Figure 5.8 (a) *cis*-cyclooctene conversion with different temperature, (b) cyclooctene oxide selectivity with different vanadium content. The reaction condition: 24h, 1 atm, 3 wt.% vanadium.

The catalytic performances under different temperatures are carried out over these two catalysts. For V-X catalyst, the conversion rapidly increases with the temperature. The V-X(C) catalyst also shows an increase with the temperature but less significant increase rate compared to V-X catalyst. The selectivities can be maintained at around 90 %. V-X catalyst exhibits higher conversion than that of V-X(C) over all the tempera-

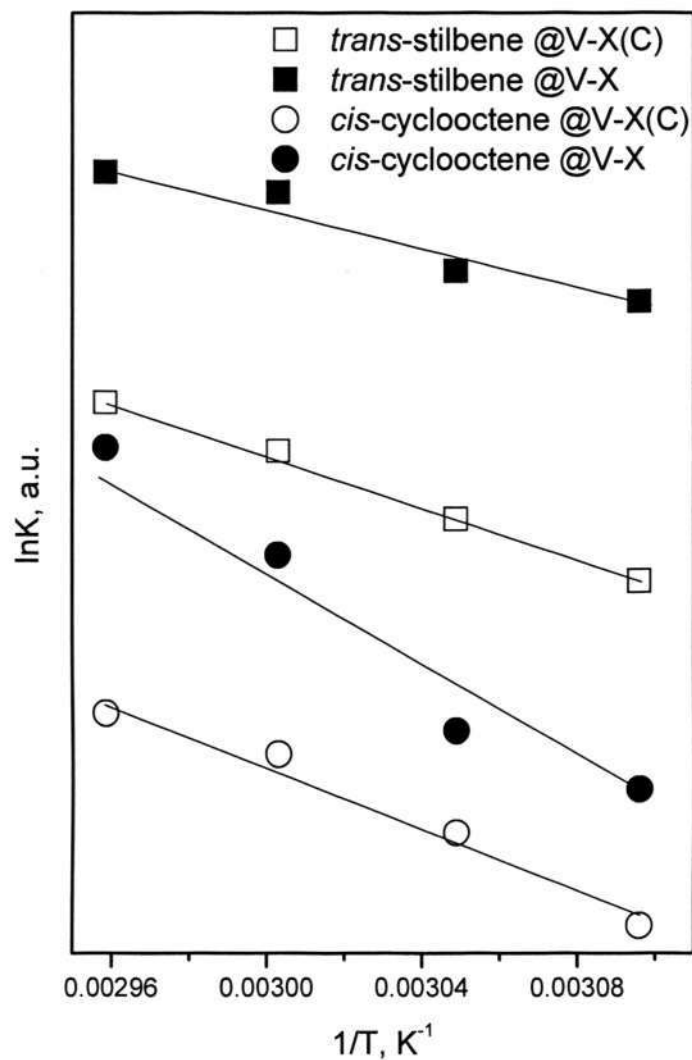


Figure 5.9. Activation energy calculated by Arrhenius plot, the activation energies for epoxidation of *trans*-stilbene are 33.37 kJ/mol and 43.15 kJ/mol on 3V-X and 3V-X(C) respectively; the activation energies for epoxidation of *cis*-cyclooctene are 85.5 kJ/mol and 51.16 kJ/mol on 3V-X and 3V-X(C) respectively. The test reaction: 1 atm, 24h.

tures. Activation energies for both two catalysts are summarized in Fig 9 as well. The activation energies of *cis*-cyclooctene epoxidation over 3V-X and 3V-X(C) are 85.5 and 51.6 kJ/mol, respectively. The higher activation energy for 3V-X could be the reason of significant increase of conversion with increasing the reaction temperature.

5.3 Conclusion

A series of vanadium-containing NaX catalysts was prepared by a facile ion exchange method. Various techniques were employed to characterize the nature of vanadium. The results indicated that most of vanadium species was in V^{5+} valance and in distorted tetrahedral coordination for both as-synthesized and calcined samples. Though the UV-Raman detected a partly polymeric VO_x species, no crystalline V_2O_5 was formed.

The vanadium species preferred locating in the supercage of the FAU zeolite during the ion-exchange; the calcination step may trigger the migration of vanadium from supercage to the SOD cage, suggested by the loss of long range structure of zeolite support. Catalytic epoxidation was carried out to test the catalytic performance of these catalysts, these vanadium supported on zeolite catalyst showed superior catalytic activity in the epoxidation of *trans*-stilbene and *cis*-cyclooctene. The as-synthesized catalysts presented remarkably better conversion and epoxide selectivity than those of calcined catalysts in both *trans*-stilbene epoxidation and *cis*-cyclooctene epoxidation. These catalytic results of these vanadium-containing catalysts strongly complimented the characterization results that the migration of vanadium active centers occurred upon the calcination pretreatment.

References:

- (1) Held, A.; Florczak, P. *Catalysis Today* **2009**, 142, 329.
- (2) Kalilur Rahiman, A.; Shanmuga Bharathi, K.; Sreedaran, S.; Rajesh, K.; Narayanan, V. *Inorganica Chimica Acta* **2009**, 362, 1810.
- (3) Dzwigaj, S.; Ivanova, E.; Kefirov, R.; Hadjiivanov, K.; Averseng, F.; Krafft, J. M.; Che, M. *Catalysis Today* **2009**, 142, 185.
- (4) Corma, A. *Chemical Reviews* **1997**, 97, 2373.
- (5) Sen, T.; Rajamohanam, P. R.; Ganapathy, S.; Sivasanker, S. *Journal of Catalysis* **1996**, 163, 354.
- (6) Dimitrova, R.; Neinska, Y.; Mihlyi, M.; Pal-Borbély, G.; Spassova, M. *Applied Catalysis A: General* **2004**, 266, 123.
- (7) Dzwigaj, S.; Matsuoka, M.; Anpo, M.; Che, M. *Microporous and Mesoporous Materials* **2006**, 93, 248.
- (8) Tang, Q. H.; Zhang, Q. H.; Wang, P.; Wang, Y.; Wan, H. L. *Chemistry of Materials* **2004**, 16, 1967.
- (9) Tielens, F.; Trejda, M.; Ziolek, M.; Dzwigaj, S. *Catalysis Today* **2008**, 139, 221.
- (10) Dzwigaj, S.; Matsuoka, M.; Anpo, M.; Che, M. *The Journal of Physical Chemistry B* **2000**, 104, 6012.
- (11) Kang, L.; Deng, W.; Han, K.; Zhang, T.; Liu, Z. *International Journal of Hydrogen Energy* **2008**, 33, 105.
- (12) Ferdov, S.; Lin, Z.; Ferreira, R. A. *Microporous and Mesoporous Materials* **2006**, 96, 363.
- (13) Hu, S.; Liu, D.; Li, L.; Borgna, A.; Yang, Y. *Catalysis Letters* **2009**, 129, 478.
- (14) Solsona, B.; Blasco, T.; Nieto, J. M. L.; Pena, M. L.; Rey, F.; Vidal-Moya, A. *Journal of Catalysis* **2001**, 203, 443.
- (15) Wu, Z.; Kim, H.-S.; Stair, P. C.; Rugmini, S.; Jackson, S. D. *The Journal of Physical Chemistry B* **2005**, 109, 2793.
- (16) *Tai Fen Zu Fan Feng Zu Ge Fen Zu*; Shen Panwen, C. Y., Luo Yuji, Gu Yidong, Xie Gaiyan, Song Yuan, Jin Songlin, Ed.; Science Press, 1998; Vol. 8.
- (17) Yang, Y. H.; Du, G. A.; Lim, S. Y.; Haller, G. L. *Journal of Catalysis* **2005**, 234, 318.
- (18) Shylesh, S.; Singh, A. R. *Journal of Catalysis* **2006**, 244, 52.

(19) Stair, P. C.; Bruce, C. G.; Helmut, K. In *Advances in Catalysis*; Academic Press: 2007; Vol. Volume 51, p 75.

(20) Tran, K.; Hanning-Lee, M. A.; Biswas, A.; Stiegman, A. E.; Scott, G. W. *Journal of the American Chemical Society* **1995**, *117*, 2618.

(21) Stair, P. C. *The Journal of Physical Chemistry A* **2009**, *113*, 4346.

(22) Wong, J.; Lytle, F. W.; Messmer, R. P.; Maylotte, D. H. *Physical Review B* **1984**, *30*, 5596.

(23) Du, G.; Lim, S.; Pinault, M.; Wang, C.; Fang, F.; Pfefferle, L.; Haller, G. L. *Journal of Catalysis* **2008**, *253*, 74.

(24) Selvaraj, M.; Seshadri, K. S.; Pandurangan, A.; Lee, T. G. *Microporous and Mesoporous Materials* **2005**, *79*, 261.

(25) Monteiro, B.; Balula, S. S.; Gago, S.; Grosso, C.; Figueiredo, S.; Lopes, A. D.; Valente, A. A.; Pillinger, M.; Lourenco, J. P.; Goncalves, I. S. *Journal of Molecular Catalysis A: Chemical* **2009**, *297*, 110.

Chapter 6 Response Surface Methodology Using Gaussian Processes: Towards

Optimizing the *trans*-Stilbene Epoxidation over Co^{2+} -NaX Catalysts

Of particular interest in this study is the catalytic oxidation process that converts *trans*-stilbene into stilbene oxide using molecular oxygen as the oxidant. Stilbene oxide is a commercially important intermediate used in the synthesis of various fine chemicals and pharmaceuticals. Conventionally, stilbene oxide is produced using organic peracid as an oxidant or by a chlorohydrin process, and a large amount of chemical waste is formed.¹ As a consequence, it is desired to exploit molecular oxygen or air as oxidant for stilbene epoxidation for the environmental, safety and economic considerations. Recently, cobalt ion-exchanged faujasite zeolite (Co^{2+} -NaX) has been reported as an efficient heterogeneous catalyst for the epoxidation of *trans*-stilbene using O_2 in the absence of co-reductant.^{2,3} These chapters focused on the synthesis of catalyst and catalytic performances, but studies on the process of the epoxidation are limited. Therefore, it is of great importance to optimize the existing catalytic oxidation process, through investigating the effect of the process factors on the overall performance (response).

Traditionally, heterogeneous catalysis research heavily relies on tedious experimental studies, screening a large number of process factors that may affect the

reaction performance. Despite the wide acceptance of RSM in various scientific disciplines, the usual “one-factor-at-a-time” approach is still common in catalysis research. That is, one factor is varied each time, with others being fixed, to investigate individual factor’s influence on process performance. This “one-factor-at-a-time” method ignores the interactions between different factors, and has long been criticized of having little chance (if any) of finding the optimal conditions.⁴⁻⁶ As Response surface methodology (RSM) is widely accepted in many scientific disciplines a consequence,⁷⁻⁹ we propose a novel GP(Gaussian process)-based RSM framework here to demonstrate/validate its application in catalytic reaction processes.

RSM is a family of statistical techniques for the design, empirical modelling and optimization of processes, where the responses of interest are influenced by several process variables (also termed *factors*).^{10,11} RSM comprises the following three major components: (i) experimental design to determine the process factors’ values based on which the experiments are conducted and data are collected; (ii) empirical modelling to approximate the relationship (i.e. the *response surface*) between responses and factors; and (iii) optimization to find the best response value based on the empirical model. In addition, the above three-stage procedure is typically operated in an iterative manner, where the information attained from previous iterations is utilized to guide the search for better response variables. RSM is particularly applicable to problems where the

understanding of the process mechanism is limited and/or is difficult to be represented by a first-principles mathematical model. RSM has seen wide applications in many scientific disciplines, including chemical,⁷ mechanical⁸ and logistics systems⁹. Depending on specific objectives in practice, these RSM techniques differ in the experimental design procedure, the choice of empirical models, and the mathematical formulation of the optimization problem.

An appropriate design of experiments (DoE) is the pre-requisite for a successful experimental study. The classical fractional factorial and central composite designs were proposed to investigate the interactions of process factors based on polynomial models.¹¹ The other class of designs is motivated by the concept of “space-filling” to have the design points being uniformly distributed within the range of each factor. Among this class the Latin hypercube sampling (LHS)¹² is probably the most widely adopted method as a result of its simple implementation and good performance. For this reason, LHS is a preferred method in practice, and it is adopted for experimental design in this study. There has been considerable effort to improve the LHS to obtain more uniform design points^{13,14} although improving the uniformity is at the expense of significantly higher computation.

After experimental data is collected according to the design points, the next step of RSM is to develop an empirical model for the response surface. The traditional method

is to fit a polynomial function (typically linear, quadratic or cubic polynomial) to the data, followed by identifying the factor values that optimize the objective function. However, the prediction accuracy of the empirical model is usually unsatisfactory when using polynomial functions, and consequently the identified optimum is unreliable. To address this issue, artificial neural network (ANN) was proposed to provide a more accurate estimation of the response surface, and it demonstrated improved optimization results in various applications.¹⁵⁻¹⁷

The primary purpose of this study is to apply Gaussian process (GP) regression as the empirical model for RSM. GP models have recently received considerable attention in process systems engineering and chemometrics.¹⁸⁻²⁰ GP can be viewed as an alternative approach to ANN because a large class of ANN-based Bayesian regression models converge to GP in the limit of an infinite network.²¹ GP models can also be derived from the perspective of non-parametric Bayesian regression,²² by directly placing Gaussian prior distribution over the space of regression functions. The fact that GP models attain both good practical performance and desirable analytical properties motivates the current work, where the polynomial function or ANN is replaced by GP for process optimization. In addition to prediction accuracy, GP models are also known for the capability of providing reliable prediction variance, which measures the uncertainty of the studied model.²³ As a consequence, the model-based optimization

problem can be formulated to account for the uncertainty, and the identified optimal process factors are remarkably more robust against the modelling uncertainty.

In a broader literature, GP regression has been applied to mechanical system optimization,⁸ and notably used as “metamodel” for the optimization of complex functions and computer models.²⁴⁻²⁸ The predictive uncertainty obtained by GP was utilized in various ways. Apley et al.²⁴ considered a “worst-case scenario” and proposed to maximize the statistical lower bound. More elegant criteria were discussed by Jones²⁵ to optimize the “probability of improvement” or “expected improvement”, and this idea was later used in^{26,27}. As the name suggests, metamodel is to approximate another complex *computer* model using a GP, whilst in the current study we are concerned with approximating and optimizing a *real* chemical process. Although the methodology for optimizing a computer model and a real process is largely similar, there is a salient distinction between them. Specifically, computer model itself is an approximation of the real process. As a result, in order to apply the optimal conditions obtained from a complex model to a real process, additional uncertainty resulting from the mismatch between the computer model and reality has to be accounted for; see²³ for a comprehensive discussion on this matter. In this paper, we restrict our scope to the development of RSM for the optimization of real chemical processes.

The rest of this chapter is organized as follows. Section 6.1 gives a brief description of the catalytic stilbene oxidation process. Section 6.2 presents the proposed RSM framework, including four major components: the LHS method for experimental design, the GP model for approximating the response surface, model-based “region-searching” (to be presented subsequently) and model-based optimization. To facilitate the adoption of the proposed methodology, the software tools to implement the RSM framework are either made freely available (if written by the authors) or identified through relevant links. Results and discussions are given in Section 6.3, followed by concluding remarks in Section 6.4.

Table 6.1: The process factors. The response variable to be maximized is the stilbene conversion (%).

Process factor	Range
Temperature, x_1 (°C)	60 – 120
Partial pressure of oxygen, x_2 (Bar)	0.2 – 0.8
Initial stilbene concentration, x_3 (mmol/15mL)	1 – 5
Stirring rate, x_4 (rpm)	200, 300, 400, 500, 700, 1000, 1250
Reaction time, x_5 (min)	30-240

6.1 Experimental

In this study, a lab-scale catalytic reaction is utilized as a test-bed to validate the proposed RSM technique. Specifically, we are interested in maximizing the *trans*-stilbene conversion rate in the epoxidation of *trans*-stilbene over Co^{2+} -NaX catalyst using molecular oxygen as the oxidant. Five process factors are considered: reaction temperature, partial pressure of oxygen, initial *trans*-stilbene concentration, stirring rate and reaction time. The range of these factors to be explored is listed in Table 6.1.

Sodium form Zeolite X (NaX) was purchased from Sigma-Aldrich. Unit cell composition of NaX was $\text{Na}_{88}\text{Al}_{88}\text{Si}_{104}\text{O}_{384}$ with unit cell dimension of 24.94 Å. The BET surface area of the zeolite was $608 \text{ m}^2\cdot\text{g}^{-1}$. Cobalt-exchanged zeolite (Co^{2+} -NaX) was prepared by ion-exchange of the NaX with 0.1 M $\text{Co}(\text{NO}_3)_2$ aqueous solution with 1:80 ratio of NaX zeolite to $\text{Co}(\text{NO}_3)_2$ followed by heating at 80 °C for 4 h. The resulting powder was filtered and washed with deionized water until it is free from unexchanged cobalt ions. The washed Co^{2+} -NaX sample was dried at 100 °C for 4 h.

The liquid phase catalytic *trans*-stilbene epoxidation reactions were carried out using a batch-type reactor operated under atmospheric pressure. In a typical reaction, a measured amount of *trans*-stilbene (> 96%, Aldrich), 200 mg of Co^{2+} -X catalyst, and 15 ml of N,N-dimethylformamide (DMF, > 99.8%, J.T.Baker) were introduced into a 50 ml round-bottomed flask followed by bubbling O_2 or O_2 diluted with N_2 into the liquid

at a flow rate of $50\text{ml}\cdot\text{min}^{-1}$. The reaction was initiated by immersing the round bottom flask into an oil bath under desired reaction temperature. The solid catalyst was filtered off after reaction, and the liquid organic products were analyzed by an Agilent gas chromatograph (GC) 6890 equipped with a HP-5 capillary column (30 m long and 0.32 mm in diameter, packed with silica-based supel cosil). Calibration of GC was done using solutions with known amounts of benzaldehyde, benzoic acid, stilbene, and stilbene oxide in DMF. The conversion was calculated on the basis of moles of stilbene as follows:

$$\text{Conversion (\%)} = \frac{(\text{initial moles}) - (\text{final moles})}{(\text{initial moles})} \times 100\% \quad (6.1)$$

6.2 Response Surface Methodology using Gaussian Processes

The proposed RSM framework is operated in an iterative manner and is summarized step by step as follows.

Step 1: Use LHS to obtain design points that are uniformly distributed over the whole factor space.

Step 2: Conduct experiments at the design points, and collect the response data.

Step 3: Develop GP regression model to approximate the response surface.

Step 4: If this is NOT the final iteration

Then:

- (a) Find the region of factors that is predicted (using the GP model) to give better response variable.
- (b) Use LHS to allocate design points that are uniformly distributed over this region, and go to Step 2 for the next iteration.

Else:

- (c) Solve the mathematical optimization problem based on the GP model to obtain the optimal values of the process factors.
- (d) Conduct final experiment(s) to verify the optimal conditions.

In the initial iteration, little knowledge is available regarding the factors' values for desirable response variables, and thus LHS will be used to uniformly fill the entire factor space with designed points (Step 1). At Step 2, actual experiments will be conducted carefully at the design points to obtain the corresponding response variables, followed by Step 3 to develop a GP model to approximate the relationship between the response and process factors. In Step 4, if this is not the final iteration, a model-based approach is used to identify the region of factors that is more likely to produce better

responses (Step 4(a)), followed by using LHS to generate design points within this region for experiments in next iteration(Step 4(b)). Step4 (a)(b) is referred to as “region-searching” in this paper. After several iterations of this procedure, the factor space has been well explored and no more iterations are needed. In this case, Step 4 is to use a model-based optimization approach to obtain the optimal values of the process factors (Step 4(c)), followed by the final experiment to validate the optimal conditions (Step 4(d)).

Conceptually, this iterative procedure is similar to the traditional catalyst screening practice. However, the conventional methods search for region-of-interest purely based on experimental data and intuition. In contrast, the proposed strategy takes advantage of a GP model to predict a better region of factor’s values. Therefore, RSM is a rational, as opposed to trial-and-error, approach to process optimization. We discuss each individual step within an iteration in more detail below.

6.2.1. Experimental Design through Latin Hypercube Sampling

The key objective of DoE is to select the values of process factors in such a way that the obtained experimental data are representative of the design space being explored and informative to predict the process responses. This section presents a specific DoE method, Latin hypercube sampling (LHS),¹² and its incremental algorithm.

LHS is a special “space-filling” DoE method that selects the factors’ values to be uniformly distributed. It was shown that LHS is more efficient than randomly generating the uniform samples from the design space. For the same number of design points, the modelling and estimation accuracy of LHS is substantially better than those of random sampling.¹² Specifically, let $R_k (k = 1, \dots, K)$ be the range of values of factor k and N be the number of design points to be generated. The first step of LHS is to divide the range of each factor k , R_k , into N equally spaced intervals, followed by uniformly sampling from each interval to result in N values for this factor: $x_{kj}, j = 1, \dots, N$. Subsequently, these N values are randomly permuted to have a better coverage of the design space. This procedure is repeated for all the K process factors to attain $K \times N$ values: $x_{kj}, k = 1, \dots, K, j = 1, \dots, N$, which form the N design points, each being K dimensional. More details of LHS can be found in ¹². The LHS algorithm has seen applications in various disciplines, partly due to its relatively simple implementation and its wide availability in statistical software packages (e.g. Statistical Toolbox for Matlab).

The capability to incrementally increase the design points is clearly a desired property of LHS and other DoE methods, since RSM is often conducted iteratively. A straightforward approach is to apply the LHS algorithm multiple times to add more design points without any consideration of previous data. However, although LHS

guarantees that each set of points are located in the equally spaced N intervals at each dimension, the entire data set does not necessarily cover the design space uniformly. We illustrate this phenomenon in Figure 6.1 in which a single process factor is considered. Initially, two design points are generated and located in two equally spaced intervals (Figure 6.1(a)), followed by adding two more design points. If these two new data are generated by repeating LHS algorithm, it only guarantees that the new points are separately located in the original two intervals; however, they can be close to the original data and thus undesirable (Figure 6.1(b)(c)). To address this issue, we adopt a simple but efficient incremental approach for LHS.²⁹ Suppose N_1 design points were previously generated by LHS and N_2 additional points are required, the incremental algorithm divides the range of each factor into (N_1+N_2) equal intervals. Clearly, at least N_2 of the intervals do not contain any previous data. It is possible that there are more than N_2 empty intervals due to more than one data point falling into the same interval. Therefore, we randomly select N_2 empty intervals and generate a random sample from each of them. The above procedure is repeated for each factor to attain N_2 new design points. Note that the incremental algorithm does not guarantee that all (N_1+N_2) design points are allocated into (N_1+N_2) equally spaced intervals because some intervals may not be occupied if there are more than N_2 empty intervals. Nevertheless, this algorithm is a fast and efficient way to obtain significantly better coverage of the design space

than repeated LHS. A Matlab implementation of the incremental LHS algorithm is available from: <http://www.ntu.edu.sg/home/chentao/>.

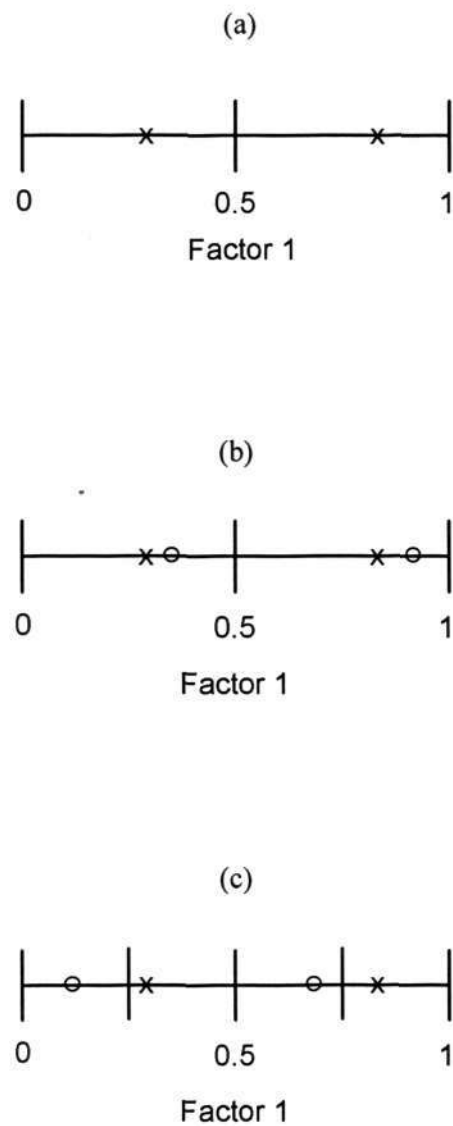


Figure 6.1 Illustration of incremental LHS using one design factor within the range of [0 1]. (a) Initial two design points (denoted by “x”) generated by LHS. (b) Two additional design points (denoted by “o”) generated by one more run of LHS; they are

close to the initial points and do not provide desired overall coverage of the range. (c)

Two additional design points generated by incremental LHS.

6.2.2. Gaussian Process Regression Modelling

The idea of Gaussian process (GP) can be dated back to the classical statistical method by O'Hagan.³⁰ However, the application of GP as a regression (and classification) technique was not common until late 1990's, when the rapid development of computational power facilitated the implementation of GP for large data sets. Recently, GP models have seen successful applications in various fields, including chemical process modeling,^{19,31} chemometric calibration of spectrometers,^{18,20} and mechanical system modelling and optimization.⁸ In this subsection, a brief overview of GP regression technique is given, including the formulation and implementation of the model.

From the perspective of a regression problem, a functional relationship is identified between the K dimensional predictor variables (factors), \mathbf{x} , and the response y . Consider a training data set of size N : $\{\mathbf{x}_i, y_i; i = 1, \dots, N\}$ that was obtained by conducting experiments on the designed points. A GP regression model is defined such that the regression function $y(\mathbf{x})$ has a Gaussian prior distribution with zero mean, or in discrete form:

$$\mathbf{y} = (y_1, \dots, y_N)^T \sim G(0, \mathbf{C}) \quad (6.2)$$

where \mathbf{C} is an $N \times N$ covariance matrix of which the ij -th element is defined by a covariance function: $C_{ij} = C(\mathbf{x}_i, \mathbf{x}_j)$. An example of such a covariance function is:

$$C(\mathbf{x}_i, \mathbf{x}_j) = a_0 + a_1 \sum_{k=1}^K x_{ik} x_{jk} + v_0 \exp\left(-\sum_{k=1}^K w_k (x_{ik} - x_{jk})^2\right) + \sigma^2 \delta_{ij} \quad (6.3)$$

where x_k is the k -th variable of \mathbf{x} , and $\delta_{ij} = 1$ if $i=j$, otherwise $\delta_{ij} = 0$. We term

$\theta = (a_0, a_1, v_0, w_1, \dots, w_K, \sigma^2)^T$ “hyper-parameters” defining the covariance function. The

hyper-parameters must be non-negative to ensure that the covariance matrix is non-

negative definite. For the covariance function given in Equation (6.3), the first two

terms represent a constant bias (offset) and a linear correlation term, respectively. The

exponential term is similar to the form of a radial basis function, and it takes into

account the potentially strong correlation between the responses with similar predictors.

The term σ^2 captures the random error effect. By combining both linear and non-linear

terms in the covariance function, GP is capable of handling both linear and non-linear

data structures.¹⁸ Other forms of covariance functions are also discussed.²²

For a new datapoint with predictor vector \mathbf{x}^* , the predictive distribution of the output y^* conditional on the training data is also Gaussian, of which the mean (\hat{y}) and variance (σ_y^2) are calculated as follows:

$$\hat{\mathbf{y}}^* = \mathbf{k}^T(\mathbf{x}^*)\mathbf{C}^{-1}\mathbf{y} \quad (6.4)$$

$$\sigma_{\hat{\mathbf{y}}^*}^2 = C(\mathbf{x}^*, \mathbf{x}^*) - \mathbf{k}^T(\mathbf{x}^*)\mathbf{C}^{-1}\mathbf{k}(\mathbf{x}^*) \quad (6.5)$$

where $\mathbf{k}(\mathbf{x}^*) = [C(\mathbf{x}^*, \mathbf{x}_1), \dots, C(\mathbf{x}^*, \mathbf{x}_N)]^T$.

The hyper-parameters θ can be estimated by maximizing the following log-likelihood function:

$$L = \log p(\mathbf{y} | \theta, \mathbf{X}) = -\frac{1}{2} \log |\mathbf{C}| - \frac{1}{2} \mathbf{y}^T \mathbf{C}^{-1} \mathbf{y} - \frac{N}{2} \log(2\pi) \quad (6.6)$$

This is a non-linear optimization problem which can be solved by using gradient based methods, e.g. the conjugate gradient method.²² These methods require to calculate the derivative of log-likelihood with respect to each hyper-parameter θ , which is:

$$\frac{\partial L}{\partial \theta} = -\frac{1}{2} \text{tr} \left(\mathbf{C}^{-1} \frac{\partial \mathbf{C}}{\partial \theta} \right) + \frac{1}{2} \mathbf{y}^T \mathbf{C}^{-1} \frac{\partial \mathbf{C}}{\partial \theta} \mathbf{C}^{-1} \mathbf{y} \quad (6.7)$$

where $\partial \mathbf{C} / \partial \theta$ can be obtained from the covariance function. A Matlab implementation of the GP models is used to produce the results in this chapter and it is publicly available from <http://www.gaussianprocess.org/gpml/code/matlab/doc/>.

It should also be noted that the calculation of the likelihood and the derivatives involves a matrix inversion step and takes time of the order $O(N^3)$, which can be extremely demanding for large data set. Fortunately in the context of RSM, the experiments are

costly to run, and the available data are normally limited and should not pose a computational problem for GP modelling. In addition, for large data sets, sparse training strategies may be employed to significantly reduce the computational cost.³²

6.2.3. Model-based Region-searching

The GP model that relates the process response y to the factors x provides the basis to guide the search for more promising process factors, referred to as “region-searching” in this study. Once a better region of factors is identified, the LHS method will allocate new design points to this region for next-iteration experiments. In this stage, model robustness emerges as an issue because of the predictive errors (and thus uncertainty) that are inevitable when using a statistical regression model. The predictive uncertainty must be considered and accounted for in order to identify a trustworthy optimal region. Fortunately, GP models are capable of giving the uncertainty (through variance) of the prediction in addition to a mean predicted value, and the uncertainty should be incorporated into the region-searching method.

In this paper the worst-case scenario is considered to deal with the prediction uncertainty. Suppose the objective is to maximize the response variable, we instead maximize the *lower-bound* of the response predicted by the GP model. Similar approach was adopted in ²⁴ for the optimization of computer simulation of mechanical systems. Mathematically we seek to obtain the region of process factors defined by:

$$\{\mathbf{x} : \hat{y}(\mathbf{x}) - 1.96\sigma_y(\mathbf{x}) > c \text{ AND } \sigma_y(\mathbf{x}) > b \text{ AND } \mathbf{x} \in S\} \quad (6.8)$$

where $\hat{y}(\mathbf{x})$ and $\sigma_y(\mathbf{x})$ are the predictive mean and standard deviation obtained from GP model (Equations (6.4)(6.5)), respectively, and S denotes the range of the process factors as given in Table 6.1. Since the prediction from GP is Gaussian distributed, $\hat{y}(\mathbf{x}) - 1.96\sigma_y(\mathbf{x})$ corresponds to the 95% lower-bound of the prediction, and c is a user-chosen value. Essentially, this is to search for the factors such that the 95% lower-bound of the response is greater than c . Furthermore, the constraint $\sigma_y(\mathbf{x}) > b$ is to avoid allocating design points to well-explored region, where the GP model is quite certain about its prediction (i.e. with small $\sigma_y(\mathbf{x})$) and thus further experiments in this region are not necessary. The choice of b and c is dependent on specific applications, and this will be discussed in the next section.

It should be noted that the proposed method may not explore the region with high variance and low prediction (i.e. predictive lower bound less than c). With more design points in this region, it is possible that the prediction becomes higher. As a result, our approach does not guarantee to find the *global optimum* of the process. However, since we use LHS to allocate multiple initial design points to cover the whole design range, the possibility of obtaining a poor local optimum is fairly low, and our method appears to give satisfactory results as demonstrated in the application study (Section 6.4). One possible way to address this issue is to also search for $\{\mathbf{x} : \sigma_y(\mathbf{x}) > d \text{ AND } \mathbf{x} \in S\}$ in

addition to Equation (6.8), where d can be set to a relatively large value to explore high variance region. A more disciplined approach is to adopt the concept of expected improvement.²⁵⁻²⁷ Currently, the effectiveness of these and other methods are under further investigation.

Clearly there are infinite number of design points that satisfy Equation (6.8). Hence the region-searching essentially becomes a constrained DoE problem, where the factors' values are selected to be uniformly distributed in the constrained space that is defined by Equation (6.8). This constrained DoE problem can be solved as follows. Suppose from previous iterations, N design points were used and the experiments were conducted, and now N_1 new design points are to be generated. Then we can generate N_1 design points using incremental LHS algorithm (discussed in section 6.2.1), and find the points such that Equation (6.8) holds. Suppose n out of N_1 points satisfy this constraint, and thus we can further generate $N_1 - n$ design points using incremental LHS. This procedure is repeated until a total of N_1 design points satisfy the above constraint, and these points are selected for the experiments in next iteration. The proposed procedure is an effective solution to the constrained DoE problem, since the incremental LHS algorithm ensures a uniform distribution of the design points within the entire factors' range ($\mathbf{x} \in S$), and thus the points selected will also be uniformly distributed within the region given by Equation (6.8).

6.2.4. Model-based Optimization

Once the factors' space is well explored through several iterations of the RSM technique, the final step is to conduct the optimization of the response variable. Similar to region-searching step, the optimization problem is formulated to maximize the 95% lower bound of predicted response variable, subject to the constraint on the factors' range ($\mathbf{x} \in S$):

$$\max_{\mathbf{x}} (\hat{y}(\mathbf{x}) - 1.96\sigma_y(\mathbf{x})) \quad \text{s.t. } \mathbf{x} \in S \quad (6.9)$$

This is typically a mixed-integer optimization problem, i.e. continuous process factors (e.g. reaction temperature) are coupled with categorical and discrete (or integer) factors. For example in the reactor available in our laboratory, the stirring rate is fixed to seven different values (200, 300, 400, 500, 700, 1000 and 1250 rpm, see Table 6.1) due to instrument constraint, and thus the stirring rate can only take a discrete set of values. It is well known that mixed-integer problems are dramatically more difficult to solve than continuous problems, and the computation time increases rapidly with the number of discrete factors.³³ To solve this optimization problem, an in-house branch-and-bound algorithm was developed under Matlab computational environment. A comprehensive optimization toolbox for Matlab (i.e. TOMLAB: <http://tomopt.com/tomlab/>) is commercially available and could also be used for solving this problem.

6.3 Results and Discussions

Table 6.2: Designed experiments and resultant stilbene conversion y (%): the first iteration.

Run No.	x_1	x_2	x_3	x_4	x_5	y
1	73	0.62	3.25	1250	162	1.42
2	107	0.41	4.95	1000	182	18.95
3	110	0.65	1.95	700	76	13.31
4	118	0.79	1.25	300	112	42.78
5	88	0.76	2.95	500	152	6.72
6	68	0.33	4.50	400	238	1.52
7	71	0.37	2.65	200	198	1.75
8	91	0.21	4.25	1250	228	9.50
9	104	0.57	1.65	300	126	20.13
10	76	0.28	3.50	500	138	1.99
11	84	0.47	1.95	400	200	9.54
12	98	0.71	2.25	700	40	4.00
13	115	0.55	1.45	200	214	55.00
14	102	0.35	2.80	1000	42	4.00

15	93	0.49	3.30	200	178	9.49
16	81	0.72	3.90	700	64	1.08
17	113	0.30	1.15	1250	50	12.02
18	78	0.54	4.65	400	146	1.88
19	63	0.67	2.50	500	90	0.01
20	96	0.25	3.80	300	98	5.63

This section demonstrates the application of the proposed RSM framework for the optimization of stilbene conversion of a catalytic oxidation process. In the initial iteration, the knowledge about the process is relatively limited, and the LHS algorithm is used to obtain 20 design points within the whole range of five factors for experiments. The designs and corresponding stilbene conversion rates are given in Table 6.2.

Following the reaction experiments, the response surface is approximated by a GP model. However, before the model is applied for subsequent region-searching or optimization purpose, its predictive capability should be validated. In this study, we adopt the method of leave-one-out cross-validation (LOOCV)³⁴ to validate the GP regression model. LOOCV takes a single data point from the entire data set as the validation data, and then develop a GP model using the remaining data points. Hence the error of the validation data can be calculated. This procedure is repeated such that

each data point is used once for validation, and the overall validation error (typically in terms of root mean squared error (RMSE) or coefficient of determination (R^2)) is used as the criterion to assess model quality. In addition, to consider the effect of prediction uncertainty, we also use the average *negative log predictive density* (NLPD)^{3 5} defined by

$$\text{NLPD} = -\frac{1}{N} \sum_{i=1}^N \log p(\hat{y}(\mathbf{x}_i) = y_i | \mathbf{x}_i) \quad (6.10)$$

to assess the prediction performance. When prediction is Gaussian distributed with mean $\hat{y}(\mathbf{x}_i)$ and variance $\sigma_y^2(\mathbf{x}_i)$, $p(\hat{y}(\mathbf{x}_i) = y_i | \mathbf{x}_i)$ corresponds to the calculation of a normal density function with mean $\hat{y}(\mathbf{x}_i) - y_i$ and variance $\sigma_y^2(\mathbf{x}_i)$. NLPD reaches its minimum if all predictions are equal to the true value and the predictive variances are zero. It was shown³⁵ that given a prediction, the optimal variance is the squared error of the prediction mean. Therefore, NLPD penalizes both over-confident (small variance) and under-confident (large variance) predictions, and it is a reliable criterion to quantify the prediction quality under uncertainty. For the purpose of comparison, the conventional multiple quadratic polynomial regression model is also developed. Figure 6.2 gives the prediction results of LOOCV for both GP and quadratic regression model. Clearly, the GP model (RMSE=5.42, R^2 =0.85, NLPD=6.07) has attained significantly higher prediction accuracy than the quadratic regression (RMSE=7.66, R^2 =0.70,

NLPD=8.52). A final GP model is then developed from all the available data, and this model will be used for either region-searching or optimization subsequently.

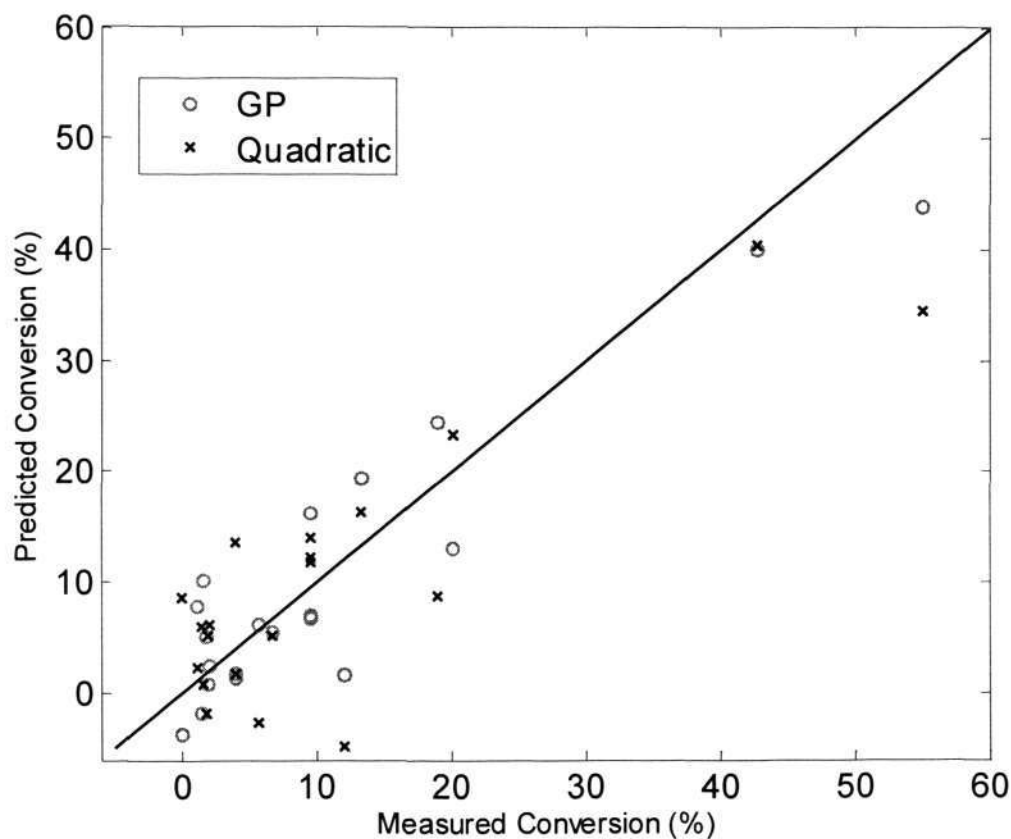


Figure 6.2 Prediction results (the first iteration) using leave-one-out cross-validation for GP (RMSE=5.42, $R^2=0.85$, NLPD=6.07) and quadratic regression (RMSE=7.66, $R^2=0.70$, NLPD=8.52) models.

Table 6.2 and Figure 6.2a also indicate that most experiments did not result in satisfactory conversion rate of stilbene. Indeed, only four experiments attained conversion rates higher than 15%. Therefore, it may be premature to claim that the optimal region has been well identified for process optimization. However, these

experiments do provide important information as to which region of the factors' space is more promising to improve the conversion rate. Following the region-searching algorithm presented in section 6.2.3, we search for a new set of design points \mathbf{x} such that the 95% lower-bound prediction from the GP model is sufficiently large (i.e. $\hat{y}(\mathbf{x}) - 1.96\sigma_y(\mathbf{x}) > c$) and the prediction uncertainty is also large ($\sigma_y(\mathbf{x}) > b$). The choice of b and c is subject to the experimenter's discretion. Based on the experimental results obtained in iteration 1, it may be reasonable to set $c=15\%$, in the hope to explore the factors' region with conversion higher than 15%. In addition, we set b to be the average standard deviation of predictions in the LOOCV procedure, so that to generate design points that are not well predicted by the current model. Based on these choices, the incremental LHS algorithm generates a new set of 20 design points as shown in Table 6.3, which also lists the conversion rates obtained through reaction experiments.

Table 6.3 Designed experiments and resultant stilbene conversion y (%): the second iteration.

Run No.	x_1	x_2	x_3	x_4	x_5	y
21	112	0.73	1.83	200	174	38.07
22	119	0.40	4.17	300	158	18.47
23	116	0.22	2.12	1000	139	27.75
24	118	0.42	1.09	1250	147	59.28

25	119	0.48	4.10	200	221	28.99
26	120	0.21	1.01	500	133	31.90
27	106	0.54	2.18	700	236	42.40
28	113	0.80	3.42	500	203	28.10
29	115	0.63	3.93	200	185	23.18
30	112	0.61	1.54	1250	136	44.45
31	119	0.65	1.73	300	180	61.05
32	113	0.60	2.26	1250	129	30.29
33	116	0.70	2.47	700	200	56.53
34	110	0.69	4.28	400	161	15.79
35	117	0.20	4.98	200	219	7.52
36	104	0.45	1.42	1250	166	35.97
37	109	0.28	4.54	400	202	12.29
38	109	0.48	1.67	1000	239	59.04
39	120	0.57	2.87	300	223	51.47
40	119	0.31	1.19	700	79	22.64

A comparison between Table 6.2 and 6.3 confirms that the RSM framework has successfully identified more promising region of the process factors. On average, the

conversion rate of the 20 experiments in Table 6.3 is 34.76%, which is a dramatic improvement over the average conversion of 11.04% in Table 6.2. The maximal conversion achieved in Table 6.3 is 61.05%, as opposed to 55.00% in Table 6.2. In addition, recall that the objective of the region-searching in iteration 1 is to find the process factors with conversion higher than 15%. This objective has been fulfilled for most experiments in Table 6.3, except the 15th and 17th runs (conversion rate of 7.52% and 12.29% respectively). Therefore, it appears that the GP model is reasonably reliable for predicting the process response variable.

In principle, the RSM can be iterated multiple times as required, and the number of iterations should be decided by the experienced experimenters after careful examination of the results. The primary purpose of the present study is to demonstrate and validate the proposed RSM framework, and thus the number of iterations is restricted to two. Indeed, the specialists in catalytic reactions also feel that the identified factors in Table 6.3 may be close to the optimal condition achievable given the current experimental environment.

To enable the optimization in the final iteration, a new GP regression model is required to approximate the response surface, using all the 40 data available in Table 6.2 and 6.3. Again, the LOOCV approach is employed to assess the prediction capability of GP and conventional quadratic regression models, and the prediction

results are shown in Figure 6.3. With more data available in iteration 2, the prediction accuracy of both GP and quadratic models has been improved in comparison with iteration 1. Adding more data typically has significant effect on reducing the prediction error in RSM, since initially the data are very limited. However, due to the time and cost associated with experiments, it may be unrealistic to request a large amount of experimental data to be collected in the process design and development stage. Therefore, advanced modelling approaches should be utilized if they can provide more accurate predictions than conventional methods on the same amount of data. Figure 6.3 indicates that, again, the GP model ($RMSE=3.77$, $R^2=0.96$) is superior to the quadratic regression ($RMSE=5.31$, $R^2=0.92$) in terms of lower RMSE and higher R^2 value.

Based on the finally developed GP model from all the 40 experimental data, the optimization problem defined in Equation (6.9) is solved using branch-and-bound algorithm. The optimal process condition is found to be: $x_1=120$ °C (temperature), $x_2=0.63$ bar (partial pressure of oxygen), $x_3=1.00$ mmol/15mL (initial stilbene concentration), $x_4=1250$ rpm (stirring rate), and $x_5=120$ min (reaction time), and the GP model predicts the conversion rate to be 94.51%. The actual experiment at this claimed optimal condition attains a conversion rate of 93.45%, which is reasonably close to the predicted value and is

regarded as satisfactory under the current constraints of experiments.

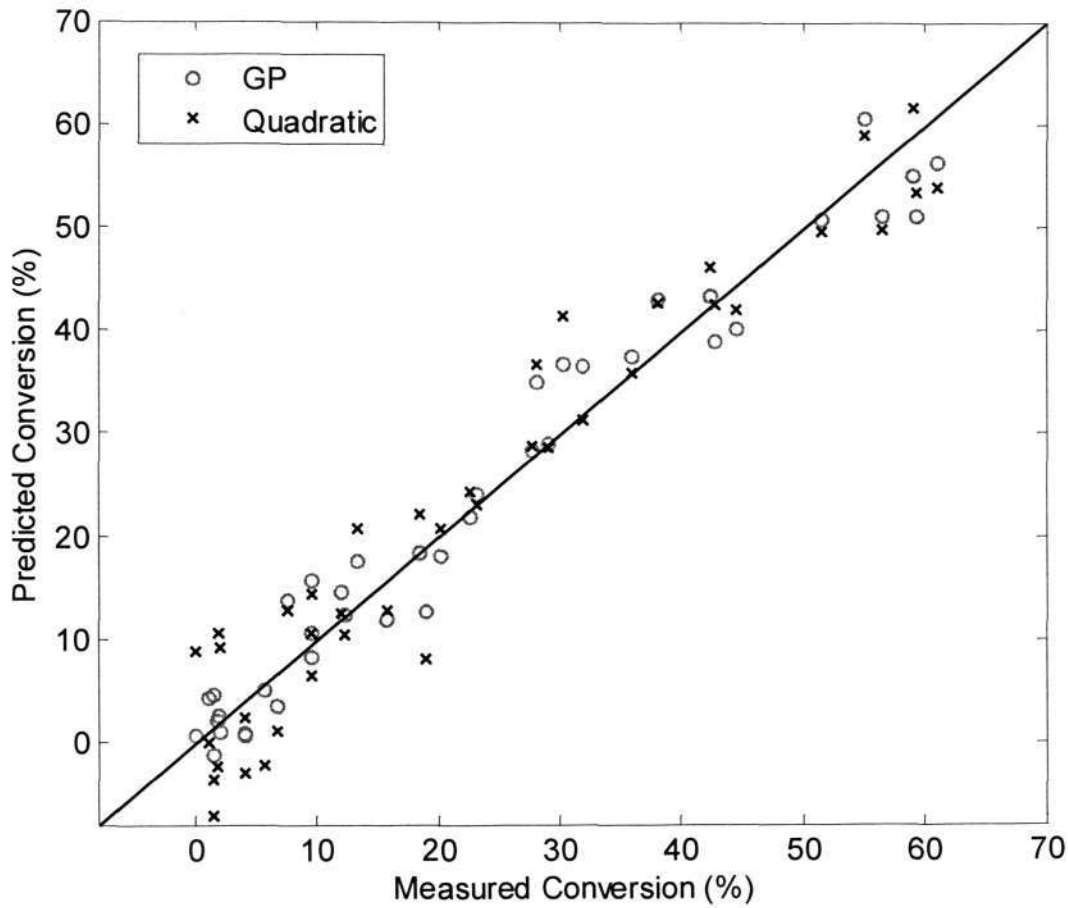


Figure 6.3 Prediction results (the second iteration) using leave-one-out cross-validation for GP (RMSE=3.77, $R^2=0.96$, NLPD=3.06) and quadratic regression (RMSE=5.31, $R^2=0.92$, NLPD=3.60) models.

Besides searching for the optimal process conditions, one important task of RSM is to understand how the process factors influence the response variable, which can be visualized by the response surface plots as given in Figure 6.4. In each plot we illustrate the conversion rate against two process factors, and thus a total of 10 plots would be

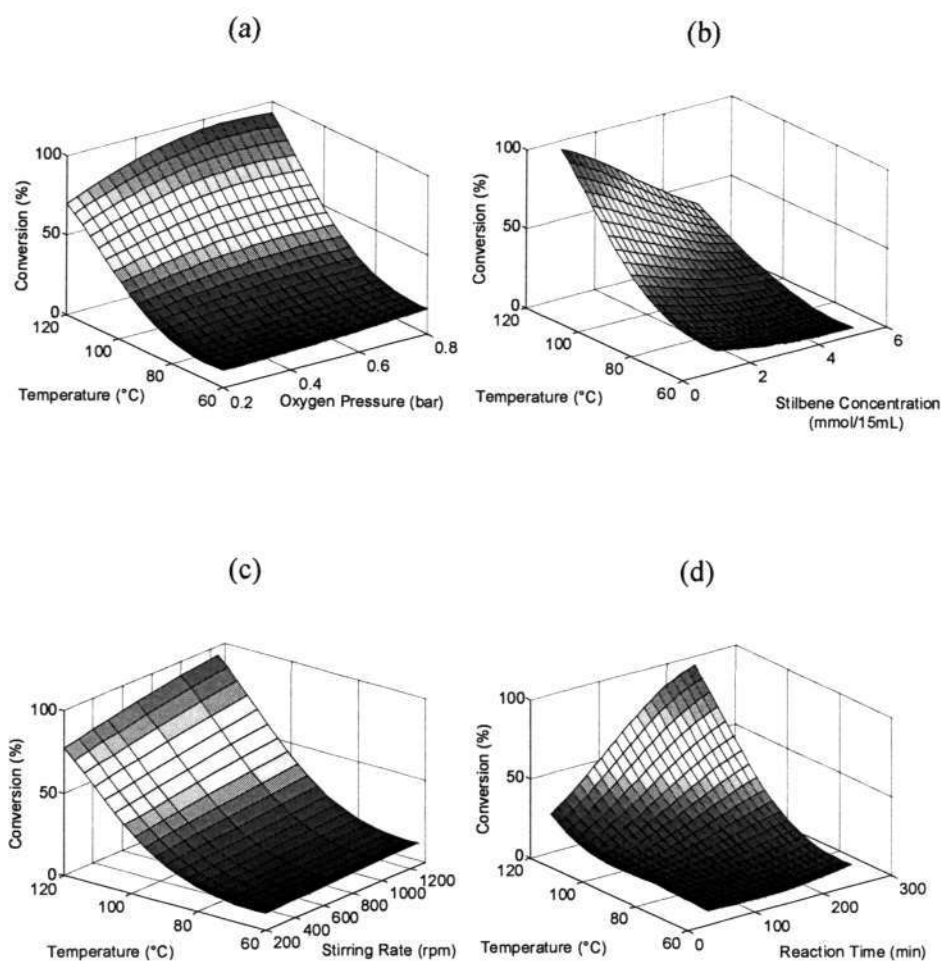


Figure 6.4 The response surface of conversion as a function of temperature and (a) oxygen pressure, (b) stilbene concentration, (c) stirring rate, and (d) reaction time.

needed to present the combinations of every two factors. For demonstration purpose, Figure 6.4 only includes four plots to consider the effect of temperature and other four factors. The response surfaces were obtained by calculating the response of the final GP

model through varying the two factors within their range, whilst keeping other three factors to have the optimal values as given in the previous paragraph.

Figure 6.4 clearly indicates the trend of the stilbene conversion as a function of process factors. Within the range under study, it appears that higher temperature, faster stirring rate and longer reaction time lead to better conversion, which is consistent with our chemical intuition. Indeed, the identified optimal condition for these three factors corresponds to their maximum value within the range (refer to Table 6.1 for the factors' range). In contrast, lower initial stilbene concentration results in better conversion rate, since a smaller amount of stilbene needs to be converted and thus the optimal condition for this factor is at its minimum value of 1.00 mmol/15mL. Finally, Figure 6.4(a) shows that the conversion rate increases when oxygen pressure increases from 0.20 bar to approximately 0.63 bar, and then decreases with further increase in the pressure. The identified optimal oxygen pressure is 0.63 bar.

6.4 Conclusions

This chapter has proposed an iterative RSM framework for the modelling and optimization of a chemical reaction process. The key component of this proposed framework is a novel statistical approach, i.e. GP regression, which is used as the empirical model for RSM. Compared with traditional regression methods, GP models have been demonstrated to attain the capability of providing high prediction accuracy

and reliable prediction uncertainty. The desirable properties of GP model are the basis for model-based range-searching and optimization in the iterative framework. The proposed methodology has been successfully applied to the optimization of *trans*-stilbene epoxidation over Co^{2+} -X catalysts.

In principle, the presented RSM framework is applicable to general “processes” in diverse fields of science, engineering, management, among others, where empirical models are developed from designed experiments to facilitate the rational, instead of “trial-and-error”, design and optimization of the processes. Currently, we are investigating the extension of the methodology to consider multiple objectives that are to be optimized.

References:

- (1) Wedissermel, K.; Arpe, H. J. *Industrial Organic Chemistry*; 4th ed.; Wiley-VCH: Weinheim, 2003.
- (2) Tang, Q.; Zhang, Q.; Wu, H.; Wang, Y. *Journal of Catalysis* **2005**, 230, 14.
- (3) Sebastian, J.; Jinka, K. M.; Jasra, R. V. *Journal of Catalysis* **2006**, 244, 11.
- (4) Tang, Q. H.; Chen, Y. T.; Zhou, C.; Chen, T.; Yang, Y. H. *Catalysis Letters* **2009**, 128, 210.
- (5) Baumes, L.; Farrusseng, D.; Lengliz, M.; Mirodatos, C. *QSAR & Combinatorial Science* **2004**, 23, 767.

- (6) Yang, Y. H.; Lim, S. Y.; Wang, C. A.; Du, G. A.; Haller, G. L. *Microporous and Mesoporous Materials* **2004**, 74,133 .
- (7) Fezei, R.; Hammi, H.; M'Nif, A. *Journal of Chemometrics* **2008**, 22, 122.
- (8) Yuan, J.; Wang, K.; Yu, T.; Fang, M. **2008**, 48, 60.
- (9) Shang, J. S.; Li, S.; Tadikamalia, P. *International Journal of Production Research* **2004**, 42, 3823-3849.
- (10) Box, G. E. P.; Draper, N. R. *Empirical Model Building and Response Surfaces*; Wiley, 1987.
- (11) Myers, R. H.; Montgomery, D. C. *Response Surface Methodology*; Wiley, 1995.
- (12) McKay, M. D.; Beckman, R. J.; Conover, W. J. *Technometrics* **1979**, 21, 17.
- (13) Fang, K.-T.; Winker, P.; Lin, D. K. J.; Zhang, Y. *Technometrics* **2000**, 42, 12.
- (14) Ma, C. X.; Fang, K. T. *International Journal of Materials & Product Technology* **2004**, 20, 115.
- (15) Agatonovic-Kustrin, S.; Zecevic, M.; Zivanovic, L.; Tucker, I. G. *Analytica Chimica Acta* **1998**,364 , 11.
- (16) Dutta, J. R.; Dutta, P. K.; Banerjee, R. *Proess Biochemistry* **2004**, 39, 6.
- (17) Shao, P.; Jiang, S. T.; Ying, Y. J. *Trans IchemE, Part C, Food and Bioproducts Processing* **2007**, 85, 8.
- (18) Chen, T.; Morris, J.; Martin, E. *Chemometrics and intelligent laboratory systems* **2007**, 87, 13.
- (19) Likar, B.; Kocijan, J. *Computers & Chemical Engineering* **2007**, 31, 142-152.
- (20) Hernandez, N.; Talavera, I.; Dago, A.; Biscay, R. J.; Ferreira, M. M. C.; Porro, D. *Journal of Chemometrics* **2008**, 22, 686-694.

- (21) Neal, R. M. *Bayesian learning for neural networks*; Springer-Verlag New York, 1996.
- (22) Rasmussen, C. E.; Williams, C. K. I. *Gaussian Processes for Machine Learning*; MIT Press, 2006.
- (23) O'Hagan, A. *Reliability engineering & System Safety* **2006**, 91, 11.
- (24) Apley, D.W.; Liu, J.; *J. Mech. Des.* **2006**, 128, 945.
- (25) Jones, D.R.; *Global, Optim.* **2001**, 21, 345
- (26) Frean, M.; Boyle, P.; *Using Gaussian processes to optimize expensive functions*, in: Wobcke, W.; Zhang, M. (Eds) *AI 2008: Advances in Artificial Intelligence*, Lecture Notes in Computer Science, vol. 5360, Springer, **2008**, pp. 258.
- (27) Boyle, P.; *Gaussian Processes for regression and Optimization*, PhD thesis, Victoria University of Wellington, New Zealand, **2007**.
- (28) Kleijnen, J.P.C. *Eur. J. Oper. Res.* **2009**, 192, 707.
- (29) Yan, S.; Minsker, B. *Water Resour. Res.* **2006**, 42, W05407.
- (30) O'Hagan, A. *J. Roy. Stat. Soc. B* **1978**, 40, 1.
- (31) Chen, T.; Ren, J. *Neurocomputing* **2009**, 72, 1605.
- (32) Csato, L.; Oppner, M. *Neural Computation* **2002**, 14, 641.
- (33) Edgar, T. F.; Himmelblau, D. M.; Lasdon, L. S. *Optimization of Chemical Process*; 2nd ed.; McGraw-Hill, 2001.
- (34) Martens, H. A.; Dardenne, P. *Chemometrics and intelligent laboratory systems* **1998**, 44, 99.
- (35) Quiñero-Candela, J.; Rasmussen, C.E.; Sinz, F.; Bousquet, O.; Schölkopf, B. *Evaluating predictive uncertainty challenge*, in: J. Quiñero-Candela et al. (Eds.), *Machine Learning Challenges, Lecture Notes in Computer Science*, vol. 3944, Springer, **2006**, pp. 1-27.

Chapter 7 Summary

Different transition metal molecular sieves were synthesized with extensive characterization techniques to demonstrate their physical and chemical properties. These materials were applied in the liquid-phase epoxidation catalysis and radius of pore curvature effect, pore structure effect were discussed in details. The proposed RSM framework was also used in the modeling and optimization of liquid-phase epoxidation processes.

To get an advanced study the pore size and structure effects of mesoporous materials, vanadium was introduced to three different kinds of mesoporous molecular sieves (MCM-41, SBA-15 and TUD-1) by grafting method. The vanadium on these supports was uniform in coordination and highly dispersed on the support surface within a control vanadium content (≤ 3 wt%) demonstrated by series characterization methods. Catalytic epoxidation of *trans*-stilbene and *cis*-cyclooctene were taken out as a probe reaction to test the pore structure effect with the different type of catalysts. Both the catalysis reactions show a better active performance of 3-D pore structure TUD-1 than the 2-D pore structure MCM-41 and SBA-15. This demonstrates the widely open 3-D structure can decrease the pore diffusion of reactants and allows greater accessibility of the reactants to the active sites embedded on the pore wall surface.

As most mesoporous materials are still not applicable in the industry, epoxidation catalysis using zeolites as support is studied. A series of vanadium-containing NaX catalysts was prepared by ion exchange method. Various characterization techniques were employed to detect the vanadium location and the results indicated that most of vanadium species was in V^{5+} valance and in tetrahedral coordination for both the V-X and V-X(C) samples. The vanadium species can be easily driven into supercage of the FAU zeolite during the ion-exchange while calcination step would lead to the shift of vanadium to the SOD cage. Epoxidation of *trans*-stilbene and *cis*-cyclooctene were carried out to test the catalytic performance of the catalysts. The V-X samples performed better conversion and epoxide selectivity than those of the V-X(C) samples both for the *trans*-stilbene epoxidation and the *cis*-cyclooctene epoxidation. The catalytic results of the vanadium-containing catalysts are in agreement with the location of vanadium oxide species in the V-X and V-X(C) samples.

To find an optimization method for the epoxidation, we proposed an iterative RSM framework for the modeling and optimization of chemical reaction processes. The central component of the proposed framework is a novel statistical approach, i.e. GP regression, which is used as the empirical model for RSM. Compared with traditional regression methods, GP models have been demonstrated to attain the capability of providing high prediction accuracy and reliable prediction uncertainty. The desirable

properties of GP model are the basis for model-based range-searching and optimization in the iterative framework. The proposed methodology has been successfully applied to the optimization of *trans*-stilbene epoxidation over Co^{2+} -X catalysts. In principle, the presented RSM framework is applicable to general “processes” in diverse fields of science, engineering, management, among others, where empirical models are developed from designed experiments to facilitate the rational, instead of “trial-and-error”, design and optimization of the processes. Currently, we are investigating the extension of the methodology to consider multiple objectives that are to be optimized.

Appendix

A.1 A non-Sodium Synthesis of Highly Ordered V-MCM-41 and its Catalytic

Application in Isomerization

MCM-41 has become one of the most popular mesoporous molecular sieves in the family of M41S, which was disclosed in 1992 by Mobil oil Corporation.^{1,2} Due to its unique properties, e.g., well defined mesostructure, narrow pore size distribution, tuneable pore diameter and high specific surface areas, MCM-41 has been widely used in heterogeneous catalysis, separation, electronics as well as optical fields.^{3,4} However, MCM-41 in its pure siliceous form shows limited applications in catalytic organic transformation due to the lack of active sites.^{3,4} Hence, modification is necessary by incorporating active components into the MCM-41 framework.

In recent years, the development of transition metal incorporated MCM-41 materials has attracted much attention in the fields of heterogeneous catalysis.⁵⁻⁷ Exploring the novel formulation to produce metal incorporated mesoporous MCM-41 with a scalable process is the first critical step to achieve their industrialized applications of these materials. Various preparation routes can be adopted to synthesize metal incorporated MCM-41 catalytic materials, e.g., ion-exchange,^{8,9} post grafting,¹⁰ direct synthesis, impregnation,⁹⁻¹³ and chemical vapour deposition.¹⁴ Most of these reported methods

usually utilize NaOH to get an alkali solution or use Na_2SiO_3 as the silica source. However, the elimination of complications arising from sodium is highly desired for the application of metal ion incorporated MCM-41 as catalytic material because sodium has a negative effect in the substitution of metal ions, catalytic reactions, and stability.¹⁵ Furthermore, the procedures of ion-exchange and post grafting methods are very complicated.

Vanadium containing MCM-41 has been widely investigated for the oxidation catalytic reaction.^{6,16} In this study, rapid synthesis of vanadium incorporated MCM-41 (V-MCM-41) materials with well-ordered mesostructure in the absence of sodium is reported; the direct hydrothermal synthesis is formulated with the addition of ammonia solution. The effects of ammonia addition and vanadium incorporation will be discussed in detail.

Alkene isomerization has been receiving considerable attention in recent years, focusing mainly on butene isomerization,^{17,18} as well as C5 and C6 alkene reactions.¹⁹⁻²¹ The long chain naphtha is the main components of high octane gasoline. C7 alkenes represent one of the largest contributions to the alkene pool. Isomerization of C7 alkenes can increase the octane number of heavy naphtha dramatically, which has great potential for improving the resistance of a fuel to knock. S. A. Goddard et al. studied the C7 alkene hydrotreating activity over $\text{CoMo}/\text{Al}_2\text{O}_3$,²² while Wehrer et al. carried out C7

isomerisation of alkenes on molybdenum oxides under rapid flow of hydrogen.²³ The iron-catalyzed alkene isomerization was also investigated.²⁴ However, the low surface areas of these catalysts have restricted their performances. As reported, MCM-41 shows much lower activity in catalytic cracking compared to USY or Beta zeolites because MCM-41 materials only presents mild acid sites.^{25,26} The incorporation of vanadium species manipulates the acidity on the MCM-41 pore wall surface to some extent. Along this line, one can predict that V-MCM-41 can be a good candidate for alkene isomerization. Herein, it is also reported the study of heptene isomerisation under hydrogen flow over V-MCM-41 mesoporous molecular sieves.

A.1.1 Experimental

The synthesis process of V-MCM-41 is shown in section 3.2.2.

In the heptene isomerization, 200 mg catalyst was loaded in the quartz reactor which was equipped with the thermocouple beside the catalyst bed for better monitoring of the pre-treatment and reaction temperature. The reactor was installed vertically inside a 35 mm i. d. tubular furnace controlled by a programmable PID temperature controller. Before each reaction run, the catalyst was pre-treated in situ in a hydrogen stream at 673 K for 1 h. Hydrogen was regulated by mass flow controller at 20 ml/min. Heptene with constant flow rate of 0.005 ml/min was controlled by a HPLC pump. The volume ratio of reactant feed mixture is 4.2 vol. % heptene vapour and 95.8 vol. % hydrogen. The

weight hourly space velocity (WHSV) was changed from 0.5 to 2 h⁻¹ by changing the catalyst weight. The entire micro-reactor, including the pipelines, was heated at 393 K to vaporize the heptene and avoid condensation of the products. The feedstock and products were analyzed by an on-line gas chromatograph (Agilent 6890) equipped with FID detector and PONA column.

A.1.2 Catalysts Characterization

A.1.2.1 X-ray diffraction

It is well known that MCM-41 is typically characterized by an X-ray reflection in the vicinity of $2\theta = 2^\circ$. In MCM-41 samples, the XRD peaks do not result from local order in the atomic range, but from the ordered channel walls. The powder XRD patterns of the calcined Si-MCM-41 and V-MCM-41 samples are shown in Figure A.1. Figure A.1(a) shows the XRD patterns of Si-MCM-41 prepared with different amounts of ammonia. A well ordered two-dimensional hexagonal structure can be observed, giving a sharp (100) plane diffraction peak and the diffraction peaks of higher miller index planes, (110), (200), (210), and (300). The Si-MCM-41 sample prepared with modest amount of ammonia shows the best structure, suggesting that the alkali environment will affect the hydrothermal synthesis to some extent, which is in good agreement with the literature reported elsewhere.²⁷ The vanadium incorporated MCM-41 samples (V-MCM-41) exhibit similar structure to that of Si-MCM-41 (Figure A.1(b)).

The main (100) diffraction peaks of V-MCM-41 samples shift to lower angle compared to that of Si-MCM-41, which may be caused by (i) the incorporation of vanadium ions in which V-O has longer bond than that of the Si-O, and (ii) the thickening of the pore wall due to the transition-metal-promoted cross-linking of the amorphous silica walls.²⁸

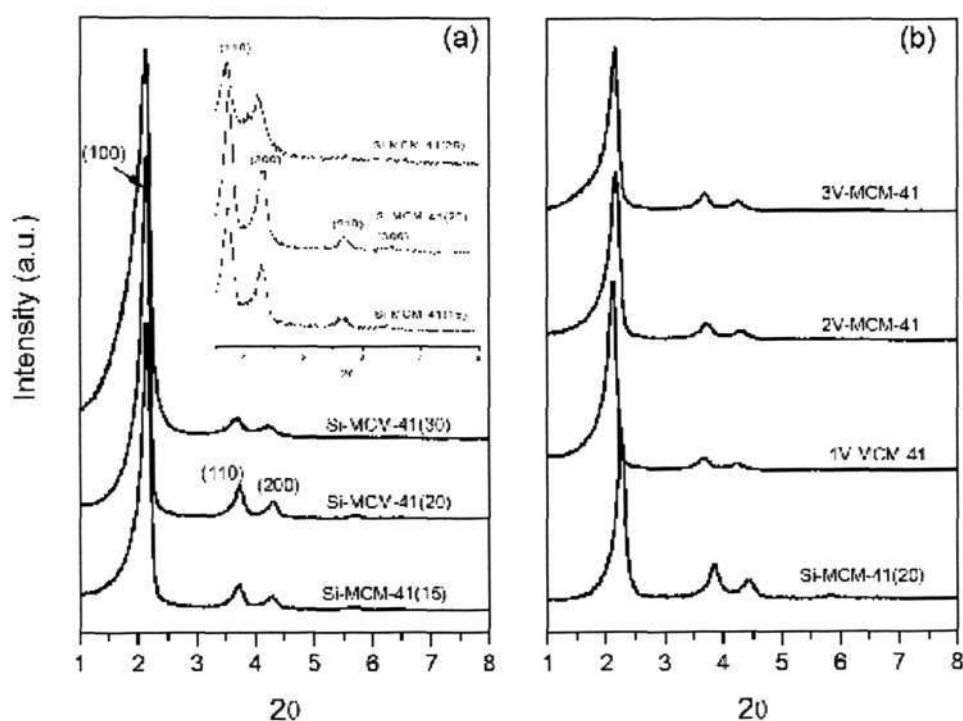


Figure A.1 X-ray diffraction patterns of Si-MCM-41 and V-MCM-41: (a) Si-MCM-41 synthesized with different amounts of ammonia; (b) V-MCM-41 with different vanadium content.

A.1.2.2 Nitrogen Physisorption

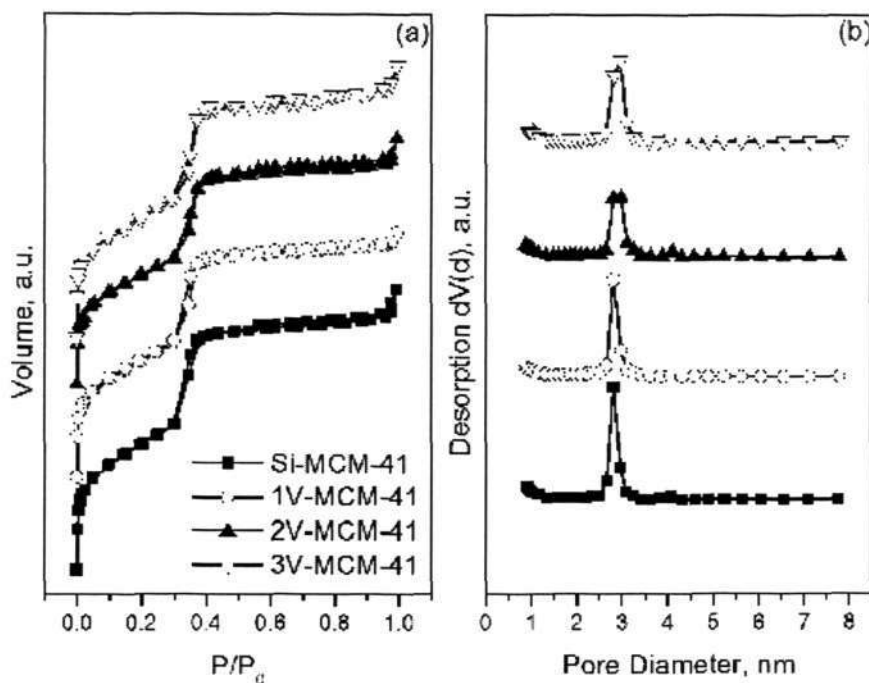


Figure A.2 Nitrogen physisorption of V-MCM-41 with different vanadium loading (a) isotherm graph of Si-MCM-41, 1V-MCM-41, 2V-MCM-41 and 3V-MCM-41 (b) Pore size distribution of Si-MCM-41, 1V-MCM-41, 2V-MCM-41 and 3V-MCM-41.

The nitrogen physisorption was conducted for a series of V-MCM-41 samples with different vanadium contents. The nitrogen adsorption/desorption isotherms and the corresponding pore size distributions are depicted in Figure A.2. The isotherms are assigned to type Langmuir IV isotherm according to the IUPAC classification. The

capillary condensation shows a sharp step increase in the relative pressure (P/P_0) range of 0.3-0.4 for all V-MCM-41 samples, suggesting typical mesoporous structure with uniform pore diameters. The uniformity of the pore structure changes with the incorporation of vanadium cations. The more the vanadium incorporation, the broader the pore size distribution of V-MCM-41 samples (Figure A.2(b)). Apparently, the incorporation of a large amount of vanadium disrupts the structure of V-MCM-41 over some distance, which is similar to the effect of other transition metal ions on the MCM-41 structure reported elsewhere.²⁹ The physicochemical properties of V-MCM-41 samples are summarized in Table A.1. The surface area and pore volume decrease when

Table A.1 List of physicochemical properties of Si-MCM-41 and V-MCM-41.

V content ^a (wt %)	Test V content ^b (wt %)	BET Surface Area (m ² /g)	Mesopore Volume (cc/g)	Pore Volume (cc/g)	Pore Diameter (nm)	d-spacing (nm)	Wall thickness (nm)
0	0	970	0.98	1.10	2.83	3.93	1.71
1	0.59	877	0.93	1.00	2.82	4.20	2.04
2	0.93	810	0.85	0.95	2.97	4.10	1.77
3	1.42	922	0.95	1.79	2.97	4.14	1.81

^a vanadium content added when synthesis.

^b vanadium content tested by ICP.

large amount of vanadium is incorporated. The pore diameter and wall thickness become larger as the result of the vanadium incorporation into the MCM-41 silica framework.

A.1.2.3 Diffuse reflectance UV-Vis spectroscopy

Table A.2 List of Edge Position of V-MCM-41 samples and the standard samples.

Sample name	Edge Position (eV)	Standard sample*	Edge position (eV)	Coordination condition
Si-MCM-41	-	Na3VO4	4.4	Tetrahedral
1V-MCM-41	4.16	NH4VO3	3.2	Distorted Tetrahedral
2V-MCM-41	3.98	PbV2O6	2.8	Distorted Octahedral
3V-MCM-41	4.04	V2O5	2.4	Square Pyramidal

* The standard samples are prepared by mixed pure chemical with Si-MCM-41 by grinding.

The local environmental formation of metal cations in an oxide domain can be revealed by UV-Vis spectroscopy. It is known that the quantum size effect results in the relationship between the optical band gap energy and the domain size. Diffuse reflectance UV-Vis spectra of V-MCM-41 samples are shown in Figure A.3(a). There is

no absorbance in the range of 600-800 nm region, indicating the lack of the characteristic d-d transitions of $(VO)^{2+}$.³⁰ This is probably caused by the valence of vanadium changing from 4+ to 5+ during the calcination. All samples show absorbance bands in 247 and 374 nm, which are attributed to the isolated vanadium species incorporated into the framework and on the pore wall surface, respectively.^{11,31} The absence of the 320 and 450 nm bands indicates there is no polymeric V-O-V bond and V_2O_5 crystallites in these V-MCM-41 materials.¹¹

The shape and shift of the absorption edge of the UV-Vis spectrum are useful in understanding the basic mechanism of optically-induced transitions in crystalline and non-crystalline materials, providing local structural coordination information. The edge position is determined in a classic approach³² by finding the energy intercept of a straight line fitted through the low energy rise in the profile of $[F(R_\infty) \times hv]^2$ vs hv , where $F(R_\infty)$ is the Kubelka-Munk function. This suggests an expression to correlate the absorption coefficient to photon energy, and the order of the power function depends on whether the transitions are allowed or forbidden.³³ However, different order of power is determined by the best linear fit of the energy gap curve for the cases of vanadium oxide species. The V-MCM-41 and referential samples with standard compounds (V_2O_5 , NH_4VO_3 , PbV_2O_6 , and Na_3VO_4) are tested. The transformations of $[F(R_\infty) \times hv]^2$ vs hv of samples 1V-MCM-41, 2V-MCM-41 and 3V-MCM-41 are shown

in Figure A.3(b). The absorption band reflects a ligand to metal charge transfer band (LCT) transition.⁶ Band gap edge energies of various V-MCM-41 samples are shown in Table A.2. All the band gap edge energies of V-MCM-41 samples fall into the region between Na_3VO_4 (tetrahedral) and NH_4VO_3 (distorted tetrahedral) indicating that the vanadium species in these V-MCM-41 samples is located in the distorted tetrahedral coordination.

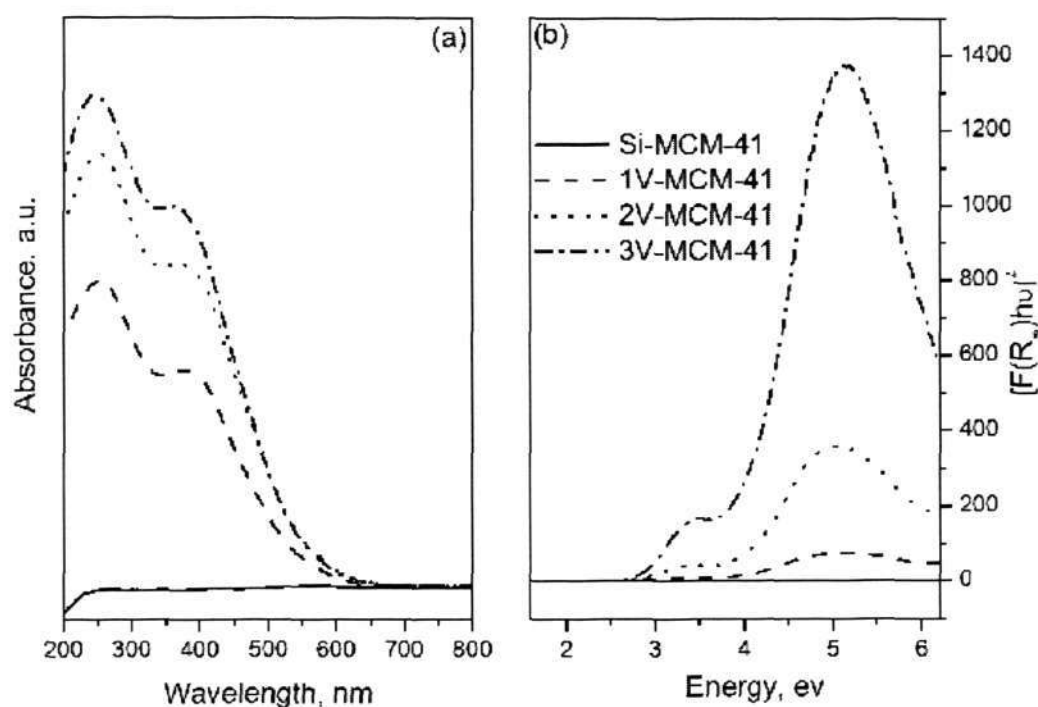


Figure A.3 UV-vis spectrum of V-MCM-41, (a) absorbance graph of V-MCM-41 (b)

UV absorption edge of V-MCM-41.

A.1.2.4 UV-Raman spectroscopy

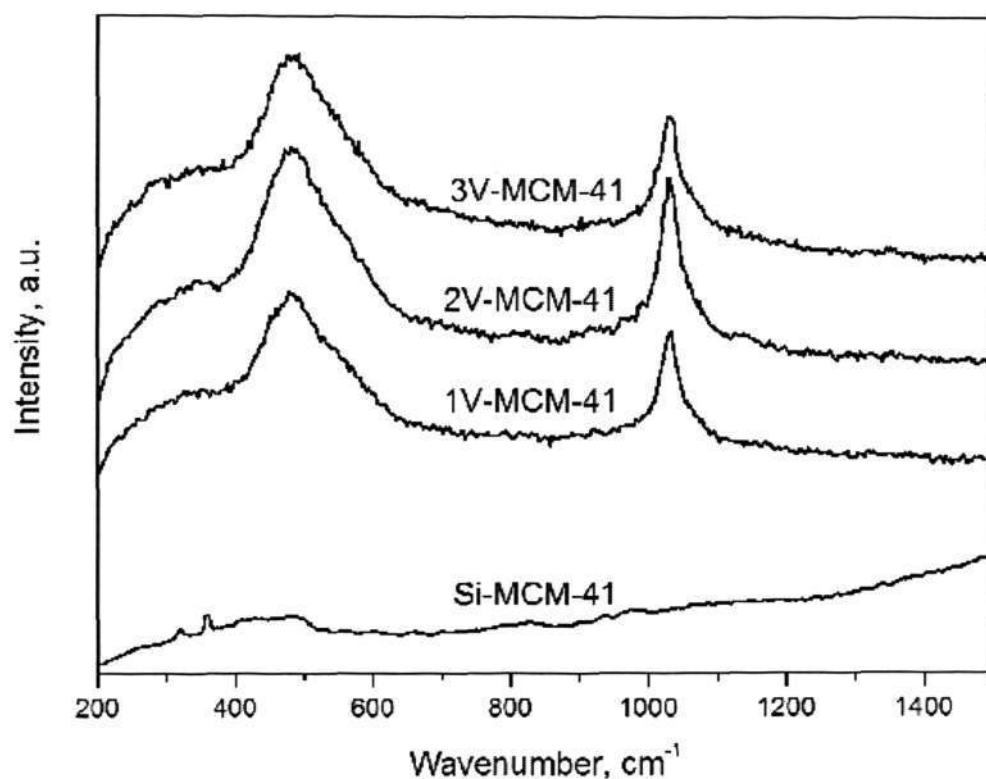


Figure A.4 Raman spectra V-MCM-41 materials

UV-Raman spectroscopy is used to elucidate the molecular nature of vanadium domains. The Raman spectra of V-MCM-41 samples with different vanadium loading are shown in Figure A.4. The peak at 486cm^{-1} is due to the threefold siloxane rings and siloxane bridges on the silica support.³⁴ A strong Raman band at $\sim 1033\text{ cm}^{-1}$ assignable to the symmetric V=O stretching vibration of isolated VO_4 species can be observed for

all the V-MCM-41 samples.³⁴⁻³⁶ The broad Raman band at $\sim 915\text{ cm}^{-1}$ is the characteristics of Si-O- and Si(-O-)₂ functionalities corresponding to the perturbation in silica vibrations, which may be an indication of the V-O-Si formation.³⁷ No significant band at $\sim 141\text{ cm}^{-1}$ corresponding to crystalline V₂O₅ can be observed. Furthermore, the absence of typical band at 995 cm^{-1} of V₂O₅ implies no polymeric crystalline V₂O₅ is formed in the V-MCM-41 samples, which is in good agreement with UV-Vis results. These observations suggest the vanadium domains in the siliceous framework or on the pore wall surface are all in an isolated state, without aggregation to form crystalline V₂O₅.

A.1.2.5 Electron Paramagnetic Resonance (EPR)

EPR is a powerful and sensitive technique for investigating the oxidation states, surfaces, bulk coordination and the physical form of a transition metal oxide. V⁴⁺ cations are very convenient EPR probes because the ⁵¹V (natural abundance 99.8%) nuclei have a large magnetic moment leading to informative hyperfine structures ($S=1/2$; $I=7/2$). Figure A.5 shows the EPR spectra of calcined V-MCM-41 samples. There is no tetravalent vanadium (V⁴⁺) signal shown for 0.2 wt. % V-MCM-41 sample, which indicates that nearly all vanadium has been oxidized to 5+ during the calcination. However, samples with higher V content show an axially symmetrical signal of tetravalent vanadium which originated from the d^1 electron interaction with nuclear spin

signals with nuclear spin of ^{51}V . The spectrum indicates only one vanadium site and the spin Hamiltonian parameters are $g=1.984$ and $A=110\text{G}$ where A is the hyperfine coupling constant. This signal can be assigned to tetrahedrally coordinated vanadium inside the pore wall of MCM-41, which cannot be fully oxidized during the calcination. No spin-spin interaction among V^{4+} ions indicates that V^{4+} is highly dispersed in the silica framework.^{38,39}

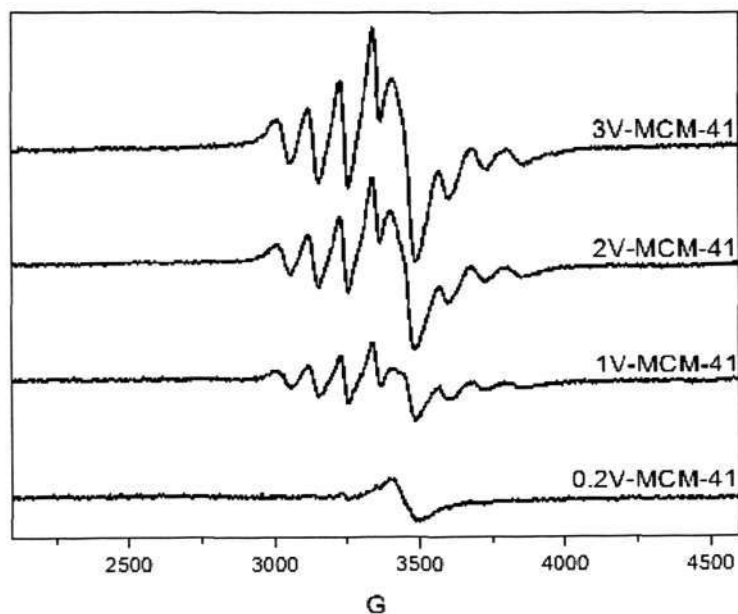


Figure A.5 EPR spectra (1st derivative) of 0.2V-MCM-41, 1V-MCM-41, 2V-MCM-41, and 3V-MCM-41.

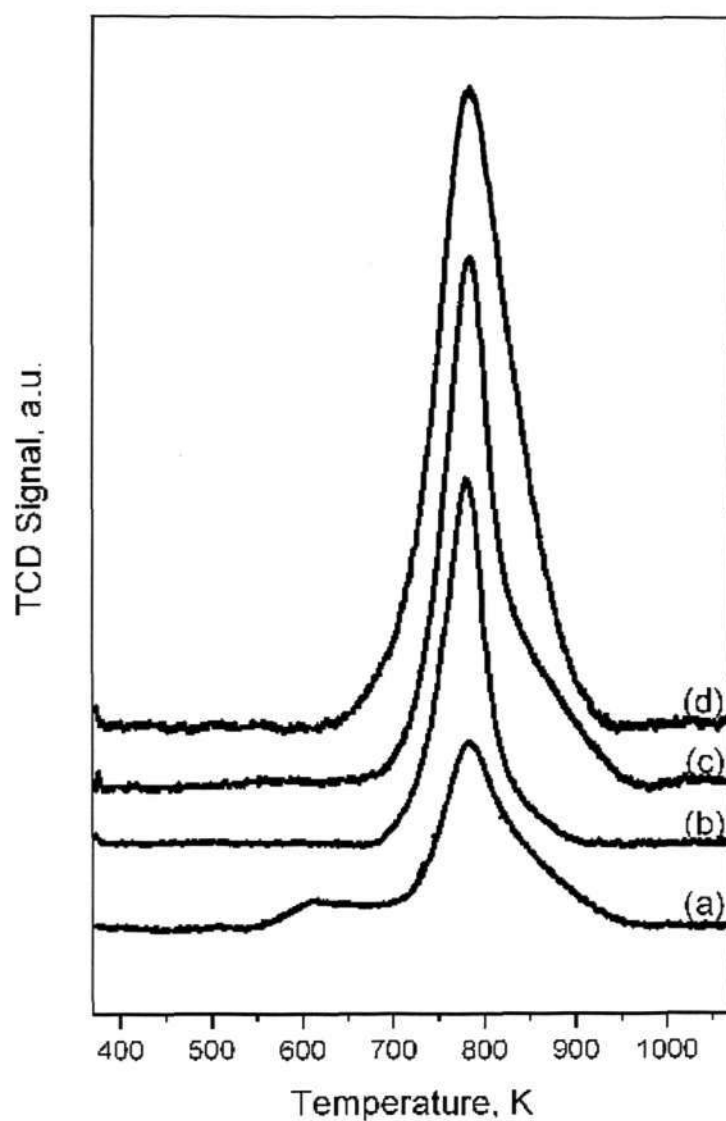


Figure A.6 H_2 -TPR profiles of impregnated vanadium on different catalysts.

(a),(b),(c),(d) represent impregnated V/MCM-41, 1V-MCM-41, 2V-MCM-41, 3V-MCM-41.

A.1.2.6 Hydrogen temperature programmed reduction (H_2 -TPR)

By H_2 -TPR analysis, not only the reducibility and stability of the metal supported or unsupported catalysts can be revealed, but also the more profound surface chemical information, i.e., metal species, metal distribution, the loading of different metal surface forms, can be ideally provided. In this study, the temperature programmed reduction was carried out from 323K to 1073K for 1V-MCM-41, 2V-MCM-41, 3V-MCM-41 as well as the impregnated V/MCM-41.

The H_2 -TPR profiles are shown in Figure A.6. The strong reduction peak at around 778K is attributed to the reduction of vanadium in the framework. Only one sharp reduction signal for 1V-MCM-41, 2V-MCM-41, 3V-MCM-41 indicates the uniform distribution of vanadium species with single valence state, the valence state changes from V^{5+} to V^{3+} after reduction calculated by the hydrogen consumption. For the vanadium impregnated sample V/MCM-41, there is a broad peak around 607K due to the presence of the vanadium on the surface of MCM-41 in which there is a lack of strong interaction with MCM-41 support.

A.1.2.7 Ammonia Temperature Programmed Desorption (NH_3 -TPD)

The temperature programmed desorption of basic molecule such as ammonia (NH_3 -TPD) is one of the most commonly used methods for measuring the surface acidity of porous materials. The NH_3 -TPD profiles of 1V-MCM-41, 2V-MCM-41 and 3V-MCM-

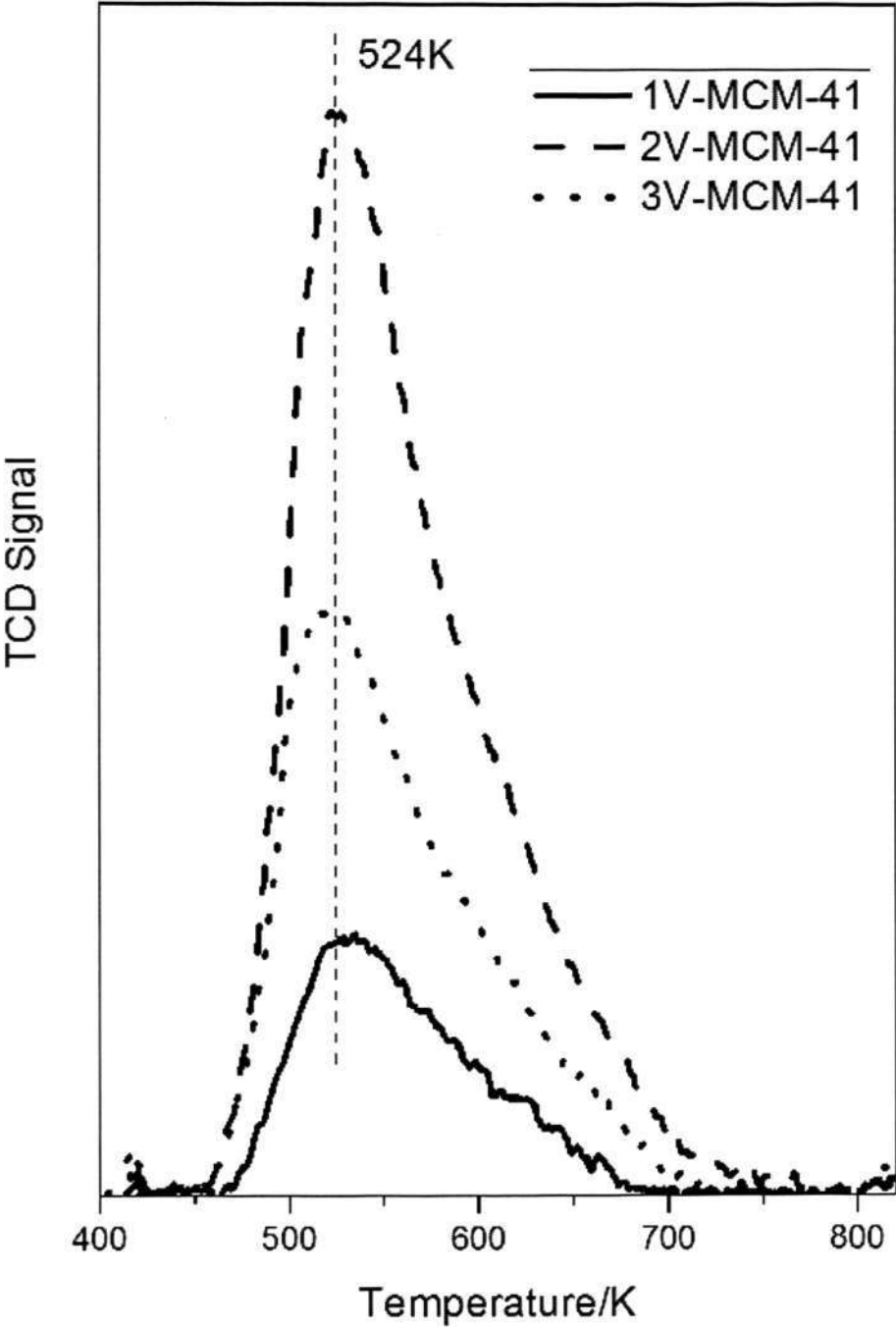


Figure A.7 NH₃-TPD results of V-MCM-41 materials.

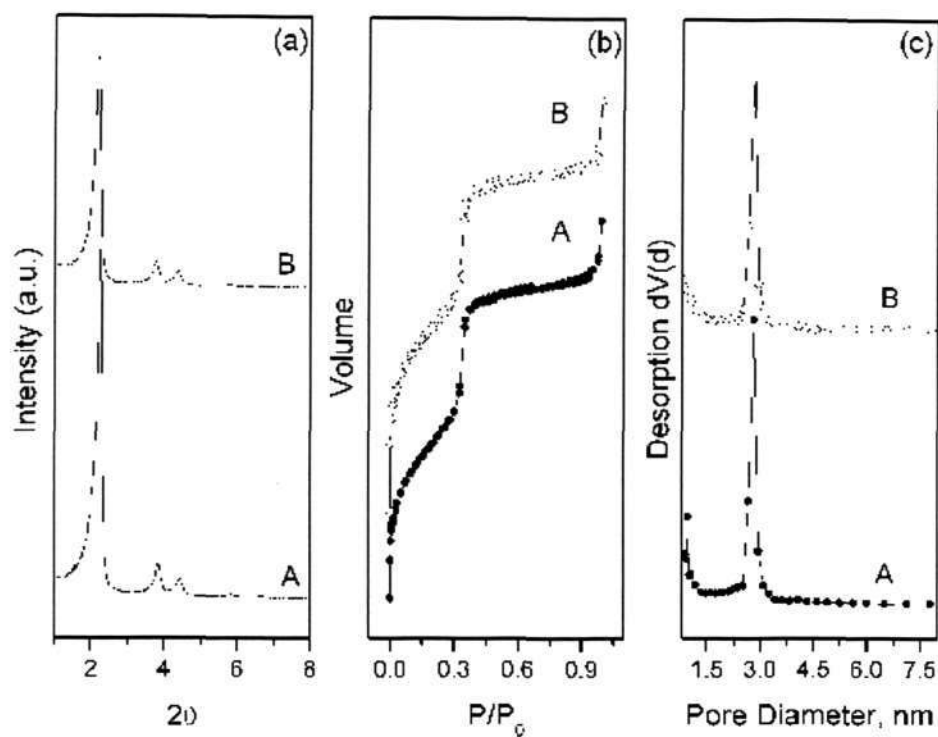


Figure A.8(a) XRD patterns of 1V-MCM-41 before and after reaction of heptene isomerization. (b) Isotherm graph of 1V-MCM-41 before and after heptene isomerization reaction (c) Pore size distribution of 1V-MCM-41 before and after heptene isomerization reaction. A represents the sample before reaction and B represents the sample after reaction.

41 samples are shown in Figure A.7. Only one broad desorption peak is observable at medium temperature range, and the peak position is almost identical at 524K for all the samples, suggesting the similar acidity strength which is in the mild acidity range. The

total amount of Bronsted acid sites increases with the content of vanadium incorporated in the silica framework of MCM-41. The calculated acidity amount for 1V-MCM-41, 2V-MCM-41 and 3V-MCM-41 are 0.012 mol/g, 0.048 mol/g and 0.097 mol/g, respectively. The correlation between total acidity amount and vanadium content gives the evidence that the acidity in the V-MCM-41 is mainly caused by the vanadium sites in the structure.⁴¹

A.1.2.8 Structure stability after reaction

N₂ physisorption and XRD experiments were performed to test the structural stability of V-MCM-41 catalysts under reaction conditions, as shown in Figure A.8. The XRD patterns illustrate that the V-MCM-41 sample still preserves its good hexagonal structure even under reaction conditions. Nitrogen physisorption was also tested as shown in Figure A.8 (b) and (c); it confirms the XRD results that our V-MCM-41 samples are stable under this isomerization reaction conditions.

A.1.3 Heptene isomerization

In this study, V-MCM-41 is demonstrated as a good catalyst to catalyze the heptene isomerization due to its mild acidity. Alkene isomerization shows more complicated reaction scheme compared to alkane isomerization. Besides the skeletal isomerization and double bond shift, hydrogenation of alkene to the corresponding alkane accompanies isomerization under hydrogen environment. In this study, the isomer

selectivity is defined as the total isomerization (skeletal isomerization and double bond shift reaction) over the total C7 conversion (skeletal isomerization, double bond shift reaction, and hydrogenation).

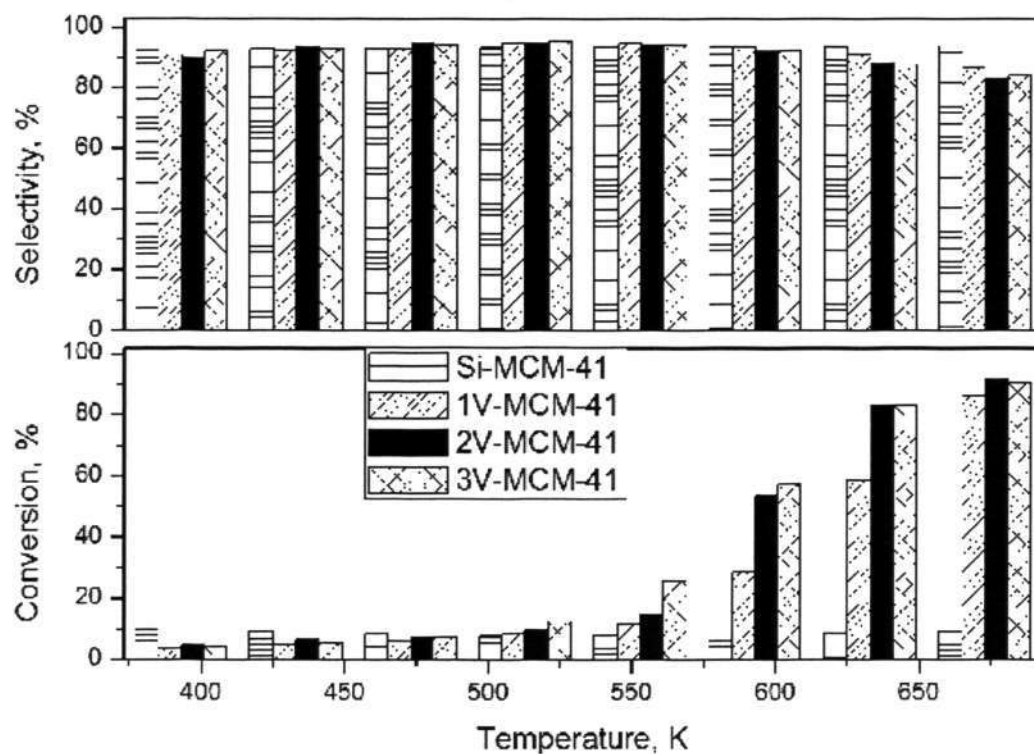


Figure A.9 Catalytic results about the conversion and selectivity of heptene isomers by Si-MCM-41, 1V-MCM-41, 2V-MCM-41 and 3V-MCM-41.

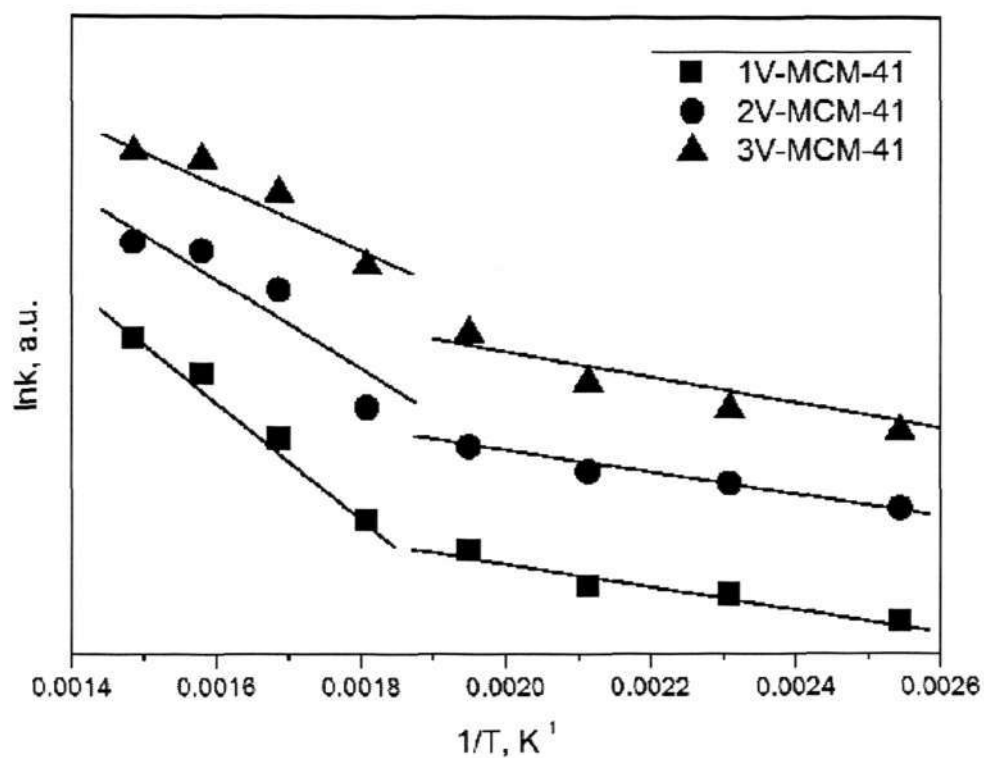


Figure A.10 Linear relationship between $\ln k$ vs $1/T$ for V-MCM-41.

The conversion and isomer selectivity of heptene isomerization over V-MCM-41 samples are shown in Figure A.9. Pure siliceous Si-MCM-41 exhibits the conversion of around 10% and does not change significantly with temperature. The low conversion is probably due to the weak acidic sites of Si-MCM-41 arise from the silanol groups on the pore wall surface.⁴² The isomer selectivity (~92%) stays constant within the range of reaction temperature tested in this study. For 1V-MCM-41, 2V-MCM-41, and 3 V-

MCM-41 catalyst, the conversion of heptene is similar with the Si-MCM-41 when temperature is below 550 K, whereas a remarkable increase of heptene conversion occurs at the temperature above 550 K. The conversion reaches 90% at 673 K and the selectivity maintains above 83%, suggesting that vanadium cations bring stronger acidic sites into V-MCM-41 than that of silanol group and these acidic sites become more active at the temperature above 550 K.⁴¹ Increasing vanadium content from 1 to 3 wt. % gives higher conversion under high temperature (> 650 K). The selectivity of isomers slightly decreases for the V-MCM-41 catalyst with high vanadium content, e.g., from 94% to 84% for 3V-MCM-41 at temperature about 650 K due to more hydrogenation occurs at high temperature. These results indicate that V-MCM-41 may favor both isomerization and hydrogenation at high temperature, although isomers are still the main product. The absence of cracking and cyclo-alkene products, even under high temperature (650 K), suggests the good potential for industry application of V-MCM-41 as a catalyst for alkene isomerization.

Activation energy of the reaction was calculated using Arrhenius plot shown in Figure A.10. Two stage of linear relationship is observed. The activation energies for 1V-MCM-41, 2V-MCM-41 and 3V-MCM-41 are calculated as 10.2, 10.3 and 10.2 kJ/mol, respectively between temperature of 513 K and 393 K, which may be attributed to the diffusion limitation of heptene in the V-MCM-41 channels under low temperature.

The activation energies are 52.4, 46.8 and 32.7 kJ/mol for 1V-MCM-41, 2V-MCM-41 and 3V-MCM-41, respectively between temperature 550 K and 700 K. The decrease of activation energy can be explained by the addition of more O-vacancy when vanadium cations incorporate into the silica framework.⁴³

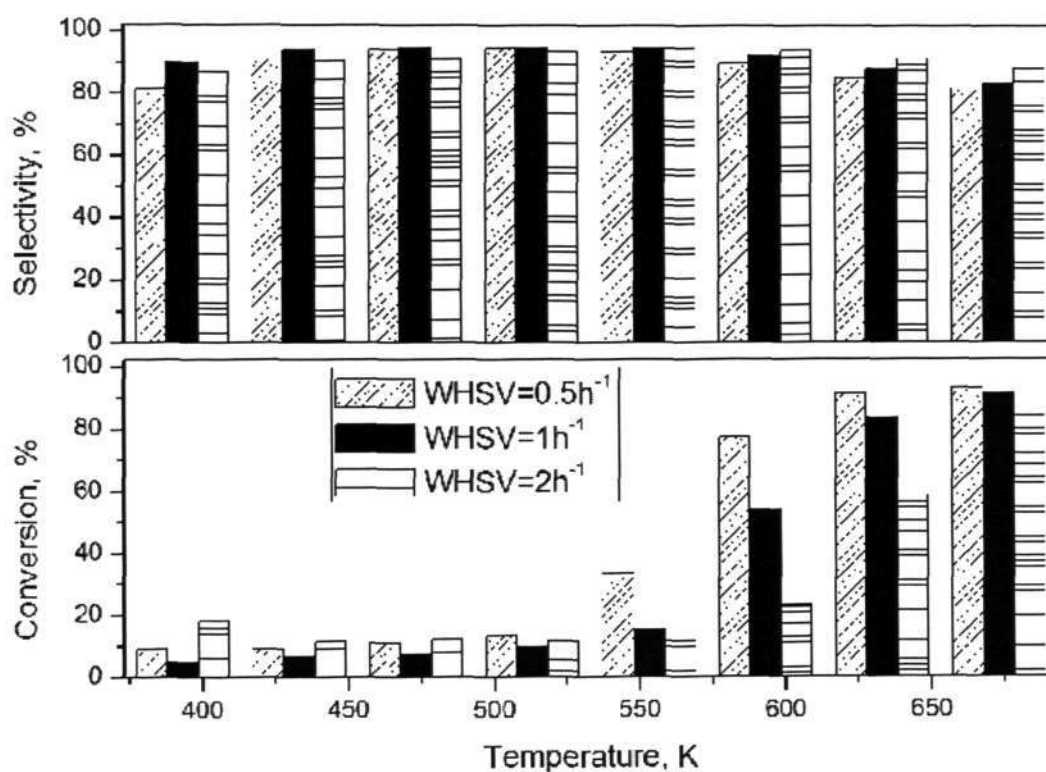


Figure A.11 Conversion and selectivity of isomers with different WHSV (0.5h⁻¹, 1h⁻¹, 2h⁻¹) on 2V-MCM-41.

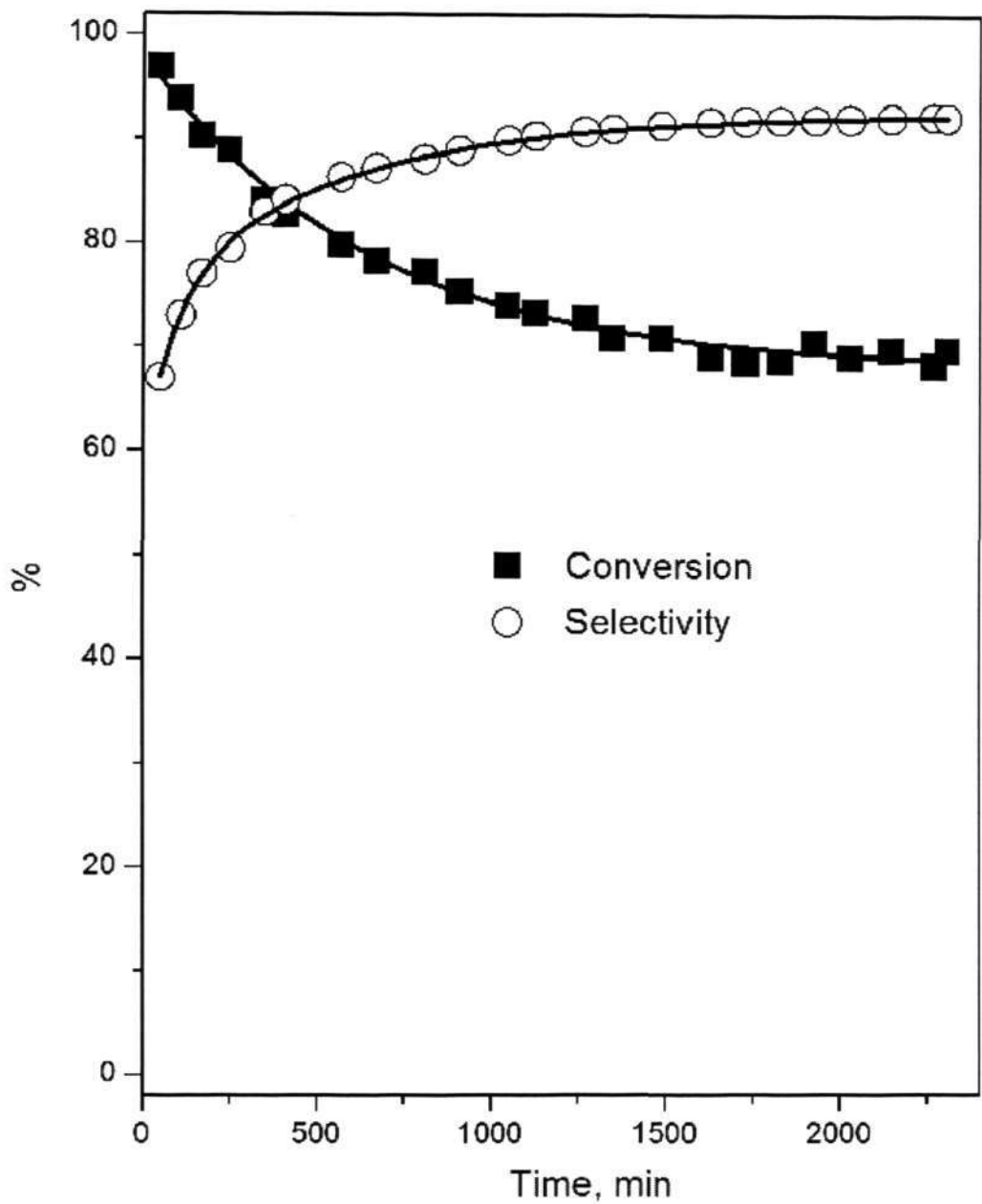


Figure A.12 Conversion and selectivity of isomers over long time test on 2V-MCM-41 under 593K.

Weight hourly space velocity (WHSV) effect was tested by varying the weight of 2V-MCM-41 catalyst, shown in Figure A.11 (WHSV=0.5h⁻¹, 1h⁻¹, 2h⁻¹). Increasing WHSV leads to a lower heptene conversion due to the insufficient contact between catalyst and reactant flow. Interestingly, the selectivity of isomer was observed to increase with the space velocity at elevated temperature, suggesting that high WHSV is favorable to isomerization than hydrogenation. When the temperature is above 673 K, the effect of different WHSV on heptene conversion becomes less significant.

The long-term stability of 2V-MCM-41 catalyst was tested under 593 K for 40 hours as shown in Figure A.12. The conversion gradually decreases, whereas the selectivity of isomers shows a rapid increase via reaction time. After 1600 min, the stabilized conversion and isomer selectivity are 70% and 93%, respectively.

A.1.4 Conclusion

A series of highly ordered V-MCM-41 samples were successfully synthesized rapidly using ammonia solution. The XRD and N₂ adsorption/desorption showed that the samples possess highly ordered structure and narrow pore size distribution. UV-Vis, UV-Raman, and EPR characterizations indicated that the vanadium ions in the mesoporous molecular sieves were in a tetrahedral coordination and distributed on the pore wall surface with an atomic level dispersion. The heptene isomerization results

showed that V-MCM-41 catalysts presented high conversion and isomer selectivity because of its mild acidity brought by the vanadium incorporation.

Reference:

- (1) Beck, J.S.; Vartuli, J.C.; Roth, W.J.; Leonowicz, M.E.; Kresge, C.T.; Schmitt, K.D.; Chu, C.T.W.; Olson, D.H.; Sheppard, E.W.; McCullen, S.B.; Higgins, J.B.; Schlenker, J.L.; *Journal of the American Chemical Society* **1992**, *113*, 10834
- (2) Kresge, C.T.; Leonowicz, M.E.; Roth, W.J.; Vartuli, J.C.; Beck, J.S. *Nature* **1992**, *359*, 710.
- (3) Xu, J.Q.; Chu, W.; Luo, S.Z. *Journal of Molecular Catalysis A-Chemical* **2006**, *256*, 48.
- (4) Ying, J.Y.; Mehnert, C.P.; Wong, M.S. *Angewandte Chemie International Edition in English Angew* **1999**, *38*, 56.
- (5) Dapurkar, S.E.; Sakthivel, A.; Selvam, P. *Journal of Molecular Catalysis A-Chemical* **2004**, *223*, 241.
- (6) Kwak, J.H.; Herrera, J.E.; Hu, J.Z.; Wang, Y.; Peden, C.H.F. *Applied Catalysis A-General* **2006**, *300*, 109.
- (7) Chen, Y.; Ciuparu, D.; Lim, S.; Haller, G.L.; Pfefferle, L.D. *Carbon* **2006**, *44*, 67.
- (8) Gucbilmez, Y.; Dogu, T.; Balci, S. *Catalysis Today* **2005**, *100*, 473.
- (9) Zhang, Q.H.; Wang, Y.; Ohishi, Y.; Shishido, T.; Takehira, K. *Journal of Catalysis* **2001**, *202*, 308.
- (10) Pena, M.L.; Dejoz, A.; Fornes, V.; Rey, E.; Vazquez, M.I.; Nieto, J.M.L. *Applied Catalysis A-General* **2001**, *209*, 155.
- (11) Solsona, B.; Blasco, T.; Nieto, J.M.L.; Pena, M.L.; Rey, F.; Vidal-Moya, A. *Journal of Catalysis* **2001**, *203*, 443.

- (12) Du, G.A.; Lim, S.Y.; Yang, Y.H.; Wang, C.; Pfefferle, L.; Haller, G.L. *Applied Catalysis A-General* **2006**, 302, 48.
- (13) Parida, K.M.; Rath, D. *Journal of Molecular Catalysis A-Chemical* **2006**, 258, 381.
- (14) Grubert, G.; Rathousky, J.; Schulz-Ekloff, G.; Wark, M.; Zukal, A. *Microporous and Mesoporous Materials* **1998**, 22, 225 .
- (15) Xia, Q.H.; Chen, X.; Tatsumi, T. *Journal of Molecular Catalysis A-Chemical* **2001**, 176, 179.
- (16) Selvam, P.; Dapurkar, S.E. *Journal of Catalysis* **2005**, 229, 64.
- (17) de Menorval, B.; Ayrault, P.; Gnep, N.S.; Guisnet, M. *Journal of Catalysis* **2005**, 230, 38.
- (18) de Menorval, B.; Ayrault, P.; Gnep, N.S.; Guisnet, M. *Applied Catalysis A-General* **2006**, 1.
- (19) Guo, J.; Cheng, X.W.; Zhou, W.Z.; Long, Y.C. *Microporous and Mesoporous Materials* **2005**, 79, 319.
- (20) Tiitta, M.; Harlin, E.; Makkonen, J.; Root, A.; Sandelin, F.; Osterholm, H. in *Recent Advances in the Science and Technology of Zeolites and Related Materials* **2004**, Pts a - C, pp. 2323.
- (21) Li, D.D.; Li, M.F.; Chu, Y.; Nie, H.; Shi, Y.H. *Catalysis Today* **2003**, 81, 65.
- (22) Goddard, S.A.; Kukes, S.G. *Energ. Fuel.* **1994**, 8, 147.
- (23) Wehrer, P.; Libs, S.; Hilaire, L. *Applied Catalysis A-General* **2003**, 238, 69.
- (24) Glascoe, E.A.; Sawyer, K.R.; Shanoski, J.E.; Harris, C.B. *Journal of Physical Chemistry C* **2007**, 111, 8789.
- (25) Taguchi, A.; Schuth, F. *Microporous and Mesoporous Materials* **2005**, 77, 1.

- (26) Auroux, A. *Top. Catal.* **2002**, 19, 205.
- (27) Lim, S.; Ciuparu, D.; Yang, Y.H.; Du, G.A.; Pfefferle, L.D.; Haller, G.L. *Microporous and Mesoporous Materials* **2007**, 101, 200.
- (28) Parvulescu, V.; Anastasescu, C.; Constantin, C.; Su, B.L. *Catalysis Today* **2003**, 78, 477.
- (29) Shylesh, S.; Singh, A.P. *Journal of Catalysis* **2005**, 233, 359.
- (30) Yang, Y.H.; Lim, S.; Du, G.A.; Chen, Y.; Ciuparu, D.; Haller, G.L. *Journal of Physical Chemistry B* **2005**, 109, 13237.
- (31) Shylesh, S.; Singh, A.R. *Journal of Catalysis* **2006**, 244, 52.
- (32) Yang, Y.H.; Du, G.A.; Lim, S.Y.; Haller, G.L. *Journal of Catalysis* **2005**, 234, 318.
- (33) Weber, R.S. *Journal of Catalysis* **1995**, 151, 470.
- (34) Davis, E.A.; Mott, N.F. *Philos. Mag.* **1970**, 22, 903.
- (35) Das, N.; Eckert, H.; Hu, H.C.; Wachs, I.E.; Walzer, J.F.; Feher, F.J. *Journal of Physical Chemistry* **1993**, 97, 8240.
- (36) Went, G.T.; Oyama, S.T.; Bell, A.T. *Journal of Physical Chemistry* **1990**, 94, 4240.
- (37) Ying, F.; Li, J.H.; Huang, C.J.; Weng, W.Z.; Wan, H.L. *Catalysis Letters* **2007**, 115, 137.
- (38) Chatterjee, M.; Iwasaki, T.; Hayashi, H.; Onodera, Y.; Ebina, T.; Nagase, T. *Chemical Materials* **1999**, 11, 1368.
- (39) Subrahmanyam, C.; Louis, B.; Viswanathan, B.; Renken, A.; Varadarajan, T.K. *Applied Catalysis A-General* **2005**, 282, 67.
- (40) Rodriguez-Gonzalez, L.; Hermes, F.; Bertmer, M.; Rodriguez-Castellon, E.; Jimenez-Lopez, A.; Simon, U. *Applied Catalysis A-General* **2007**, 328, 174.
- (41) Lim, S.; Haller, G.L. *Journal of Physical Chemistry B* **2002**, 106, 8437.

- (42) Slomkiewicz, P.M. *Applied Catalysis A-General* **2006**, 301, 232.
- (43) Goodrow, A.; Bell, A.T. *Journal of Physical Chemistry C* **2008**, 112, 13204.

A.2 Publications

- Shuangquan Hu, Lusi Li, Sufen Xu, Qinghu Tang, Yanhui Yang, Epoxidation of trans-stilbene and cis-cyclooctene over vanadium containing mesoporous materials with different pore sizes and structures, (Submitted)
- Shuangquan Hu, Lusi Li, Qinghu Tang, Yanhui Yang, Preparation, Characterization and Catalytic Properties of Vanadium Exchanged X Faujasite Zeolites for the Epoxidation Reaction of trans-Stilbene and cis-Cyclooctene. (Submitted)
- Shuangquan Hu, Qinghu Tang, Ying Bin Lau, Wenjin Yan, Yanhui Yang, Tao Chen, Response surface methodology using Gaussian processes: towards optimizing the trans-stilbene epoxidation over Co^{2+} -NaX catalysts, (Revision)
- Dapeng Liu, Xian-Yang Quek, Shuangquan Hu, Lusi Li, Hui Min Lim, Yanhui Yang, Mesoporous TUD-1 supported molybdophosphoric acid (HPMo/TUD-1) catalysts for n-heptane hydroisomerization, *Catalysis Today*, (in press)
- Shuangquan Hu, Dapeng Liu, Lusi Li, Armando Borgna, Yanhui Yang, A non-sodium synthesis of highly ordered V-MCM-41 and its catalytic application in isomerization, *Catalysis Letters*, 2009, 129(3-4), 478-485
- Dapeng Liu, Shuangquan Hu, Raymond Lau, Armando Borgna, Gary L. Haller, Yanhui Yang, Hydroconversion of n-heptane over Pt/Al-MCM-41 mesoporous molecular sieves, *Chemical Engineering Journal*, 2009, 151, 308-318

- Xian-Yang Quek, Qinghu Tang, Shuangquan Hu, Yanhui Yang, Liquid phase trans-stilbene epoxidation over catalytically active cobalt substituted TUD-1 mesoporous materials (Co-TUD-1) using molecular oxygen, Applied Catalysis A-General, 2009, 361, 130-136
- Qinghu Tang, Chuan Wang, Shuangquan Hu, Hui Sun, Yuan Chen, Gary L. Haller, Yanhui Yang, Radius of curvature effect on the selective oxidation of cyclohexene over highly ordered V-MCM-41, Catalysis Letters, 2007, 117(1-2), 25-33